Electrical Scanning Probe Microscopy on Organic Optoelectronic Structures

Dissertation

zur Erlangung des Grades
„Doktor der Naturwissenschaften“
am Fachbereich Physik, Mathematik und Informatik
der Johannes-Gutenberg-Universität in Mainz

vorgelegt von

Stefan Weber

geboren in Trier

Mainz, den 26. August 2010

Die vorliegende Arbeit wurde in der Zeit von September 2007 bis August 2010 unter der Betreuung von Dr. Rüdiger Berger und Prof. Dr. Hans-Jürgen Butt am Max-Planck-Institut für Polymerforschung in Mainz durchgeführt.

Dekan: Prof. Dr. Manfred Lehn

1. Berichterstatter: Prof. Dr. H.J. Butt
2. Berichterstatter: Prof. Dr. T. Palberg
3. Berichterstatter: Prof. Dr. E. Meyer (Universität Basel, Schweiz)
4. Berichterstatter: Prof. Dr. D.Y. Yoon (Seoul National University, Südkorea)

"I am a firm believer that without speculation
there is no good and original observation."

Charles R. Darwin in a letter to Alfred R. Wallace,
December 22nd, 1857

Zusammenfassung

Im Bereich der organischen Optoelektronik hat die mikro- und nanoskopische Struktur der Materialien einen großen Einfluss auf die Leistungsfähigkeit der Bauteile. In diesem Bereich gewinnen rasterkraftmikroskopische Methoden (SFM) immer mehr an Bedeutung. Neben topographischer Information können zahlreiche andere Oberflächeneigenschaften wie elektrische Leitfähigkeit (Leitfähigkeits-Rasterkraftmikroskopie, C-SFM) oder Oberflächenpotentiale (Kelvinsondenmikroskopie, KPFM) mit Auflösungen im Bereich von Nanometern gemessen werden.

Im Rahmen dieser Arbeit wurden die SFM basierten elektrischen Betriebsmodi verwendet um den Zusammenhang zwischen Morphologie und den elektrischen Eigenschaften in optoelektronischen Hybridstrukturen zu erforschen. Diese Strukturen wurden in der Gruppe von Prof. J. Gutmann (MPI-P Mainz) entwickelt. Konkret wurde ein neuartiges Nanokomposit für eine integrierte Elektronen-Barriereschicht untersucht. Eine Struktur von elektrisch leitfähigen Pfaden entlang kristalliner TiO_2-Partikeln in einer isolierenden Schicht aus einer Keramik wurde gefunden. Darüber hinaus konnten Defektstrukturen identifiziert werden. Um die interne Struktur einer funktionsfähigen Hybridsolarzelle zu untersuchen, wurde eine Bruchkante mit einem fokussierten Ionenstrahl poliert. Mittels C-SFM konnten die funktionalen Schichten identifiziert und die Transporteigenschaften des neuartigen Kompositmaterials in der aktiven Schicht untersucht werden.

Durch den Einsatz von C-SFM können weiche Oberflächen dauerhaft zerstört werden: (i) durch Kräfte, die die Spitze ausübt, (ii) hohe elektrische Felder und (iii) hohe Stromdichten im Bereich der Spitze. Aus diesem Grund wurde ein alternativer Betriebsmodus basierend auf dem Torsion Mode in Kombination mit lokalen Leitfähigkeitsmessungen eingeführt. Im Torsion Mode vibriert die Spitze lateral und befindet sich dabei sehr nahe an der Oberfläche. Auf diese Weise kann ein elektrischer Kontakt zwischen Spitze und Probe hergestellt werden. In einer Reihe von Referenzexperimenten auf Standardoberflächen wurden grundlegende Aspekte der Leitfähigkeits-Torsionsmikroskopie (SCTMM) untersucht. Darüber hinaus wurden Proben mit Feldern aus freistehenden Nanosäulen aus einem halbleitenden Polymer untersucht, die in der Gruppe von Dr. P. Theato (Universität Mainz) entwickelt wurden. Mittels SCTMM konnten die Strukturen zerstörungsfrei und hochauflösend abgebildet und die Leitfähigkeit von individuellen Nanosäulen gemessen werden.

Zur Untersuchung lichtinduzierter Effekte in Nanostrukturen wurde ein neuer Kraft-mikroskop-Aufbau mit einer Laser-Probenbeleuchtung konstruiert. Mit diesem Photoelektrischen SFM wurde die Reaktion funktionalisierter Nanostäbchen auf Beleuchtung untersucht. Dazu wurde in der Gruppe von Prof. R. Zentel (Universität Mainz) ein neuartiges Blockcopolymer mit einem Anker- und Farbstoffblock und einem halbleitenden Polymerblock synthetisiert und kovalent an ZnO Nanostäbchen gebunden. Dieses System stellt ein Elektronen Donot/Akzeptorsystem dar und kann daher als ein Modell für eine Solarzelle auf der Nanoebene angesehen werden. Mittels KPFM auf beleuchteten Proben konnte die lichtinduzierte Ladungstrennung zwischen Stab und Polymer nicht nur visualisiert, sondern auch quantifiziert werden.

Die Ergebnisse zeigen, dass mittels elektrischer Rasterkraftmikroskopie fundamentale Prozesse in optoelektronischen Nanostukturen untersucht werden können. Diese Erkenntnisse liefern wertvolle Informationen an die synthetischen Chemiker, die ihre Materialien nach diesen Aspekten weiter optimieren können.

Abstract

In the field of organic optoelectronics, the nanoscale structure of the materials has huge impact on the device performance. Here, scanning force microscopy (SFM) techniques become increasingly important. In addition to topographic information, various surface properties can be recorded on a nanometer length scale, such as electrical conductivity (conductive scanning force microscopy, C-SFM) and surface potential (Kelvin probe force microscopy, KPFM).

In the context of this work, the electrical SFM modes were applied to study the interplay between morphology and electrical properties in hybrid optoelectronic structures, developed in the group of Prof. J. Gutmann (MPI-P Mainz). In particular, I investigated the working principle of a novel integrated electron blocking layer system. A structure of electrically conducting pathways along crystalline TiO_2 particles in an insulating matrix of a polymer derived ceramic was found and insulating defect structures could be identified. In order to get insights into the internal structure of a device I investigated a working hybrid solar cell by preparing a cross cut with focused ion beam polishing. With C-SFM, the functional layers could be identified and the charge transport properties of the novel active layer composite material could be studied.

In C-SFM, soft surfaces can be permanently damaged by (i) tip induced forces, (ii) high electric fields and (iii) high current densities close to the SFM-tip. Thus, an alternative operation based on torsion mode topography imaging in combination with current mapping was introduced. In torsion mode, the SFM-tip vibrates laterally and in close proximity to the sample surface. Thus, an electrical contact between tip and sample can be established. In a series of reference experiments on standard surfaces, the working mechanism of scanning conductive torsion mode microscopy (SCTMM) was investigated. Moreover, I studied samples covered with free standing semiconducting polymer nano-pillars that were developed in the group of Dr. P. Theato (University Mainz). The application of SCTMM allowed non-destructive imaging of the flexible surface at high resolution while measuring the conductance on individual pillars.

In order to study light induced electrical effects on the level of single nanostructures, a new SFM setup was built. It is equipped with a laser sample illumination and placed in inert atmosphere. With this photoelectric SFM, I investigated the light induced response in functionalized nanorods that were developed in the group of Prof.

Abstract

R. Zentel (University Mainz). A block-copolymer containing an anchor block and dye moiety and a semiconducting conjugated polymer moiety was synthesized and covalently bound to ZnO nanorods. This system forms an electron donor/acceptor interface and can thus be seen as a model system of a solar cell on the nanoscale. With a KPFM study on the illuminated samples, the light induced charge separation between the nanorod and the polymeric corona could not only be visualized, but also quantified.

The results demonstrate that electrical scanning force microscopy can study fundamental processes in nanostructures and give invaluable feedback to the synthetic chemists for the optimization of functional nanomaterials.

Contents

1 Introduction

For many years, organic electronics and scanning probe microscopy developed independently. Whereas electric charge conduction in organic compounds was a topic for physical chemists, the first scanning probe microscopes were developed by engineers and physicists.

The first investigation on charge conduction in organic compounds dates back to 1906, when the Italian physical chemist Alfredo Pochettino observed photoconductivity in anthracene [Poc06]. More than twenty years later, the first scanning probe microscope was introduced by the German engineer Gustav Schmaltz [Sch29]. For his "physical and physiological" investigation of surface roughness, he developed a surface stylus profilometer that already had many features of a modern scanning force microscope. A stylus made of agate mounted at the end of a compliant bar was scanned over a surface structure. Topographic features caused a deflection of the stylus which was detected by a light beam reflected from a mirror on top of the stylus head. The traces of the light beam were recorded on photographic paper and thus, a magnification of the surface structure by a factor of almost 400 was achieved (see figure 1.1).

The big breakthrough for both fields, however, came fifty years later. In the early 1980s Gerd Binnig, Heinrich Rohrer, Christoph Gerber and Edmund Weibel reported on their first experiments with the scanning tunneling microscope (STM) at the IBM Zurich Research Laboratory in Rüschlikon, Switzerland [Bin82]. They used a fine metallic tip that was scanned over an electrically conductive surface at a constant tunneling current between tip and sample. With this method it was possible for the first time to image surface atoms on planar surfaces, such as the 7 x 7 reconstruction of Si(111) [Bin83]. Only four years after the first publication on STM, Gerd Binnig and Heinrich Rohrer received the Nobel Prize in physics (1986).

In March of the same year, one of the laureates, Gerd Binnig, published a paper together with Calvin F. Quate and Christoph Gerber in Physical Review Letters with the simple title "Atomic Force Microscopy" [Bin86]. They described a modified stylus profilometer with a sharp diamond tip mounted on a cantilever arm combined with a STM as a displacement sensor for the lever. A feedback mechanism regulated the vertical sample displacement in order to keep the force on the diamond tip constant. During their first measurements in air they already achieved a lateral and vertical
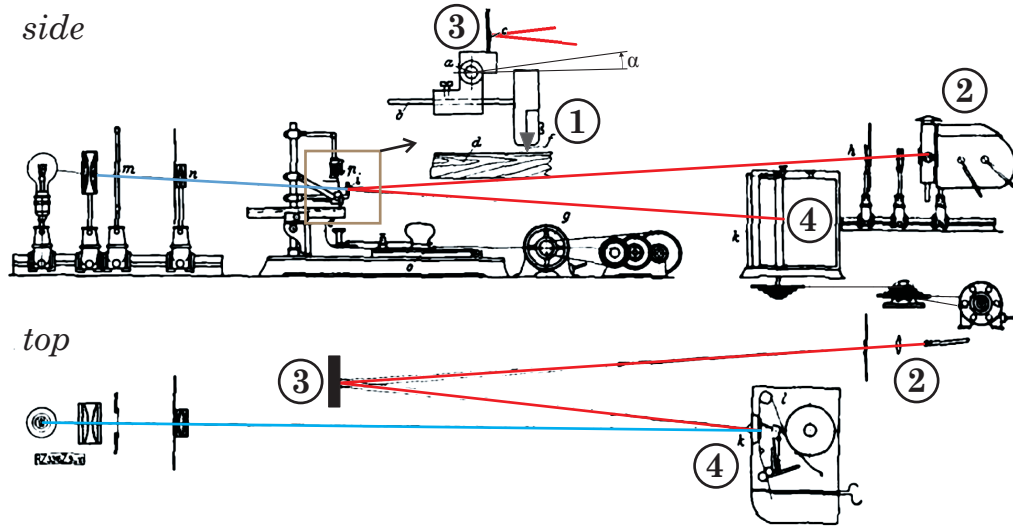
Figure 1.1: Side and top view of the surface stylus profilometer developed by Prof. Gustav Schmaltz in 1929 (modified original drawing from [Sch29]). A sample is moved by a motor underneath an agate stylus. Surface irregularities deflect the stylus by an angle of α (1). The deflection is detected by a light beam (2) reflected from the mirror (3) and projected on endless photographic paper in an "Edelmann" recorder (4). Additionally, a scale is projected on the paper by the optics on the left (blue line).

resolution of $3\,\mathrm{nm}$ and $0.1\,\mathrm{nm}$, respectively. This development solved a number of problems: First, it combined the wide applicability of the stylus profilometer with the high resolution capabilities of STM. Owing to the tunneling current feedback, STM can only be performed on electrically conductive samples. Second, the feedback mechanism could keep the tip - sample force at a constant level which reduced the tip wear and sample damage. Moreover, the force sensitivity of the setup was at least 10 decades higher compared to state-of-the-art surface profilers.

The breakthrough for organic optoelectronics came almost simultaneously in January 1986, when Ching W. Tang at the Eastman Kodak Research Laboratories published his results on the first two layer organic solar cell [Tan86]. The importance of this improvement can be compared to the introduction of the p-n junction for silicon solar cells by Daryl Chapin, Calvin Fuller and Gerald Pearson at the Bell Telephone Laboratories (New Jersey, USA) in 1954 [Cha54]. The p-n junction facilitated the spacial separation of electrons and the holes and thus, a power conversion efficiency of 6% was achieved. In a similar approach, Tang used an electron donor type organic material (copper phthalocyanine) and combined it with an electron acceptor type organic material (a perylene tetracarboxylic derivate) in a heterojuction type solar cell. Compared to state of the art organic photovoltaic cells at that time,

the new device architecture yielded an significantly high power conversion efficiency of 0.95%. Moreover, the device was - even for modern standards - very stable. After five days of continuous illumination with a tungsten light source under ambient conditions they reported less than 2% degradation in open circuit voltage and short circuit current.

In the following years, the atomic force microscope (AFM, or scanning force microscope, SFM[1]) matured to a standard surface characterization technique. It "learned" to distinguish between different surface properties, such as photo voltage [Wea91], work function [Non91] or charge injection [Mur93]. With these capabilities and the continuing trend towards interdisciplinary research, more and more questions coming from organic electronics were answered with scanning probe methods.

At the same time, the field of organic electronics and photovoltaics has matured from a basic research topic into one of the most promising technologies for cheap and flexible electronics of the near future. The material parameters of organic semiconductors make thin and flexible device architectures possible. Proposed production procedures, such as roll-to-roll printing on plastic foil can easily be done with existing technologies at speeds of some hundred meters per minute. The organic solar cell company Konarka has recently bought a printing facility from polaroid in New Bedford, Massachusetts, that can print organic solar cells at a speed 100 feet per minute. Thus, the machine allegedly achieves a capacity of $1\,GW$ per year[2]. So the easy scalability of the the production procedures is a big advantage for wide spread use of organic electronics, as mass production will lead to affordable devices. The first applications will be mainly in the field of life style products, where the easy and flexible nature of organic solar cells is of great advantage. On the long run, broader applications and even rooftop solutions will be available that offer a sustainable alternative to fossil fuels.

However, there is still a lack of basic understanding on fundamental processes. Compared to inorganic systems, such as the well established silicon solar cells, organic devices still yield much lower efficiencies and limited lifetimes. The joint efforts of theoretical and experimental physics, physical and synthetic chemistry together with the industry have already lead to major improvements and recently to a power conversion efficiency of 7.7% (tandem organic solar cell [Uhr10]). In spite of that, the exact reasons for the restricted efficiency and lifetime are still not sufficiently understood.

---

[1]The original term "atomic force microscopy" is in my opinion misleading. The forces detected by this method do in most cases not originate from single atomic structures but merely from the collective interaction with thousands and millions of atoms. Gravity, for example, also originates in the interaction of atoms, however, nobody would call it an "atomic force".

[2]Konarka press release on October 7th, 2008 (`www.konarka.com`).

1.1 Motivation

The aim of this work was to evaluate the capabilities of electric modes in scanning probe microscopy for contributing to the basic understanding of organic optoelectronics, in particular for organic photovoltaics. In numerous collaborations within the international research training group (IRTG) "Self Organized Materials for Optoelectronics" I was able to identify problems of organic electronics that can be answered by means of SPM methods. Here, it turned out that the existing operation modes were not sufficient for the specific properties of organic optoelectronic structures. In particular, strong tip-sample interactions due to the highly localized character of the measurements can lead to modifications in the sample structure and even to the complete loss of a specific functionality. Douhéret and co-workers, for example, reported that a thin film of an organic photovoltaic blend (P3HT:PCBM) turned into an insulator upon scanning the sample at a bias voltage of 1 V (see figure 1.2, [Dou07b]).

Next to tip induced sample degradation, organic electronic structures are very sensitive towards degradation when exposed to oxygen and humidity, in particular in combination with light. Therefore, new SPM operation modes and experimental setups that are suitable for the application on soft and sensitive electronic nanostructures had to be developed and tested.

SPM based methods are very versatile tools for studying surface properties. In organic electronics, however, specific functionalities are often found in the complex interface regions between subsequent layers inside the device. The investigation of the top surface of such a device yields only a small part of the working mechanism of such systems. Therefore, new sample preparation procedures were necessary for making these internal interface structures accessible for SPM.
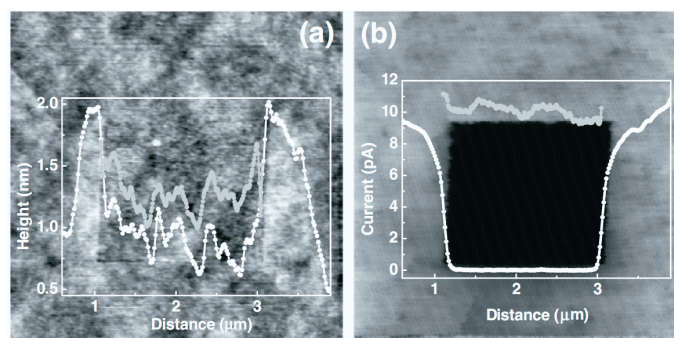
Figure 1.2: Topography (a) and current map (b) on a organic photovoltaic blend system (P3HT:PCBM, 1:1, as cast) on a transparent conductive substrate (ITO). Images from [Dou07b].

1.2 Outline

In **chapter 2** I will explain briefly the fundamentals of charge conduction from the very basic Drude model to the band type conduction. I will demonstrate that the principles derived for perfect crystalline materials can in parts be applied for disordered organic materials, as well. This more fundamental part will be followed by an introduction to the principles of photovoltaics. Starting with a general description on metal - insulator and heterojunctions (e.g. at a p-n junction), the well studied field of inorganic solar cells will be compared with photovoltaic organic systems. Finally, the concept of the bulk heterojunction and the field of hybrid or dye sensitized solar cells will be discussed.

In **chapter 3** the principles of scanning probe microscopy are introduced. After describing different strategies for force detection in static and dynamic scanning force microscopy, the detectable forces and their specific length scales are discussed. This more fundamental part is followed by an introduction to electrical operation modes, namely conductive scanning force microscopy (C-SFM) and Electrostatic- and Kelvin probe force microscopy (EFM and KPFM). In the context of C-SFM, a more detailed introduction into charge injection will be given and examples for applications on organic electronic systems from the literature will be discussed. Finally, the capabilities of KPFM and examples from the literature are introduced.

In **chapter 4** my investigations on hybrid solar cell structures will be presented. The working principle of a nano-composite for a novel blocking layer architecture was tested by an electrical SFM study. With KPFM, the working principle of the preparation procedure was studied and with C-SFM the nanoscale conductive structure of the composite was visualized. Furthermore, I will present my results of a C-SFM study on the internal structure of a hybrid solar cell prepared in a novel one-pot preparation procedure. In order to get insights into the internal structure, a cross cut was prepared by focused ion beam polishing.

In **chapter 5** the first systematic studies on the novel operation method of scanning conductive torsion mode microscopy (SCTMM) will be presented. I will demonstrate the working mechanism by a couple of fundamental experiments on reference surfaces. Thereafter, the application of SCTMM on fragile nano-pillar arrays made of a novel cross-linkable and a standard semiconducting polymer. Finally, the charge injection mechanism and the transport properties of the material are elucidated by a detailed analysis of a current voltage characteristic recorded on a single nano-pillar.

In **chapter 6** the new Photoelectric SPM setup will presented that was specifically modified for the study of organic optoelectronic systems. With this setup it will be possible to study the light induced nanoscale response of organic optoelectronic nanostructures. In particular, I will discuss the charging on a system of nanoparticles

that were functionalized with a semiconducting polymer under laser light irradiation. With KPFM, the charging could be visualized and quantified on the the level of single particles.

Finally, I will give some concluding remarks and outline future projects with the new tools introduced in this work in **chapter 7**.

2 Fundamentals

2.1 Charge Conduction

In this section some basic principles of charge conduction in solids will be presented. Starting with the classical description of the free electrons given by the Drude theory, the band model and its implications for the conduction in ideal crystalline materials will be explained. Finally the charge conduction in organic materials and specific similarities and differences to the ideal systems will be discussed.

2.1.1 The Drude Model

One of the most basic and straight forward theories for charge conduction is the model proposed by Drude in 1900 [Dru00]. It is based on the assumption that the charge carriers in an electrically conducting material can move freely, i.e. without interaction with other charge carriers. Under the influence of an external electric field charge carriers are accelerated. After an average time of τ the acceleration is stopped by a collision with a defect or the interaction with a lattice vibration (phonon)[1]. The charge carrier is assumed to lose its "memory" after the collision, i.e. the direction and the magnitude of the velocity before and after the scattering event are uncorrelated. This assumption is taken into account by an average drift velocity $\hat{v}$ at which a charge carrier (charge q, effective mass m^*) travels through the material under the influence of an electric field E. It is given by

$$\hat{v} = \frac{q}{m^*} \cdot \tau \cdot E := \mu E \; ; \;\; \mu = \frac{q\tau}{m^*} \tag{2.1}$$

The charge carrier mobility μ is a quantification of how free charge carriers can move in a material. Most metals and semiconductors with a well ordered crystalline structure can have mobilities of $50\,\mathrm{cm^2\,V^{-1}\,s^{-1}}$ (typical metals) up to $77000\,\mathrm{cm^2\,V^{-1}\,s^{-1}}$

---

[1]The original Drude model was assuming collisions with the lattice ions as a source for charge carrier scattering. Quantum mechanics, however, taught us that the electrons do not interact with a perfect crystal lattice. Instead, deviations from the periodic potential (i.e. phonons or defects) can cause scattering. Although that specific assumption was wrong, the actual scattering mechanism is not important for the theory, as long as there is *some* form of scattering that is considered in terms of the scattering time τ.

(Indium Antimonide). In organic electronic materials the mobility is much lower, typically ranging from 10^{-6} to $10^{-3}\,\mathrm{cm^2\,V^{-1}\,s^{-1}}$. The current density j is given by the charge carrier density n, the charge q and the average velocity ($q\tau E/m^*$) of the charge carrier:

$$j = \frac{nq^2\tau}{m^*}E \;=\; nq\mu E \;=\; \sigma E \tag{2.2}$$

This equation represents Ohm's law, where $\sigma = nq\mu = nq^2\tau/m^*$ is the electrical conductivity.

To this point, the exact nature of the charge carriers has been neglected. The conduction usually takes place either by negatively charged electrons ($q = -e = -1.602 \cdot 10^{-19}\,\mathrm{C}$), by positively charged electron vacancies (so called holes) or by a combination of both. Whereas in pure inorganic metals and intrinsic semiconductors the electron conduction is dominant, most organic electronic materials are hole conductors. Equation 2.2 also demonstrates that a good conductor can either have a high charge carrier density or highly mobile charge carriers (ideally both). A material of low intrinsic charge carrier density (for example intrinsic semiconductors) can still have excellent transport properties in terms of a high mobility μ for externally injected or photogenerated charge carriers.

Although this model is a classical description for the electrical current that neglects the quantum mechanical structure of the electrons and atoms involved, it can still explain many properties of metals qualitatively, such as the just mentioned Ohm's law or the temperature dependence of the metallic conductivity (Wiedemann-Franz law). More detailed theories of charge conduction involve the quantum mechanical properties of the electron as well as the periodicity of a crystal lattice. This description leads to the band structure of the electronic system.

Although most organic materials do not have the periodicity of a crystal lattice, their behavior can - to a certain degree - also be described by the band model. However, the complete derivation of the mathematical description is way beyond the scope of this thesis. It can be found in any textbook on solid state physics (e.g. [Ash76]). I will therefore restrain the description to the main conclusions of the band model.

2.1.2 Quantum Mechanic Description: Band Model

Within the Drude theory, electrons are described as localized particles that can move freely through the crystal lattice. In quantum mechanics, the electron is described in terms of a wave function

$$\Psi(\vec{r}) = Ce^{i(\vec{k}\cdot\vec{r})}. \tag{2.3}$$

$\vec{k}$ indicates the propagation direction of the wave and is coupled to the momentum $\vec{p}$ of the electron (e.g. in the free electron case by $\vec{p} = \hbar\vec{k}$; $\hbar$: Planck constant). In an isolated atom, the electrons occupy the discrete energy levels of the atomic orbitals. In a solid, atoms are packed close enough together that their atomic orbitals overlap. Thus, the outer electrons are no longer localized to their specific atom. Their wave functions can spread over many atomic distances, depending on the degree of order in the solid. In an ideal crystal, the potential $U(\vec{r})$ formed by the ion cores has the same periodicity as the crystal lattice. The Schrödinger equation for such a system is given by

$$\frac{\hbar^2}{2m}\nabla^2\Psi(\vec{r}) - U(\vec{r})\Psi(\vec{r}) = E\Psi(\vec{r}) \tag{2.4}$$

(E: energy eigenvalue of the wave function). According to Bloch's theorem, solutions to equation (2.4) have the form

$$\Psi(\vec{r}) = u_k(\vec{r})e^{i(\vec{k}\cdot\vec{r})}, \tag{2.5}$$

with a periodic function $u_k(\vec{r})$ having the same periodicity as $U(\vec{r})$. This periodicity of $u_k(\vec{r})$ implies that the wave function spreads over the whole periodic structure of the crystal, i.e. the electron is delocalized. In non-ideal systems, grain boundaries and lattice defects localize the wave function to smaller regions of the solid. As a further consequence, solutions to (2.4) do no longer occupy discrete energy levels E. They split up and form quasi-continuous energy bands separated by gaps of forbidden energies. In these energy gaps there are no solutions to the Schrödinger equation and thus no electron with this energy can exist in the solid.

The occupation of the states in the energy bands is determined by the Fermi-Dirac statistics. The probability p to find a filled energetic state at an energy E is given by

$$p(E) = \frac{1}{1 + exp(\frac{E - \epsilon_F}{k_B T})} \tag{2.6}$$

(k_B: Boltzmann constant, T: absolute temperature, ϵ_F: Fermi energy). One implication from this formula is that at a temperature above $0\,\mathrm{K}$, the probability to find an energetic state at the Fermi energy occupied is $1/2$. For all other states above ϵ_F there is a non-zero probability to find this state occupied. Fully filled energy bands below ϵ_F are called *valence bands* and partially filled or empty bands above the Fermi energy *conduction bands*. If an external electric field is applied to the crystal, transitions take place between states of the same energy and different $\vec{k}$. Thus, a net motion of the electron gas in the material can take place: an electrical current. In a material with good charge transport properties, a large number of both occupied and unoccupied states exist close to ϵ_F. Here, the position and the size of the band gap plays an important role. There are three cases:
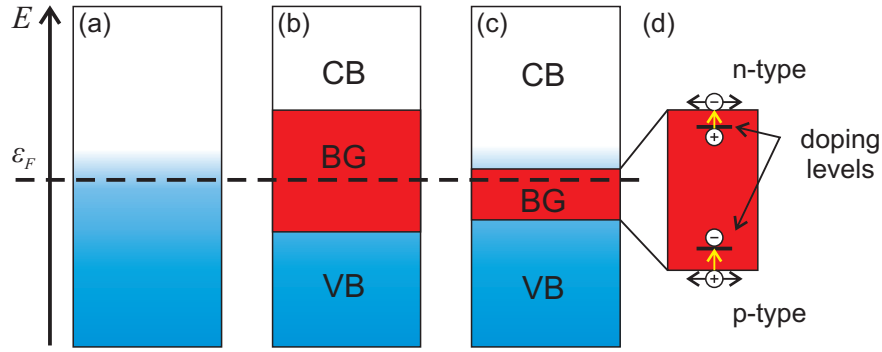
Figure 2.1: Energy diagram of a metal (a), an insulator (b) and a semiconductor (c). CB and VB indicate the conduction and valence band, respectively and BG the band gap. The effect of doping is illustrated in (d). Dopants can generate additional energetic states in the bandgap. By thermal activation, mobile charge carriers are generated.

(a) In *metals* (Fig. 2.1) the Fermi energy is located outside of a band gap. Thus, a large number of very mobile states exist close to ϵ_F (figure 2.1 (a)).

(b) *Insulators*: Here, the band gap is large compared to the thermal energy ($k_B T \approx$ 0.025 eV at room temperature). Thus, the valence band is fully occupied and the conduction band is empty (figure 2.1 (b)).

(c) *Semiconductors*: The band gap is sufficiently narrow and electrons can be thermally excited from the valence band to the conduction band, leaving an electron vacancy or hole in the valence band (figure 2.1 (c)).

The exact distinction between insulators and semiconductors is difficult. Generally, materials that exhibit observable conductivity at room temperature and turn into an insulator at low temperatures are classified as a semiconductor. If the only sources for conduction are thermally excited charge carriers, the material is classified as an *intrinsic* semiconductor. However, free charge carriers in a semiconductor do not necessarily have to originate from thermal excitations. Impurities and grain boundaries in the crystal also influence the conduction behavior.

By deliberately doping the semiconductor, the conductive properties of the material can be fine-tuned. For example by incorporating an arsenic atom (valence 5) in a germanium crystal (valence 4), an additional electron is provided. In this case, the arsenide acts as an electron *donor*. Analogously, an atom of valence 3 (e.g. gallium) provides one electron less to the crystal, which makes it an electron *acceptor*. The impurities provide additional electronic states that support thermal excitations into the conduction band (donors) or from the valence band (acceptors) and thus create mobile charge carriers. Depending on the type of charge carriers, donor type doped

materials are called *n-doped* and acceptor type doped materials *p-doped* (see figure 2.1 (d)).

2.1.3 Charge Conduction in Organic Materials

Most of the materials used in organic electronics consist of chain-like molecules with repeated molecular units (monomers) that are linked by covalent bonds. The number of repeating units ranges from only a few (small molecules) over 5 - 30 (oligomers) up to hundreds and thousands (polymers). They are linked together by covalent bonds, predominantly formed by carbon atoms (sometimes also with nitrogen, oxygen or sulfur atoms). The structure of the bonds forming the backbone of the molecule has a big influence on the electronic properties of the material. In a molecule that predominantly consists of sp^3 hybridized carbon atoms forming σ bonds, all available electrons are tied up and thus localized to their specific bonds. An example of such a molecule would be polyethylene, a well known electrical insulator (figure 2.2 (a)).

Figure 2.2: (a) σ bond and the chemical structure of polyethylene. (b) π bond and the chemical structure of the conjugated polyacetylene.
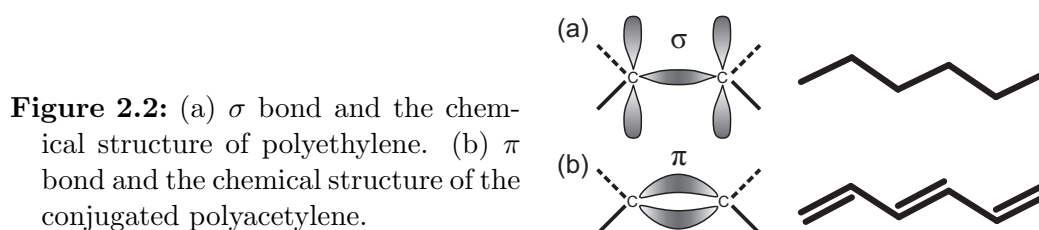
In a sp^2 hybridized system, the electrons are much less localized and adjacent π bonds in the molecule overlap. Thus, the electrons can form a delocalized (conjugated) π orbital along the backbone (figure 2.2 (b)). The energetic levels in this π system can be described similar to the afore-mentioned band model in inorganic materials. The energetically highest occupied molecular orbital (HOMO) corresponds to the upper edge of the valence band and the lowest unoccupied molecular orbital (LUMO) corresponds to the lower edge of the conduction band. The energies in between these bands are forbidden energies, comparable to the bandgap in inorganics. The electrical and optical properties of these materials are mainly governed by the HOMO and LUMO states. The most simple example for such a conjugated system would be polyacetylene (figure 2.2 (b)). Some examples of more complex conjugated systems are given in figure 2.3. Important classes of conjugated polymers are polythiophenes and poly triphenylamines as hole conductors and fullerene derived materials such as [6,6]-phenyl-C_{61}-butyric acid methyl ester (PCBM) or poly-2,7-(9,9'-dioctyl-9H-fluorene)-alt-4,9-benzol[c][1,2,5]-thiadiazole (F8BT) as electron conductors [Boe08].

Most of these compounds are intrinsic semiconductors. In order to increase conductivity, mobile charge carriers have to be generated. This can be done externally

(a) (d)

(b)

(c)

(e) (f)
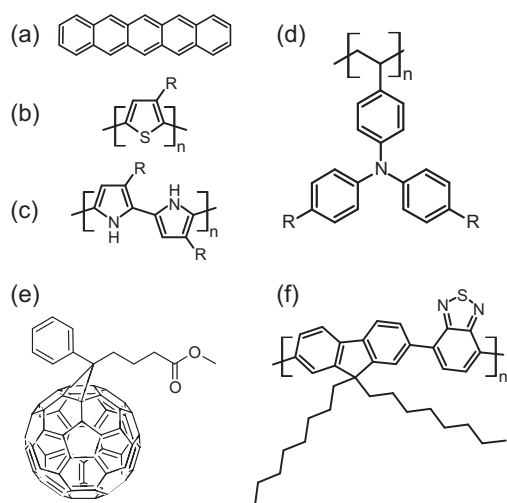
Figure 2.3: Structures of important organic electronic molecules: (a) pentacene, (b) polythiophene, (c) polypyrrole, (d) polytriphenylamine, (e) PCBM, (f) F8BT.

by charge injection or photo excitation or internally by doping the materials. An example for the latter mechanism is the intrinsically conductive polymer mixture of poly(3,4-ethylenedioxythiophene) and poly(styrenesulfonate) (PEDOT:PSS; see figure 2.4 and [Kir05]). Part of the sulfonyl groups on PSS are deprotonated and carry a negative charge. This leads to a partial oxidation and a rearrangement of the double and single bonds in the thiophenes in the PEDOT. Owing to the conjugated structure, the positive charge (in other words: the hole) can now move freely along the backbone of the molecule.
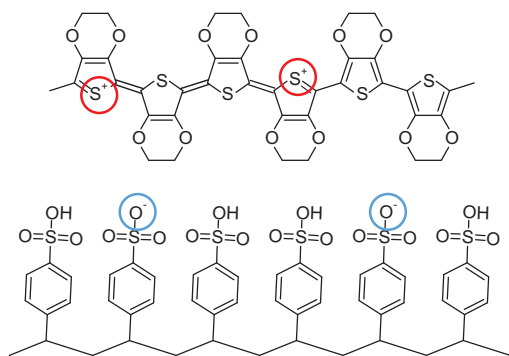
Figure 2.4: Structures of the conductive polymer composite of Poly(3,4-ethylenedioxythiophene) (top) and poly(styrenesulfonate) (bottom). The partial deprotonation of the sylfonyl groups in the PSS (blue circles) generates positive charges in the backbone of the polythiophene (red circles).

In inorganic materials, the electronic wave functions can be delocalized all over the three dimensional crystalline domain. In isolated molecules this delocalization is restricted to the one-dimensional backbone of the molecule. However, thanks to the molecular packing in the bulk phase, the π orbitals of adjacent molecules can overlap. Thus, electrons can be exchanged between these molecules. Depending on the degree of order in the material the charge transport can be described by a band like transport (highly purified molecular crystals) or by hopping between localized states (amorphous polymeric materials)[Pai70, Tes09]. In the latter case, the free

electron assumption of the Drude model no longer holds. This is, for example, reflected in an electric field dependence of the charge carrier mobility, for example by a Poole-Frenkel type transport, where the mobility can be described by

$$\mu(E) = \mu_0\, exp(\sqrt{\frac{E}{E_0}})\,;$$
(2.7)

μ_0 is the zero field mobility and E_0 the electric field coefficient [Ham88, Blo97, Cam99]. Furthermore, statistically defined parameters as the Fermi energy (equation (2.6)) become more and more undefined, as the energetic disorder and the localization of the charge carrier states increase [Sco03].

The microscopic structure or *morphology* and thus the degree of overlap ($\pi - \pi$ stacking) of adjacent molecules is strongly influenced by the overall structure and - in particular - by the side chains of the molecule. By exploiting the self organizing properties of tailored molecules, crystalline structures with an ideal molecular packing can be fabricated. Compared to inorganic crystalline materials however, the coupling of the electrons and thus their mobility is still much weaker in organic materials. Therefore, the molecular packing on the order of several tens to thousands of molecules, i.e. the structure on the length scale of $1 - 100\,\mathrm{nm}$ plays an important role for the overall performance of the material [Gir10].

2.2 Organic Photovoltaics

So far, the direct comparison of inorganic to organic electronics revealed the superiority of the classical inorganic compounds in terms of material parameters such as conductivity and charge carrier mobility. However, there are good reasons for the use of organic materials for electronic applications that have been discussed already in the introduction part. Material properties such as high optical absorption coefficients and the possibility to use ink jet or roll-to-roll printing techniques make thin, flexible and - finally - cheap device architectures possible.

The field of organic electronics is very broad, from cheap logic circuits over organic light emitting diodes (OLED) to solar cells. Here, I will restrain the discussion to the field of organic photovoltaics. To further understand the role of all the materials and their properties for the fabrication of an efficient organic solar cell, I will have a closer look on the charge generation mechanism in organic and inorganic solar cells. Both systems have in common that the charge separation is facilitated by a junction between materials of different electronic properties. Therefore, I will start by introducing the concept of the heterojuction before discussing the charge separation at such an interface.

2.2.1 Metal - Insulator- and Heterojunctions

An important parameter for the description of effects on surfaces is the *work function* Φ. It is defined as the minimum energy required to remove an electron from the solid. In metals, the work function is given by the difference between the Fermi and the vacuum energy (i.e. the energy of an electron far away from the solid, see figure 2.5 (a)). In semiconductors it is defined by the difference between the highest occupied mobile state and the vacuum energy, i.e. the upper edge of the valence band for p-type (sometimes also called *ionization potential* ϕ_I) and the lower edge of the conductance band for n-type semiconductors (sometimes also called *electron affinity*; figure 2.5 (b)).
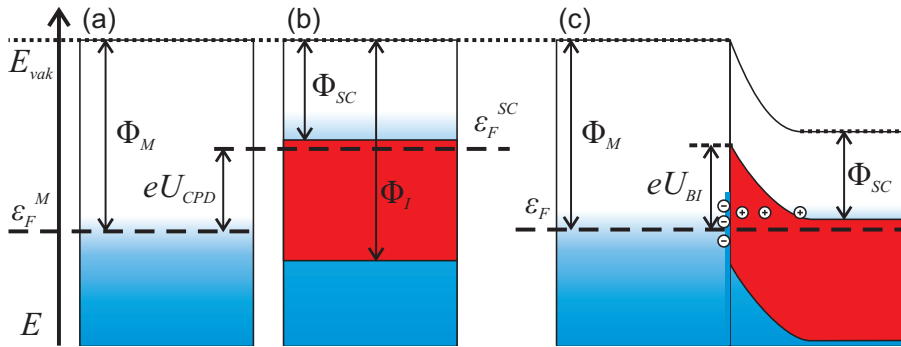
Figure 2.5: Energy diagram of a metal (a) and a n-type semiconductor (b) separated by a small gap. The difference in Fermi levels is called the contact potential difference eU_{CPD}. A metal - insulator junction is shown in (c). Fermi level alignment leads to an exchange of charge carriers and the formation of a space charge layer. In the semiconductor this leads to band bending. This type of junction is also called a Schottky barrier. It shows a rectifying behavior and is thus used for diodes (Schottky diode).

When two different materials are brought to contact, charge carriers can be exchanged at the interface by a combination of drift and diffusion. They will diffuse from the material with higher Fermi energy to the material with lower Fermi energy. Thus, charges accumulate at the interface and give rise to an electrical field that generates an opposite drift motion of charge carriers. In equilibrium both currents cancel out each other and the electric potential Φ_{bi} generated by the excess charges equals the difference in the Fermi energies:

$$\Phi_{bi} = e \cdot U_{bi} = \epsilon_F^M - \epsilon_F^{SC}. \tag{2.8}$$

This potential is also called the *contact potential difference* of the two materials or the *built in potential* of the junction[2]. In the case of the metal and the insulator

---

[2]The potentials that are mentioned here are all with respect to one electron. Thus, the electric potential or voltage of one electron is given by $U_{bi} = \Phi_{bi}/e$.

in figure 2.5 a and b electrons from the conduction band of the semiconductor can reduce their energy by diffusing into the metal. Owing to the high density of mobile charge carriers, the inside of a metal is always field free (the principle of the Faraday cage). Therefore, the negative charge accumulates directly at the interface, whereas in the semiconductor an oppositely charged space charge layer is formed. In this region, the mobile charges have moved to the metal. Thus, this region is called the *space charge* or the *depletion zone.*

The electric field leads to a deformation of the band structure called *band bending.* In the case of a pure semiconductor junction (*heterojunction*), the depletion zone extends to both compounds. The properties of these interface layers strongly determine the electrical properties of the junction.

2.2.2 Photo Induced Charge Separation

The structure of an inorganic solar cell is shown in figure 2.6 (a). It consists of a heterojunction between a p-type and a n-type semiconductor (p-n junction). The absorption of a photon of sufficiently high energy leads to the formation of a coupled electron-hole pair, an *exciton.* Owing to the high dielectric constant in inorganic materials, this excitonic coupling is relatively weak (in the order of $k_B T \approx 0.025\,\text{eV}$) and the excitation is almost directly dissociated into free charge carriers. Via a combination of diffusion (outside the depletion zone) and drift (due to the electric field in the depletion zone) the charges are separated and can be collected by the electrodes. The charge carrier collection is the crucial part in inorganic semiconductors, as the majority charge carriers have to be collected before they are able to recombine.

In the case of organic semiconductors, photo generated excitons are more difficult to separate into free charges. The low dielectric constant and the higher degree of localization lead to binding energies in the order of $0.1 - 1\,\text{eV}$, significantly higher than the thermal energy $k_B T$ [Cam96, Bre96]. Thus, an additional force is required to separate the charges. By combining an electron conducting (electron acceptor type) and a hole-conducting (electron donor type) material, the charge separation is facilitated (figure 2.6 (b)). Well studied systems are combinations of a polythiopene, such as Poly(3-Hexylthiophene) (P3HT) as donor, and the fullerene derivative PCBM ([6,6]-phenyl-C_{61}-butyric acid methyl ester) as acceptor.

At the interface between donor and acceptor, excitons are dissociated into an electrostatically coupled charge transfer state and finally into a charge separated state with a free electron and and a free hole (figure 2.6 (b) step 3). Owing to the strong localization, excitons can only exist for a certain span of time, the exciton lifetime τ_E, before recombination takes place. Typical values for τ_E are in the order of pico- to
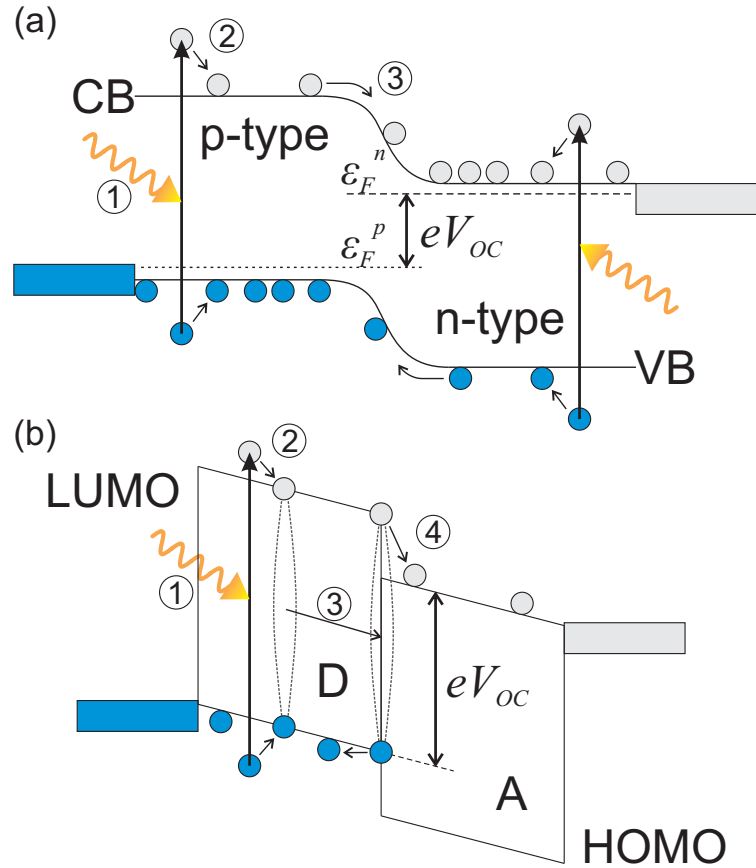
Figure 2.6: Energetic diagram of an inorganic (a) and an organic solar cell (b). The charge separation mechanism starts in both systems with the absorption of a photon (1), exciting an electron (gray circle) from the valence band (VB) to the conduction band (CB) and leaving a hole (blue circle). The subsequent relaxation leads to the formation of an exciton (2). In the inorganic system, typical thermal energies are sufficient to dissociate the exciton into free charges. Finally, the electric field at the depletion zone in the p-n junction separates electrons and holes. In the organic solar cell (b), the exciton (2) is much more stable. In order to be separated, it has to find a donor-acceptor junction by diffusion (3), where it can be separated (4). Owing to the electric field generated by the work function offset of the electrodes, the separated charges drift towards their respective electrodes. Here, the absorption takes place in the electron donor material (D); the same mechanism would apply for absorption in the acceptor (A). Adapted from [Kip09].

nanoseconds (e.g. for the donor type polythiophene derivate P3HT: 400 ps [Sha08]). Owing to the lower energy of the charge transfer state, the exciton dissociation at the donor-acceptor heterojunction is very efficient (timescale $\approx 50\,$fs [Bra01]). Once separated, the charge carriers drift towards the electrodes under the influence of the electric field generated by the work function offset of the electrodes. Thus, the proper choice of the electrode material plays another crucial role in the development of efficient device architectures.
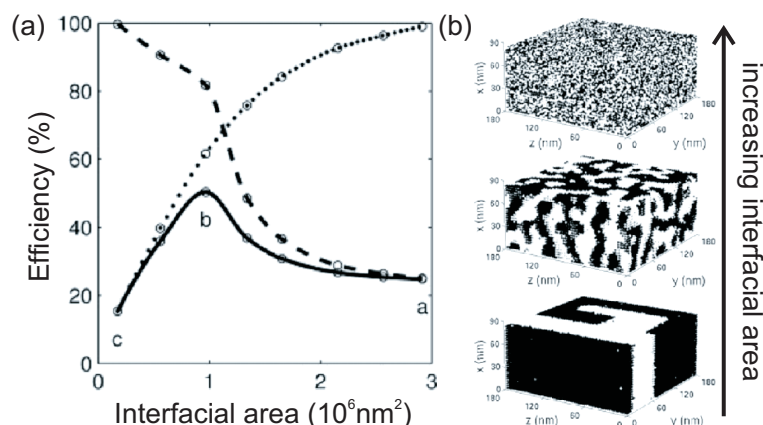
2.2.3 Bulk Heterojunction

One of the the key processes in organic photovoltaics is to get the exciton close to a heterojunction before it is able to recombine. Close in this context means within the exciton diffusion length $L = (D\tau_E)^{1/2}$ (D: diffusion coefficient), which is generally in the order of $5 - 20\,$nm. For P3HT, Shaw and co-workers have determined the diffusion coefficient D by time resolved fluorescence measurements. They found a value of $(1.8 \pm 0.3) \cdot 10^{-3}\,$cm^{2}s^{-1} [Sha08]. With a typical exciton lifetime of $\tau_E = 400\,$ps they estimated the exciton diffusion length to be $(8.5 \pm 0.7)\,$nm.

Although organic electronic materials have high absorption coefficients compared to inorganic materials (in the order of $10^5\,$cm^{-1} [Blo07]), a simple bilayer structure with thicknesses in the order of the exciton diffusion length would be too thin to absorb enough light. In the P3HT case (absorption coefficient: $\alpha = 8 \cdot 10^4\,$cm^{-1} at a wavelength of 550 nm [Sha08]), the absorption in a 10 nm thick layer would only absorb 15% of the incident light (assuming total reflection at the substrate and thus a double pass).

In order to maintain an efficient exciton dissociation in thicker films, additional interface roughness between donor and acceptor material is required. This concept is called a *bulk heterojunction* as the donor/acceptor heterojunction is distributed throughout the "bulk" of the active layer. An important issue in this approach is to have every part of the active material connected to is respective electrode (often referred to as *percolation*). Isolated islands of donor material in the acceptor matrix and vice versa lead to charge trapping and thus reduce the overall efficiency of the device. If the percolation paths are too long, the probability of charge carrier recombination increases and the performance is again decreased. Thus, the optimum morphology is a compromise between high interfacial area and minimum percolation length.

Watkins and co-workers have studied this trade-off by simulating the exciton dissociation in a bulk heterojunction (see figure 2.7, [Wat05]). They generated a number of morphologies with different degrees of phase separation between a donor- and an acceptor-type material. Excitons were placed at a constant rate at random locations

Figure 2.7: (a) Monte Carlo simulations of the quantum efficiency (charge that reaches the electrode per absorbed photon) in a bulk heterojunction with different interfacial areas (examples are shown in (b)). With increasing surface area the exciton dissociation efficiency increases (dotted line), however, the charge collection efficiency is decreasing (dashed line). Thus, the total quantum efficiency (solid line) has a maximum with an optimum balance between efficient dissociation and good percolation (graphs taken from [Wat05]).

in the sample and their diffusion was simulated. The number of excitons that were able to reach an interface and dissociate per totally generated excitons defined the dissociation efficiency. The dotted line in figure 2.7 shows an increasing dissociation efficiency with higher interfacial area. The motion of the separated charges was also simulated. The number of charges that reached the electrode per separated exciton defined the charge extraction efficiency (dashed line in figure 2.7). It had its highest value at the minimum interfacial area. Here, every part of the sample was well connected to its respective electrode and the percolation paths were broad enough to minimize the chance of recombination. The total internal quantum efficiency, given by the number of charges extracted per generated exciton, is plotted as a solid line in figure 2.7 (a). It clearly shows that there is an optimum interfacial area with a maximum power conversion efficiency around 50%.

There are numerous ways to introduce and control the interface roughness. The easiest approach is to utilize the self organizing properties of the compound itself. By optimizing the molecular structure, e.g. by using block copolymers or different side groups, and the preparation conditions, such as solvent, spin/blade coating, annealing, etc., an optimal morphology with an interpenetrating network of the two components can be formed.

The percolation issue can be tackled by using a predefined geometry for the bulk heterojunction. Watkins and co-workers have also investigated such an "ideal" checkered

morphology and found a maximum quantum efficiency of 80% (figure 2.8), which is much higher than the 50% of the disordered bulk heterojunction (figure 2.7).

Figure 2.8: (a) Monte Carlo simulations of the quantum efficiency of an ideal checkered morphology (b). See also figure caption to figure 2.7.
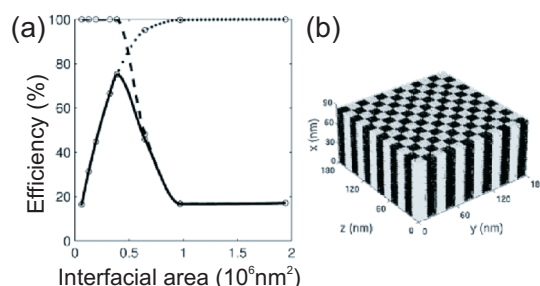
2.2.4 Hybrid Solar Cells

So called dye sensitized solar cells (DSSC) consist of a nanoporous oxide semiconductor (e.g. ZnO or TiO_2) as electron conducting part in combination with a dye molecule. In the conventional Grätzel type DSSC, a liquid electrolyte is used as hole-conducting part [O'R91]. With a power conversion efficiency of more than 10% this type of devices reaches the highest values in the field of organic solar cells so far. However, this concept also has disadvantages as the liquid electrolyte may evaporate fom a leaking device. As a replacement, p-type semiconducting polymers have been used. Altough this strategy reduces the power conversion efficiency to around 5%, it leads to more stable and reliable devices. Such systems containing both organic and inorganic materials are called *hybrid systems.*

Compared to fully organic systems, hybrid systems have a better environmental stability and the inorganic electron acceptor materials have higher electron mobilities. Furthermore, the band offsets can optimized more easily. However, the organic-inorganic interface still generates problems. For example the polythiophene P3HT forms a disordered phase in the direct vicinity of a ZnO interface. Disordered polymer domains significantly deteriorate the optical absorption and charge transport parameters, such as the exciton diffusion or the charge carrier mobility. One way to reduce these effects is to add a self assembled monolayer (SAM) to the organic-inorganic interface as for example demonstrated by Hsu and co-workers [Hsu10].

3 Scanning Probe Microscopy

The principle of the scanning probe involves a structure sensitive to surface properties that is moved over a specific area of interest. Such a probe can be the finger of a blind person reading the embossed printing of Braille, the needle of a record player "reading" the periodic structure of the sound waves pressed into the surface of the record, the stylus profiler that was mentioned in the introduction or the reading head of a hard disk, that is sensitive to modulations in the magnetic field on the surface. In this way, a stream of surface information is obtained, that can be reconstructed to a two dimensional map of surface properties. A scanning probe microscope that is able to quantify the probe-sample forces is called a *scanning force microscope.*

On the following pages, the fundamental aspects of scanning force microscopy, namely the operation modes and the relevant forces, are discussed. Thereafter, the electric operation modes used in this work are introduced. Furthermore, their potential towards application on organic electronics is demonstrated by examples from literature.

3.1 Scanning Force Microscopy

A very simple force sensor with high sensitivity can be designed by combining a micro mechanical cantilever structure with a nanometer sized tip (see figure 3.1 (a)). Together with a piezoelectric positioning system for the lateral (x,y) and the vertical (z) sample position, the system is called a *scanning force microscope* (SFM; also known as *atomic force microscope*, AFM [Bin86]). The force acting on the tip is determined by measuring the vertical bending of the cantilever, mostly via the deflection of a laser beam focused on the backside of the cantilever (figure 3.1 (b)). For small deflections, a linear dependence of force F to deflection Δx can be assumed, that is, $F = k \Delta x$, k being the spring constant of the cantilever.

3.1.1 Static and Dynamic Operation Modes

The surface topography can be obtained by scanning the surface in x and y direction and simultaneously maintaining a constant force on the cantilever by a feedback
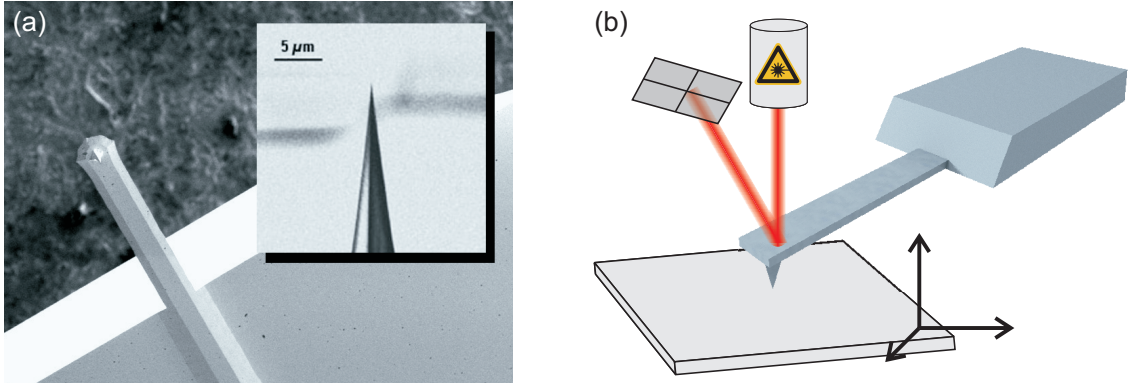
Figure 3.1: Electron microscopy of a SFM cantilever with tip (a) and SFM working principle (b).

mechanism that adjusts the z-position of the sample (constant force mode).There are several ways to monitor the force acting on the tip. The easiest way is to use the cantilever as a static force sensor by measuring the vertical deflection caused by the tip-sample forces. This operation mode is called *contact mode.* It has two major drawbacks: (i) due to friction the tip wears off very fast and (ii) on soft samples, even very low forces can lead to deformations and the destruction of the surface structure. Furthermore, lateral forces caused by the scanning of the tip are hard to control, as they do not directly translate into a vertical bending of the cantilever.

One strategy to overcome this problem is to actively vibrate the cantilever, ideally close to one of its resonance frequencies (dynamic operation of the SFM [Gar02]). Most commonly, vertical resonance modes are used [Mar87]. Alternatively, a torsional excitation of the cantilever can be used where the tip oscillates parallel to the sample surface (*torsion mode* [Kaw02, Hua04]). Vertical modes are sensitive to forces acting perendicularly to the surface whereas torsion mode operation is sensitive to in-plane interactions such as friction.

Far away from the surface, the cantilever motion can be described by a harmonic oscillator with $F_0(z) = k \cdot (z - z_0)$ (z_0: equilibrium position). Closer to the surface, the oscillator is disturbed by the tip-sample interaction F_{ts}. For a weak force field F_{ts} and small vibration amplitudes we can write the effective force as

$$F = F_0(z) \ + \ \left(\frac{\partial F_{ts}}{\partial z} \right)_{z_0} \cdot (z - z_0) \tag{3.1}$$

and thus

$$k_{eff} = -\frac{\partial F}{\partial z} = \left(k - \frac{\partial F_{ts}}{\partial z} \right)_{z_0}. \tag{3.2}$$

This modified spring constant translates to a shift of the (angular) resonance frequency by

$$\omega'_0 = \sqrt{\frac{k - \partial F_{ts}/\partial z}{m_{eff}}}, \tag{3.3}$$

where m_{eff} is the effective mass of the cantilever. Equation (3.3) shows that the resonance frequency of a SFM cantilever is influenced by the presence of a force field gradient.

Closer to the surface, the tip - sample interaction is no longer purely elastic and additional dissipative damping occurs. The amplitude of the oscillation is damped and the resonance frequency is shifted to lower frequencies:

$$A(\omega) = \frac{F_0/m_{eff}}{[(\omega_0^2 - \omega^2)2 + (\omega\omega_0/Q)^2]^{1/2}} \tag{3.4}$$

$$\omega'_0 = \sqrt{1 - \frac{1}{2\,Q^2}}. \tag{3.5}$$

Q is the quality factor of the resonator and quantifies the energy dissipation per oscillation cycle [Gar02].

There are two ways to exploit this knowledge for the force detection. One strategy is to observe the effect on the amplitude (*amplitude modulation*). Exciting the cantilever a fixed frequency close to ω'_0, the tip is approached to the surface until the target amplitude - the amplitude setpoint - is reached. Scanning the surface, a feedback adjusts the tip height to maintain a constant amplitude. The second strategy is to adjust the excitation frequency and the drive amplitude to have the cantilever vibrating at its momentary resonance frequency at a fixed amplitude (*frequency modulation* [Gar02]). For surface imaging, the feedback maintains a constant frequency shift.

If the tip vibrates vertically in the long range forcefield domain without physical contact with the sample during the scanning, the operation mode is called *non-contact mode*. True non-contact operation is hard to achieve in air; it is mostly used in ultrahigh vacuum conditions in combination with frequency modulation.

If the tip touches the surface during each oscillation, additional information about the local mechanical properties of the surface can be obtained from the phase shift between excitation and cantilever oscillation [Mag03]. This operation mode is called *tapping-* or *intermittent contact mode*. In combination with amplitude modulation, this is the most popular operation mode for experiments in ambient conditions.

The vertical vibration of cantilever and tip has two effects: First, the cantilever motion can be detected with high sensitivity by means of lock-in technology. Second,

the timescale of the tip-sample interaction becomes very short. Thus, the sample has no time to deform significantly and sample damage on soft samples is reduced.

With most commercial SFM systems and tips lateral and vertical resolutions in the order of $1 - 10$ nm and 0.1 nm are achieved under ambient conditions. Principally, SFM is capable of resolving single atomic [Gie95] and molecular structures [Gro09]. However, very clean surface conditions are required, as surface adsorbates such as water and hydrocarbons disturb the measurement. Although first examples of atomic resolution in liquid environments have been presented [Jar08, Yan10], most high resolution experiments are still performed in ultra high vacuum conditions.

3.1.2 Relevant Forces and Length Scales

At very small tip-sample separations ($d < 0.1$ nm), the repulsion of the surface atoms of tip and sample (chemical forces) and, at higher normal forces, elastic deformations in the contact area lead to a repulsive force on the SFM tip. This regime is called the contact regime. Under ambient conditions, adsorbed water on the surface leads to capillary forces, if the tip touches the surface. Depending on the humidity and the surface properties, this water layer is of the order of some monolayers up to some nanometers thick [Sti00, Men09].

At larger tip - sample separations long ranged electric forces dominate. Assuming an electrically conductive tip material, electrostatic forces can be described by a potential difference $\Delta V = V_{tip} - V_S$ between tip and sample. They can originate from work function differences, static surface charges or an externally applied bias voltage. For a first estimation of the electrostatic force, the tip - sample system can be simplified to a plate capacitor with capacity $C = \epsilon_0 A/z$ (z: tip position, $z = 0$: tip touches the sample surface). Here, the plate area $A = \pi R^2$ is given by tip radius R, neglecting contributions from the tip cone, and the cantilever (a more detailed description of the tip - sample capacitance is given in [Kur98]). Starting with the energy W of the capacitor, we obtain

$$W = \frac{1}{2}C\Delta V^2 = \frac{\epsilon_0 \pi R^2 \Delta V^2}{2z}$$
$$F_{ES} = \frac{\partial W}{\partial z} = -\frac{\epsilon_0 \pi R^2 \Delta V^2}{2z^2}. \tag{3.6}$$

The second long ranged electric interaction is the van der Waals force. It is caused by static and fluctuating dipole interactions between the atoms and molecules of tip and sample. In the case of a sphere of radius R at a separation z over a planar surface, the van der Waals force is given by [But03]

$$F_{vdW} = \frac{A_H R}{6z^2}. \tag{3.7}$$

A_H is the Hamaker constant. It depends on the dielectric properties of the materials involved. Similar to the electrostatic force, the van der Waals force shows a quadratic decay with respect to the distance.

Thus, by neglecting the interaction of the tip cone and the cantilever, the interaction of a SFM tip with the sample surface can be approximated by equation (3.7). In the case of a quartz sphere on a glass surface separated by dry air (typical configuration for SFM), the (non-retarded) Hamaker constant is $6 \cdot 10^{-20}$ J [But03]. For a sphere with $R = 10$ nm and a distance of 1 nm we obtain a force of $F_{vdW} = 10^{-10}$ N $= 100$ pN. The electrostatic force for this geometry calculated from equation (3.6) with a typical contact potential difference of 300 mV yields a similar force of 130 pN. Considering the identical decay behavior of equations (3.6) and (3.7) the forces should still be similar far away from the surface.

However, on distances larger than $2 - 5$ nm, so called retardation effects come to play for the van der Waals force and cause a decay faster than $1/z^2$. The reason for the retardation is the finite time $t = 2z/c$ (c: velocity of light) that the electric field of a fluctuating dipole needs to cross the gap between the two solids. Thus, faster components of the fluctuations cannot interact with the molecules on the other side of the gap any more. This limits the bandwidth of the electrical interaction and thus the total force [Par06].

Figure 3.2: Simulation of the distance dependent resonance frequency shift of an oscillating SFM tip(from [Gug00]). The authors used a spherical tip apex and a conical tip.
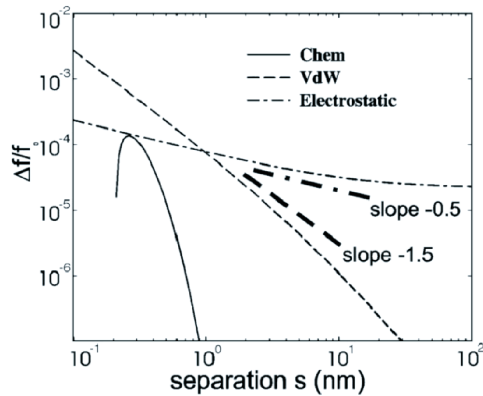
For distances smaller than 2 nm equation (3.7) is still valid and retardation does not play a role. For larger distances, the decay becomes faster. Thus, after $5 - 10$ nm the van der Waals force is mostly negligible compared to the electrostatic force. In figure 3.2 a simulation by Guggisberg and co-workers of the distance dependent resonance frequency shift of a conical tip is shown [Gug00]. The frequency shift is coupled to the force gradient (equation (3.3) on page 23).

# 3.2 Conductive Scanning Force Microscopy (C-SFM)

In contact mode, the tip is in permanent mechanical contact with the sample surface. On sufficiently conductive samples, an electrical circuit can be established between a conductive tip and the sample. By connecting the SFM tip to a current amplifier and setting the sample on a bias voltage U_S relative to the tip, the electrical current I_{tip} can be detected. Thus, variations in the local conductance $G = I_{tip}/U_S$ of the sample can be studied by scanning the sample at a constant bias voltage. This operation mode is called *conductive scanning force microscopy* (C-SFM, [Fum08, Ber09]).

The advantage of C-SFM is that it uses two independent means to detect surface topography and electrical current. In scanning tunneling microscopy, for example, the topographic information is obtained by adjusting the tip-sample distance to keep a constant tunneling current. Thus, insulating domains on composite samples lead to a tip crash, as the tunneling current breaks down on top of these structures. Even on homogeneously conductive samples smaller variations in the tip-sample contact (e.g. by surface contaminations or impurities) are reflected in a topographic signal. This cross talk is hard to separate from real topographic features.

For establishing an electrical connection, both the sample and the tip have to be electrically connected to the current amplifier. On the sample side, conductive substrates, such as metal coated silicon wafers or, for optically transparent substrates, metal oxide coatings on glass, such as indium tin oxide (ITO) or fluorine tin oxide (FTO), are used. On the tip side, conventional SFM probes are often made from doped silicon, where the doping prevents electrostatic charging (for example Olympus OMCL-AC240TS: N-Type silicon with $4 - 6\,\Omega$cm). However this conductivity is not sufficient to collect measurable currents from the nanometer sized tip. Thus, metal coated tips are commonly used for C-SFM. Gold coated tips have a good stability against oxidation, however the mechanical wear resistance is poor. Owing to its high melting point, hardness and corrosion resistance platinum-iridium is often used as a coating material for SFM tips. Another very wear resistive alternative is a conductive diamond coating. However, next to being expensive, such tips usually have tip radii of curvature in the order of some hundred nanometers, decreasing the lateral resolution.

SFM with simultaneous current measurement was first reported in 1993 for the detection of spatially resolved tunneling currents on SiO_2 gate oxide films [Mur93]. It has become a standard technique for the characterization of semiconductor devices [Ben09]. Additional to the current mapping at a fixed sample bias voltage, local current-voltage characteristics can be recorded with a resting tip and the charge injection mechanism can be determined. This kind of analysis can provide additional information about the material under investigation.

Figure 3.3: Potential distribution at a metal-vacuum interface in the presence of an electric field E_x. At sufficiently high electric fields quantum mechanic tunneling can take place (horizontal arrow).
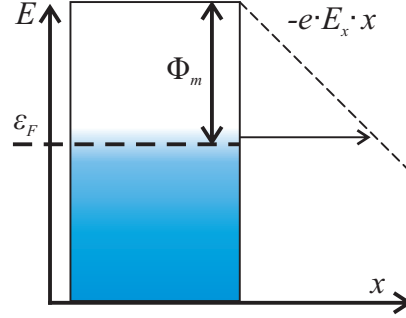
For the discussion of C-SFM experiments, it is useful to understand the physics of charge injection. Therefore, I will introduce the most important models for the description of current-voltage characteristics.

3.2.1 Charge Injection

In an electrical circuit the current usually passes several interfaces between different materials. The charge conduction over interfaces is usually described by an *injection law* that describes the injected current density j as a function of the applied voltage U. In order to simplify the description we use a geometry with parallel electrodes separated by a distance d. The injecting electrode is set to a potential U, yielding an electric field perpendicular to the electrode of $E_x = U/d$. The charge is injected into the medium and is collected by the second grounded electrode, that does not further affect the charge transport properties. We furthermore assume unipolar charge transport, i.e. either holes or electrons are injected.

There are two main mechanisms that can limit the injection current into a medium: (i) an energetic barrier that the charges have to pass, e.g. by tunneling or by thermal excitation (*injection limited*) and (ii) the electrostatic interaction between the charge carriers in the medium, called *space charge limited* conduction.

3.2.1.1 Injection Limited Conduction

In order to remove an electron from a metal surface in vacuum, an energy barrier of Φ (the work function) has to be overcome. Thus, even when a moderate electric field is present, no charge carriers can escape the solid. However, at sufficiently high voltages U, charge carriers start to escape from the solid by quantum mechanic tunneling. This phenomenon is called field emission and it exhibits a characteristic exponential increase of the current density as a function of the applied electric field. The tunneling mechanism can be explained by a tilt of vacuum level due to the presence of the electric field (see figure 3.3). The injected current can be derived by

using the WKB approximation (see [Ham88] page 174 for the complete derivation), yielding

$$j_x = \frac{e^3}{16\hbar\pi^2} \frac{E_x^2}{\Phi_m} exp\left\{-\frac{4\sqrt{2m}\,\Phi_m^{3/2}}{3\,\hbar\,e\,E_x}\right\}$$

$$= K_1 \frac{E_x^2}{\Phi_m} exp\left\{-K_2\frac{\Phi_m^{3/2}}{E_x}\right\} \tag{3.8}$$

(K_1 and K_2 summarize the constants). In the case of injection into a crystalline solid, the work function Φ_m has to be replaced by the energy barrier of the junction for the specific type of charge carriers and the mass m by the effective mass m^*. This injection mechanism is called *Fowler-Nordheim tunneling*. By plotting current voltage characteristics in a Fowler-Nordheim plot with $log(j_x/E_x^2)$ versus $1/E_x$, the injection barrier of the tunneling contact can be derived from the slope of the plot.

Even in the absence of a strong electric field, thermally excited charge carriers can also overcome the work function and escape the solid (thermionic emission). The current density of thermally emitted electrons from a metal into vacuum is given by the Richardson-Schottky equation [Ham88]:

$$j_x = -\frac{emk_B^2T^2}{2\pi\hbar^3}exp\left\{-\frac{\Phi_m - (e^3/4\pi\epsilon\epsilon_0)^{1/2}\,E_x^{1/2}}{k_BT}\right\}$$

$$= A\,T^2\,exp\left\{-\frac{\Phi_m}{k_BT}\right\}\,exp\left\{\frac{b\,E_x^{1/2}}{k_BT}\right\} \tag{3.9}$$

($k_B = 8.6 \cdot 10^{-5}\,\text{eVK}^{-1}$ is the Boltzmann constant). The factor A is the Richardson constant and b summarizes the constants in the exponent. In the case of injection into a solid, the work function Φ_m, unit charge e and mass m have to be replaced by the barrier height Φ_{bi}, the carrier type and the effective mass m^*, respectively. Again, by choosing an appropriate way of plotting current - voltage characteristics, a straight line can be obtained. In this case, Richardson-Schottky plots are used, where $log(j_x)$ is plotted versus $E_x^{1/2}$. From extrapolating the lines, the zero field current j_0 and by additional variation of the temperature, the barrier height can be extracted.

For inorganic semiconductors with band-type conduction behavior and high charge carrier mobilities, the injection from a metal SFM-tip can mostly be explained either a tunneling or a thermionic injection law [Mur93, Olb98]. Although the high degree of disorder and the hopping type charge conduction in organic materials makes the quantitative analysis difficult [Bar99, Sco03], those mechanisms have been used to describe the charge carrier injection into macroscopic organic semiconductor devices qualitatively [Li06, Bur08].

3.2.1.2 Space Charge Limited Conduction

An electrode that shows no blocking behavior is called an *ohmic contact*. In this idealized picture, an infinite number of charge carriers can be injected to the medium already at very low applied voltages. The charge conduction is in this case limited by the transport properties of the medium. Examples are purely metallic contacts, heterojunctions with low built-in potential and photo injecting contacts, where a large number of charge carriers is created by photo absorption.

In the case of an ohmic contact and a medium with a low intrinsic charge carrier density, the injection law can be described in terms of a space charge limited current [Mot50]. Examples for such a situation are the field emission in a vacuum tube at high electric fields or the charge injection into an insulator or an intrinsic semiconductor at low temperatures.

The main assumption is that the electrode emits such a high number of charge carriers that at the electrode surface the electric field is completely shielded (Mott Gurney approximation):

$$E_x(x = 0) = 0 \qquad (3.10)$$

In this case, the charge injection is controlled by the electrostatic repulsion of the injected charge carriers. Therefore, the Poisson equation is required

$$\epsilon_0 \epsilon \frac{\partial^2}{\partial x^2} U(x) = \frac{dE(x)}{dx} = -en(x) \qquad (3.11)$$

(ϵ_0: vacuum dielectric constant, ϵ: relative dielectric constant of the medium, e: elemental charge, n: charge carrier density) in combination with the continuity equation (diffusive currents caused by concentration gradients are neglected):

$$j_x(x) = e\, n(x)\, v_x(x) \qquad (3.12)$$

(j_x: current density, v: position dependent charge carrier velocity). Here, the different transport mechanisms in the vacuum and in a solid come to play. In vacuum, charge carriers are continuously accelerated, yielding $v_x(x) = (2e(U - U(x))/m)^{1/2}$ (m: mass of the charge carrier), whereas in a solid a Drude-like drift motion with $v_x(x) = \hat{v}_x = \mu E_x$ can be assumed (equation (2.1) on page 7). In the vacuum case, we obtain

$$j_x(U) = \frac{4}{9}\epsilon_0 \left(\frac{2e}{m}\right)^{1/2} \frac{U^{2/3}}{d^2}. \qquad (3.13)$$

This injection law is called *Child-Langmuir* law. In the case of a solid medium (dielectric constant $\epsilon > 1$) the electrostatic repulsion of the charge carriers is reduced.

We obtain

$$j_x(U) = \frac{9}{8}\mu\epsilon_0\epsilon\frac{U^2}{d^3}. \tag{3.14}$$

Equation (3.14) is often referred to as the *Mott Gurney* law. The complete derivation of both laws can be found in [Ham88].

In the case of a space charge limited injection it is useful to plot the current-voltage data in a double logartihmic plot, where it should form a straight line. By fitting a power function of the form ax^b to the graph, the exact exponent (1.5 in the vacuum case, 2 in the insulator case) and from the prefactor a the charge carrier mobility of the material can be calculated.

This injection mechanism is commonly used to describe the charge injection from a SFM tip into organic electronic samples [Lin02, Dou06, Dan08b, Rei08].

3.2.2 Applications of C-SFM on Organic Electronics

In addition to the field of inorganic semiconductor devices, C-SFM has become a standard technique for the investigation of organic electronic structures, as well [Pin09a]. One of the first organic structures that was investigated by C-SFM was an individual carbon nano-tube attached to a substrate electrode [Dai96]. From the position dependent resistance, the authors calculated the conductivity of single nanotubes. The field of C-SFM on organic electronic structures was pioneered by the Frisbie group. In 1998 they investigated the charge transport in thin doped oligomer films of sexithiophene by local current - voltage experiments [Loi98] and were able to estimate the resistance of the grain boundaries in sexithiophene crystals [Kel99].

In the following years, several groups started to report C-SFM experiments on the hole conducting polymer commposite system of PEDOT:PSS [Kem04, IZ04], electroluminescent polymers [Lin02] and photoactive layers for organic solar cells [Ale06, Dou06, Ale08]. Here, the multilayer device structure makes the investigation of cross cuts prepared from working devices particularly interesting. The group of Nguyen thus started to investigate focused ion beam prepared cross cuts of P3HT:PCBM [Dan08b] and PCPDTBT:PCBM blends [Dan09]. However, their focus was on the internal structure of the active layer. In a recent publication, Hamadani and co-workers reported a C-SFM investigation on a P3HT:PCBM solar cell cut at a low angle by means of a microtome [Ham10]. On the surface of the blend, they found a homogeneous layer that was enriched with P3HT. As this layer acts as an electron blocking layer, it was made responsible for a decreased device performance. Furthermore, adhesion problems between adjacent layers in the device were reported.

In combination with sample illumination, photoactive blends can generate sufficiently high photocurrent densities for the detection with C-SFM. In 2006 Douhéret and co-workers reported an offset of $0.65\,\text{pA}$ in the recorded tip sample current when they illuminated the sample with $75\,\text{W}$ tungsten lamp. The systematic study of spacially resolved photocurrents was fostered by the Ginger group [Cof07, Pin09b, Bul09]. They used a laser light source and a sample cell that was constantly flushed with nitrogen to minimize photodegradation.

3.3 Electrostatic Force Microscopy

In section 3.1.2 it was shown that the relevant forces for scanning force microscopy can be separated by their specific interaction length scales, electrostatic forces being the most long ranged forces. In order to measure electrostatic fields on a surface without any disturbance by capillary and van der Waals forces, the tip has to be lifted high enough that these forces do not play a role any more. This principle is used in the *lift mode.* In a first step, a topographic contour line is recorded in intermittent contact mode. In a second step, the mechanical excitation is switched off and the tip follows the same contour line shifted in z-direction by a defined lift height, typically $10 - 100\,\text{nm}$ above the sample. In the presence of an electrostatic field an attractive or repulsive force is exerted on the tip. This force can be detected either by the static deflection or - in a dynamic mode - by its influence on the resonance frequency of the cantilever (electrostatic force microscopy, EFM [Mar88]). The latter method has turned out to give a much better sensitivity, as the oscillation phase indicates even small changes in the resonance frequency.

The main drawback of this so called *electrostatic field microscopy* (EFM) is that it can only provide qualitative information about charged structures on the surface. With an additional feedback mechanism, EFM can be extended to provide quantitative information about the local contact potential difference between tip and sample (i.e. the local work function). The so called Kelvin probe force microscope (KPFM) uses the principle of the Kelvin method that will be introduced in the following section.

3.3.1 The Kelvin Method

If two electrically connected solids are separated by a small distance d, fermi level alignment leads to a surface charging (see also section 2.2.1 on page 14). The electrostatic interaction of the surface charges can be exploited to determine the contact potential difference. The Kelvin method uses a plate-capacitor geometry with one plate being the solid under investigation and the other plate consisting
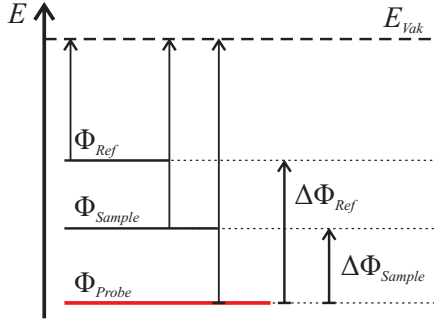
Figure 3.4: Energy diagram of a Kelvin Probe experiment.

of a material with a known work function Φ_{ref} [Kel98]. By periodically vibrating the probe plate by an amplitude z_0 in the z-direction perpendicular to the sample surface, the capacity of the system $C = \epsilon_0 A/d$ (A: surface area of the plates) is modulated with the same frequency ω. Thus, the current through the electrical connection for small vibration amplitudes z_0 is given by

$$I(t) = (U_{CPD} - U_{ext}) \frac{\partial C}{\partial z} \, \omega \, z_0 \, sin(\omega t)$$

$$= (U_{CPD} - U_{ext}) \frac{\epsilon_0 A \omega z_0}{z^2} \, sin(\omega t). \tag{3.15}$$

U_{ext} is an externally applied bias voltage and U_{CPD} is the contact potential difference between probe and sample (see figure 2.5 on page 14). When the external voltage equals the contact potential difference, no current can be measured. Together with the reference work function of the probe plate, the unknown work function of the sample can be derived. As reference electrodes, gold ($\Phi_{Au} = (5.3)\,\text{eV}$ [Boh97]) and highly ordered pyrolytic graphite (HOPG, $\Phi_{HOPG} = (4.475 \pm 0{,}005)\,\text{eV}$ [Han01]) surfaces have been used. The latter has proved to give stable and reproducible results for measurements in ambient air [Han01].

The energy diagram of a work function measurement with the Kelvin method is shown in figure 3.4. In a first step, the probe work function Φ_{probe} is obtained by measuring the contact potential difference $\Delta\Phi_{ref}$ to a reference sample. In a second measurement the sample of unknown work function is investigated. The contact potential difference $\Delta\Phi_{sample}$ yields the sample work function by:

$$\Phi_{sample} = \Phi_{ref} + (\Delta\Phi_{ref} - \Delta\Phi_{Sample}) \tag{3.16}$$

3.3.2 Kelvin Probe Force Microscopy (KPFM)

The idea of the Kelvin method can be applied to a scanning force microscope with the SFM tip as the reference electrode. However, the capacity of tip - sample system is much too low to generate a significant electrical current. Using equation (3.15) and

a typical SFM setup (tip radius of curvature: 10 nm, cantilever resonance frequency: 300 kHz, vibration amplitude 50 nm), a contact potential difference of 1 V and a tip scan height of 100 nm, we obtain for the alternating current an amplitude of 4 fA. This is very hard to measure precisely at this frequency range. Nevertheless, the scanning force microscope is a very sensitive tool for measuring forces.

Given that both tip and sample are sufficiently electrically conductive (e.g. by using highly doped or metal coated tips), the potential difference between tip and sample can be influenced by applying an external bias voltage U_{DC} to the tip. Furthermore, the cantilever's mechanics can be exploited by using an alternating voltage $V(t) = U_{AC} sin(\omega_0 t)$ at the cantilever's resonance frequency ω_0. Thus, equation (3.6) (page 24) becomes

$$F = \frac{1}{2} \frac{\partial C}{\partial z} \left(U_{CPD} - U_{DC} + U_{AC} \, sin(\omega_0 t) \right)^2. \tag{3.17}$$

Using $sin^2(x) = 1/2 \left(1 - cos(2x) \right)$ and separating into the frequency components F_{DC}, F_ω and $F_{2\omega}$ leads to

$$F_{DC} = \frac{1}{2} \frac{\partial C}{\partial z} \left((U_{CPD} - U_{DC})^2 + \frac{U_{AC}}{2} \right) \tag{3.18}$$

$$F_\omega = \frac{\partial C}{\partial z} \left(U_{DC} - U_{CPD} \right) U_{AC} \, sin(\omega_0 t) \tag{3.19}$$

$$F_{2\omega} = \frac{1}{4} \frac{\partial C}{\partial z} U_{AC}^2 \, cos(2 \, \omega_0 t). \tag{3.20}$$

The 2ω signal is influenced by the capacity gradient. It is connected to changes in dielectric properties of the material under the tip. The force component F_ω can be compensated by bringing $(U_{DC} - U_{CPD})$ to zero. In this case U_{DC} equals the contact potential difference U_{CPD}). If U_{DC} is controlled by a feedback loop during scanning, variations in U_{CPD} can be mapped on the surface [Ber09].

This form of Kelvin probe force microscopy was first reported in 1991 by Nonnenmacher, O'Boyle and Wickramashinge [Non91]. Several modifications and improvements have been proposed so far. Jacobs and co-workers have studied the influence of the tip material and the drive and feedback parameters, in particular the importance of the drive phase shift [Jac99]. They found from numerical simulations that the high surface area of the cantilever dominates the electrostatic interaction when the tip apex size becomes too small. In addition, they reported that it would be beneficial to use long and slender tip cones and a cantilever with minimal surface area.

3.3.3 Single Pass vs. Dual Pass

Another issue is the prolonged acquisition time of the lift mode, as every scan line has to be recorded twice (dual pass). Therefore, KPFM techniques have been proposed, where the potential signal is recorded simultaneously with intermittent contact imaging (single pass). This also solves the problem of electrostatic crosstalk to the topography image. One strategy is to use an excitation frequency below the resonance frequency and detect the response by means of a lock-in amplifier. Being off resonance, however, the detected signals are weak and thus the sensitivity is limited. Alternatively, frequency modulation techniques that monitor the frequency spectrum of the cantilever are used [Zer05].

A principal problem of single pass operation, especially under ambient conditions, is that the tip response during one oscillation cycle of the intermittent contact operation is the integrated response over several force regimes. At the lowest point of the oscillation, the tip is in contact with the surface and repulsive chemical forces act on the cantilever. At sufficiently high voltage differences, an exchange of charge carriers is also possible [Fre00]. At ambient conditions, the adsorbed water layer and thus capillary forces can influence the cantilever motion. For stable operation of single scan KPFM in air, a true non-contact operation would be necessary which is hard to achieve under ambient conditions [Zie07]. Finally, the different regimes of van der Waals forces (retarded and unretarded) are passed in the remaining part of the oscillation cycle. All these different forces make the interpretation of single pass KPFM signals difficult.
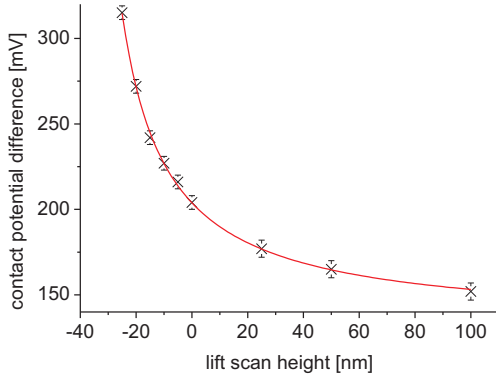
Figure 3.5: Dependence of the measured contact potential difference to the lift height. The experiments were performed on freshly cleaved HOPG under ambient conditions. The lift height is with respect to the equilibrium cantilever position during the intermittent contact measurement of the topography.

However, even the interpretation of dual pass experiments is not straight forward. The adsorbed water layer can influence the electric field between tip and sample and decrease the measured surface potential contrast [Sug02]. Thus, measuring in low humidity environments and the use of hydrophobic surfaces is beneficial. Furthermore, the absolute value of the measured contact potential difference has a certain dependence on the lift height (see figure 3.5). Liscio and co-workers found a similar

distance dependence. Additionally, they studied the influence of the other operation parameters on the recorded signals: drive amplitude and the humidity. They explained the variations by deviations from the simple plate capacitor model and a non-zero vibration amplitude during the lift scan [Lis08]. Although high drive amplitudes and low lift heights can improve the resolution, the distance dependence effects have to be taken into account when absolute work function values are measured.

3.3.4 Applications of KPFM to Organic Electronics

KPFM is an interesting tool for the study of soft matter composite samples, in particular for organic electronic systems [Pal06, Pin09a, Lis10]. Mapping the potential on bottom gate organic field effect transistors, for example, can give insights to injection barriers at the electrodes and defects in the gate channel [Bur02, Pun03, Smi07]. A big advantage of KPFM is that the topography signal is obtained in an intermittent contact mode. Thus, the mechanical interaction of tip and sample is low.

Important contributions to the understanding of the working mechanism of organic solar cells have been obtained by KPFM, especially in combination with sample illumination. Chiesa et al. investigated the surface potential of MDMO-PPV:PCBM blends [Chi05]. With increasing illumination intensity (473 nm diode laser) they found a logarithmically increasing surface potential on the top side of the blend. Furthermore, they found correlations between the morphology and the light induced potential changes, which they could associate to regions with more efficient charge separation. Hoppe and co-workers investigated MDMO-PPV:PCBM blends prepared from chlorobenzene and tolluene [Hop05]. With Kelvin probe microscopy they demonstrated that the finer phase separation in the chlorobenzene cast films is beneficial for the charge separation process. In a number of other publications similar correlations between surface potential and morphology were reported in organic [Pal07a, Pal07b] and organic/inorganic (hybrid) systems [Zen09, Liu09]. Recently, Liu and co-workers measured photoinduced charging in single carbon nanotubes embedded in a P3HT film illuminated with a halogen lamp [Liu10].

4 Electrical SPM on Hybrid Solar Cell Structures
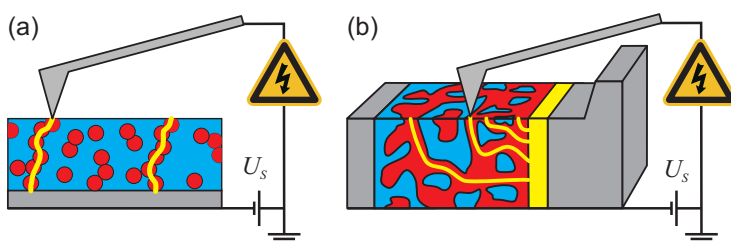
With scanning probe microscopy, the working principles of functional layers in optoelectronic devices can be tested and visualized. There are two types of questions that can be answered:

(a) What are the properties on top of a film?

(b) What are the properties at specific interlayers in a multi-layer device?

For the first type of question, SPM is performed on top of the device. Surface properties, such as variations in the work function (with KPFM), or the transport properties through the film (with C-SFM) can be studied. The latter can be highly important for blend systems, where one component has to form electrical interconnections through the blend film (percolation). However, the surface often yields only part of the information necessary for understanding processes originating from deeper lying layers. Here, the analysis of cross cuts through devices can be particularly interesting, as the specific properties of all layers can be studied and compared.

In this chapter, different structures for hybrid solar cells will be investigated. Having introduced the working principle of a blocking layer, I will present experiments on surface and transport properties of a novel integrated blocking layer structure. Finally, I will present my experiments on a focused ion beam polished cross cut of a hybrid solar cell device with a conventional blocking layer. The cell was prepared by a recently developed one-pot synthesis approach.

4.1 Blocking Layer

In both organic and hybrid solar cells an unipolar injection at the electrodes is of utmost importance. Owing to the slow hopping transport, bipolar injection at one of the electrodes would strongly increase recombination losses (figure 4.1 (a)). Thus, additional layers of hole-conducting materials such as PEDOT:PSS or electron conducting materials such as TiO_2 are added between the active layer and the respective electrodes (figure 4.1 (b)).

In the case of TiO_2, the high ionization potential of $7.4\,eV$ results in an energetic barrier for holes, whereas the electron affinity of $4.2\,eV$ is well matched to the energy of electrons generated in the most common active layers of polymer- or hybrid dye sensitized solar cells. Although these layers generate additional interfaces, the overall performance of the device is increased [Pen04].
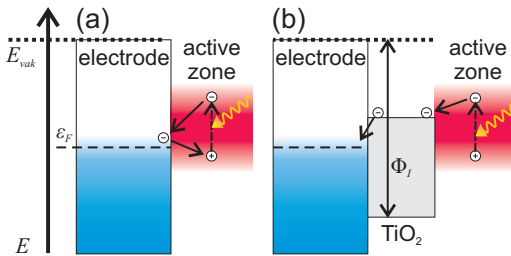
Figure 4.1: Without blocking layer, charge recombination at the electrode is possible (a). Materials with high ionization potential Φ_I, such as TiO_2, can effectively block the holes generated in the active layer (b).

4.2 SPM Studies on an Integrated Blocking Layer

In most standard hybrid solar cells, a solid, some hundred nanometer thick layer of TiO_2 is deposited on the electrode (e.g. fluorine-doped tin oxide, FTO) [Pen04], followed by nanoporous TiO_2 as the n-type material for the active layer. The blocking layer in this form has two drawbacks: first, an additional preparation step is necessary and second, there is one more interface between active layer and electrode that might give rise to losses due to injection barriers. The direct deposition of porous TiO_2 on the electrode, however, would enhance recombination losses (figure 4.2 (a)).

Recently, a combined concept for a nanoporous crystalline TiO_2 network with an integrated blocking layer has been proposed [Che06, Mem09]. The blocking layer consists of a nanocomposite of conducting TiO_2 nanoparticles embedded in an electrically insulating polymer derived ceramic matrix. Whereas the TiO_2 is supposed to have a good and homogeneous electrical contact to the substrate, the voids in between should be insulating owing to the ceramics and thus prevent recombination (figure 4.2 (b)).

Figure 4.2: In a bulk heterojunction without blocking layer, recombination would decrease the device performance. With an insulating layer around the TiO$_2$ close to the electrode, recombination is reduced.
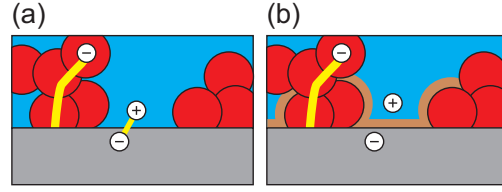

The proposed working mechanism was tested by means of electrical SPM. The effects of different TiO$_2$ concentrations on the morphology and the electric properties were studied with C-SFM, whereas the effects of the preparation procedure were investigated by KPFM. The project is a collaboration with Mine Memesa (AK Gutmann, MPI-P Mainz), who did the synthesis and the sample preparation.

4.2.1 Experimental

For the preparation of the nanocomposite, a structure defining triblock copolymer poly(ethyleneglycol)methylethermethacrylate - block - poly(dimethylsiloxane) - block - poly(ethyleneglycol)methylethermethacrylate ((PEO)MA-PDMS-MA(PEO)) was used (see figure 4.3 (a)) [Mem09]. It fulfills two tasks: first, it defines a granular morphology via self organization in a sol-gel process together with the TiO$_2$ precursor material titanium tetraisopropoxide (TTIP). Second, it contains a PDMS block that can be transformed into an electrically insulating silicon carboxide by annealing it at sufficiently high temperatures.

Samples with 2% and 5% TTIP content in the stock solution (called for simplicity 2-TTIP and 5-TTIP) and a reference sample with pure polymer were spin-cast on a 50 nm thick sputtered platinum electrode on a silicon wafer. For the KPFM experiments, the requirements for the surface conductance are lower. Thus, a second set of samples was prepared in the same way at a TTIP content of 2% directly on a highly doped silicon substrate (SiMat, CZ, N/Sb, resistivity $0.01 - 0.02 \, \Omega$cm). In order to expose the top parts of the TiO$_2$, all samples were treated in argon plasma at a power of 300 W for 10 min. Afterwards, samples were annealed at 450 °C in nitrogen atmosphere. During the annealing step, the amorphous aggregates of TiO$_2$ transform to anatase TiO$_2$, whereas the PDMS part of the copolymer ceramizes into an insulating silicon oxycarbide matrix (figure 4.3). The film thickness was measured with a surface profiler (Tencor P-10). The 5-TTIP sample was found to be approximately three times thicker ((102 ± 7) nm) than the film of the 2-TTIP sample ((30 ± 6) nm).

The surface potential was measured by KPFM (Veeco Dimension 3100; Si Cantilevers from Olympus (OMCL-AC240TS), nominal resonance frequency of 70 kHz) in the dual pass mode at a low lift height (typically 10 to 20 nm below the average tip
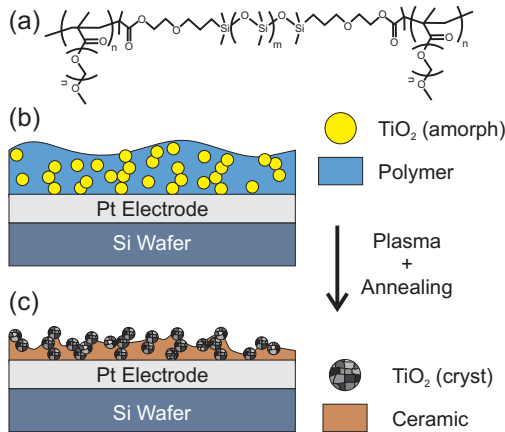
Figure 4.3: (a) (PEO)MA-PDMS-MA(PEO) triblock copolymer used for the sample preparation. (b) The TiO_2 - polymer composite is spincoated on a conductive substrate. (c) Plasma tratment exposes the top parts of the TiO_2 particles and annealing crystallizes the TiO_2 and transforms the remaining polymer into a ceramic matrix.

height during non contact imaging). It was chosen to be in a good balance between highest lateral resolution and errors due to the height dependence of the contact potential (see figure 3.5 on page 34). For C-SFM (Veeco MultiMode, TUNA current amplifier $1\,pAV^{-1}$), Pt/Ir coated SPM tips (nominal resonance frequency of $70\,kHz$, tip radii of curvature $10 - 20\,nm$, Nanosensors PPP-EFM) were used.

4.2.2 Kelvin Probe Force Microscopy

With KPFM, the samples were investigated to find possible material changes in terms of mechanical properties and work function caused by the preparation procedure. For these measurements we compared pristine with plasma treated and annealed 2-TTIP samples.

From the topographical images we found that both the structure of pristine and the annealed 2-TTIP sample showed a granular structure with a typical grain diameter of $20\,nm$ and a root-mean-square roughness of $0.5\,nm$ (figure 4.4 (a) and (d)). The absence of a phase contrast in figure 4.4 (b) and (e) indicates that the particles were closely packed and that the amount of polymer in between the particles is not sufficient to cause a measurable material contrast in the pristine sample.

In the surface potential maps in figure 4.4 (c) and (f) a granular structure with the same dimensions compared to the structures in the topographic images is observed. The observed contrast can be attributed to the exposed top parts of the TiO_2 particles (darker spots) embedded in a material of lower work function (brighter network).

The calculation of the absolute work function was done according to equation (3.16) (page 32) with a freshly cleaved HOPG sample directly before the experiment. The contact potential difference of the silicon tip and the HOPG surface was found to be $(-192 \pm 13)\,mV$. Thus, the work function of the tip is $(4.3 \pm 0.1)\,eV$. The sample work functions reveal a clear shift from $(3.7 \pm 0.1)\,eV$ to $(4.5 \pm 0.1)\,eV$ from the
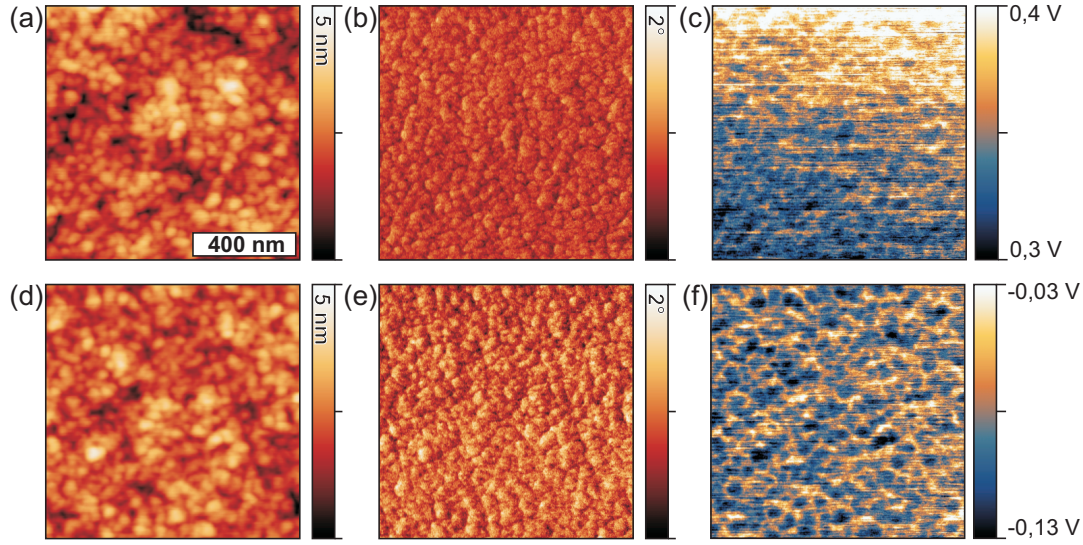
Figure 4.4: KPFM of the pristine ((a) to (c)) and the plasma treated/annealed ((d) to (f)) sample. No changes can be observed in the topography ((a), (d)) and the phase image ((b), (e)). However, both the contrast and the absolute value of the surface potential are changed ((c), (f)).

pristine to the plasma treated and annealed sample surface (figure 4.4 (c) and (f)). In all pristine samples, we observed that the work function changed during scanning, i.e. from top to bottom in figure 4.4 (c). This decrease in work function can be attributed to the gradual contamination of the SFM-tip by the soft (PEO)MA-PDMS-MA(PEO) during scanning [Jac99]. Such a pronounced decrease in surface potential was not observed on the plasma treated and annealed samples, which additionally indicated the conversion of the soft (PEO)MA-PDMS-MA(PEO) - TTIP compound at the sample surface into a hard inorganic nanocomposite.

4.2.3 Conductive Scanning Force Microscopy

The C-SFM topography of both the 2-TTIP and the 5-TTIP sample showed an almost identical granular structure compared to the intermittent contact KPFM results (figure 4.5 (a) and (d)). This is important as it proves that the sample is hard enough for a non-destructive contact mode C-SFM study. The similar structure of the 2-TTIP and the 5-TTIP sample shows that the TiO_2 precursor content in the stock solution does not have an influence on the surface structure, in particular on the average diameter and the density of TiO_2 particles.

The current maps show that on both samples almost every grain on the surface was connected with a localized current (figure 4.5 (b) and (e)). The samples carried an
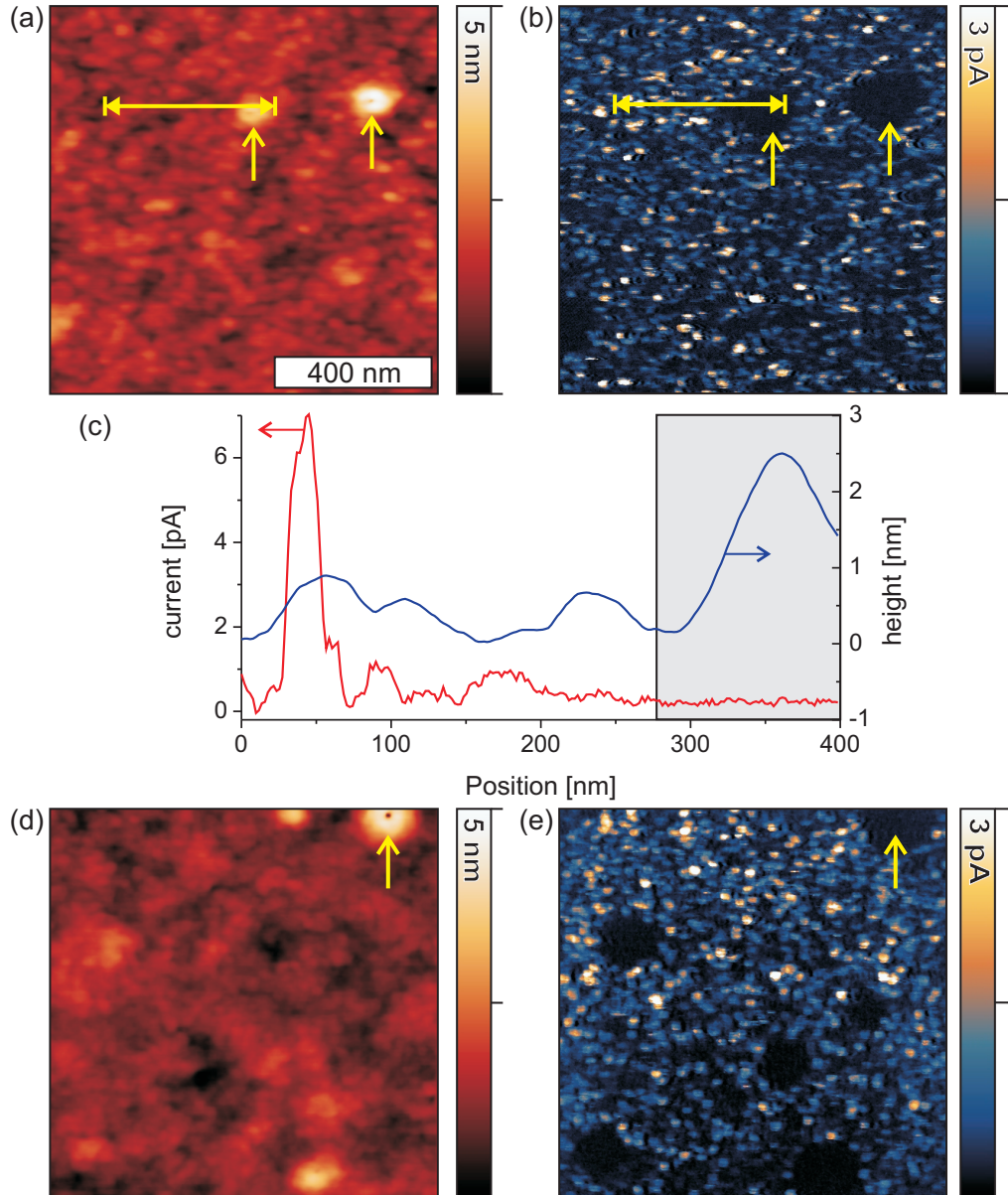
Figure 4.5: C-SFM results of the nanoporous TiO_2 samples: (a) and (b) on the 2-TTIP sample at a sample bias of 2.2 V and (d) and (e) on the 5-TTIP sample recorded at a sample bias of 2.4 V. (c) A section view of a scan line recorded in (a) and (b) demonstrates the correlation of current and topography; the gray shaded area shows one of the electrically insulating defect structures (yellow arrows).

average current of 470 fA (2-TTIP, sample bias 2.2 V) and 450 fA (5-TTIP, sample bias 2.4 V). In the section view of figure 4.5 (c) (left hand side) the correlation between topography and current is demonstrated. The two elevations give rise to a current of 6 pA and 1 pA, respectively, whereas the surrounding parts remain insulating. The correlation of grains and currents proves that the increased conductance was caused by the TiO_2 particles which formed an interconnection to the bottom electrode, whereas the gaps between the particles were electrically insulating.

Owing to the more than three times thicker film of the 5-TTIP sample, there have to be more TiO_2 particles in an average percolation path. The interconnection between adjacent TiO_2 particles, however, should be similar in both films. Thus, thicker films should have a lower conductance owing to the increase in the average percolation length. The average conductance on both samples, however, is similar. Therefore the determined currents are not limited by the resistivity of the TiO_2 network. Instead, injection barriers at the platinum-TiO_2 and the TiO_2-tip interface are more plausible to be the limiting factor for the currents.

Furthermore, larger insulating areas, $50 - 100$ nm in width, were observed on both samples. Most of these areas could be associated with elevations in the topography, $2 - 6$ nm in height (e.g. the two adjacent spots in figure 4.5, yellow arrows and gray shaded part in (c)). Scanning larger areas showed that these insulating spots occurred at a density of $2 - 3$ per μm^2. On the fresh samples, no comparable structures were observed. Thus, the structures are formed during the annealing of the samples. The high temperatures during the annealing leads to thermal stress which might cause deformations in the film. This interpretation is supported by the finding that in the center of larger elevations, small depressions $10 - 15$ nm in diameter and 5 nm in depth occurred (e.g. yellow arrow in figure 4.5 (c)).

Finally, I investigated the sample for possible tip-induced irreversible modifications on the surface. With intermittent contact mode images recorded with the same tip at the same position before and after the C-SFM experiment, no changes in the surface topography were observed (not shown here). However a "zoom out" to a larger scan area in C-SFM mode revealed an increased current in previously scanned areas (figure 4.6). In the outer region the sample was scanned with C-SFM for the first time. Here, the current had an average value of 900 fA (sample bias 3.3 V). In the area that had been scanned once before the measurement (scan size 4 μm, yellow square) this value increased to 1.4 pA. In the 1 μm wide inner square (red), where the sample had been scanned twice before, it was even 1.7 pA. This increase in current of almost a factor of two could be explained by a "directed annealing" that increases the conductance of the current paths and the substrate contacts along the TiO_2 particles when a current flows.
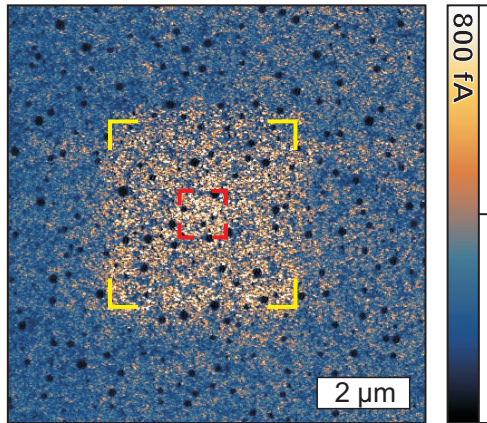
Figure 4.6: "Zoom out" to a larger scan area on the 5-TTIP sample. The previously scanned area of $4\,\mu m$ (yellow square) and $1\,\mu m$ scan size (red square) are clearly visible due to higher currents (sample bias $3.3\,V$).

4.3 Cross Sectional SPM of a Hybrid Solar Cell

Compared to organic solar cells, the fabrication of a bulk heterojunction in a hybrid solar cell is more complex. The inorganic phase (e.g. TiO_2) has to be crystalline in order to become semiconducting. At the same time, a high surface area between the inorganic and the organic semiconductor is required for an efficient charge separation. Thus, the preparation is commonly separated into two subsequent steps. First, the nanostructured inorganic part is prepared on top of a solid blocking layer. Second, a solution of the organic semiconductor is spin- or drop coated on top. Finally, an additional blocking layer and the top electrode are added.

In an alternative approach, the preparation of a hybrid bulk heterojunction in a single step was demonstrated [Lec09]. An amphiphilic block copolymer was synthesized with an additional hole-conducting moiety. The solf organizing properties of the polymer were used to obtain a well-defined TiO_2/conducting polymer structure. Depending on the preparation conditions, different morphologies such as wires, spheres and foam-like structures were obtained.

For the possible application as a bulk heterojunction in a solar cell the formation of percolating morphologies is of highest importance. In this context, scanning electron
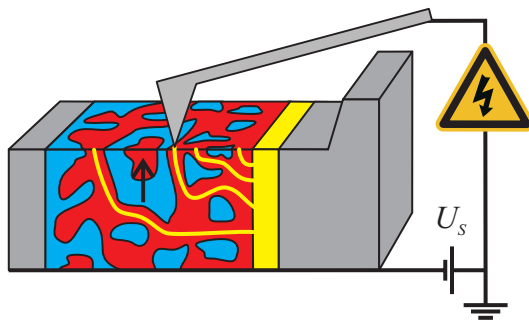
Figure 4.7: Schematic of C-SFM on a cross cut. Unpercolated domains (arrow) can be identified as electrically insulating spots.

Figure 4.8: A simple fracture of a solar cell would be very rough (a). Thus, a small part of the fracture was polished with a focused ion beam. This area was smooth enough to be investigated by C-SFM (b).
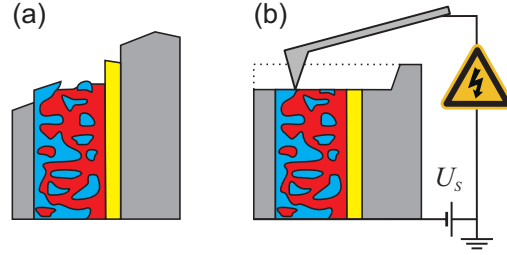
microscopy, e.g. on fractures of the sample, can give first hints towards appropriate morphologies. However, it cannot visualize the electrical contact of parts of the sample with the respective electrodes. Here, conductive scanning force microscopy is the method of choice, as it can map the sample conductance with a resolution in the order of 10 nm. In order to identify possible non-percolating islands inside the film, I prepared a cross cut of such a hybrid solar cell (figure 4.7). The project was a collaboration within the IRTG together with Maria Lechmann (AK Gutmann, MPI-P Mainz), who synthesized the material and prepared the solar cells.

4.3.1 Experimental

For the solar cell preparation, a $50 - 100$ nm thick massive TiO_2 hole-blocking layer was deposited on a fluorine-doped tin oxide (FTO) substrate. The active layer was prepared in a one-pot preparation procedure. Therefore, a poly(ethylene oxide)-b-poly(triphenylamine) (PEO-b-PTPA) block copolymer was combined with a TiO_2 precursor material (etylene glycol modified titanate, EGMT) and a dye (Ruthenium Z907) in a sol-gel process [Lec09]. The material was then drop-casted on top of the blocking layer. The active layer had a thickness of $1 - 2$ µm. Next, an electron blocking layer of PEDOT:PSS was spin-casted. Finally, a top electrode (gold) was evaporated on top. With 200 nm thickness, the gold layer was chosen to be higher than necessary. Thus, the electrode acted additionally as a protection layer against high energy ions in the following focused ion beam polishing step.

For the cross sectional analysis, a fracture of the solar cell was prepared along one of the electrodes. However, such fractures yield very rough surfaces as the fracture does not occur at the exact same position in all parts of a multilayered structure (figure 4.8 (a)). Thus, I used a focused ion beam (FIB, FEI Nova 600, dual beam setup) to polish a 30 µm wide section to obtain a sufficiently smooth area. Several steps with decreasing ion current (ion energy 30 keV) were carried out to minimize the effects of sample heating and ion implantation towards the end of the process. Finally, the section was imaged by scanning electron microscopy (FE-SEM, Zeiss LEO 1530).
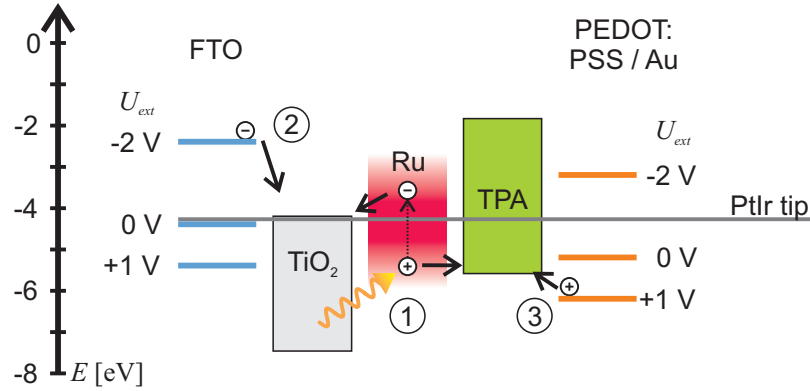
Figure 4.9: Energy diagram for the hybrid solar cell. Upon illumination, excitons are generated by photo-absorption in the Ruthenium dye (Ru). The electrons are transfered to the TiO_2, whereas the holes are transfered to the triphenylamine (TPA) polymer (1). The energies of the electrodes (FTO and PEDOT:PSS/gold) are sketched without bias ($U_{ext} = 0\,V$) and at the bias voltages used in the C-SFM experiments. The work function of a platinum/iridium coated tip (4.2 eV) is indicated as a gray line. On the TiO_2 side, electrons can easily be injected at negative bias voltage (2), whereas on the TPA side, the injection of holes should be favored (3).

Conductive scanning force microscopy (C-SFM) was performed on a MFP3D Standalone, Asylum Research, in dry N_2 atmosphere (see chapter 6 for a detailed description of the setup). A current amplifier (ORCA, Asylum Research) was used together with platinum/iridium coated tips (nominal resonance frequency of 70 kHz, tip radii of curvature $10 - 20$ nm, Nanosensors PPP-EFM). The sample was contacted at the bottom FTO electrode. As the gold electrode is much larger than the contact with the SFM-tip, I assume that the top gold electrode will be on the same potential as the FTO electrode.

4.3.2 Results and Discussion

The proposed energy diagram for the solar cell is shown in figure 4.9. Additionally, the work function of a platinum/iridium coated silicon tip is indicated by a vertical line. It was determined by calibrating the tip by KPFM on an HOPG sample according to section 3.3.1 on page 31. I found a value of (4.2 ± 0.1) eV, which is within the error margin of values reported in the literature [Hop05].

The electron microscopy image of the resulting section is shown in the background of figure 4.10. On the left hand side the active layer containing the nano-composite of TiO_2 (brighter parts) and the PTPA conjugated polymer (dark) can be seen. It

Figure 4.10: In the background a SEM of a focused ion beam polished cross section of a hybrid organic solar cell is shown. The insets show the C-SFM results with identical magnification on a different spot of the section. The upper part was recorded at a sample bias of $-2\,\text{V}$ and the lower part at $+1\,\text{V}$ (absolute current values are displayed).
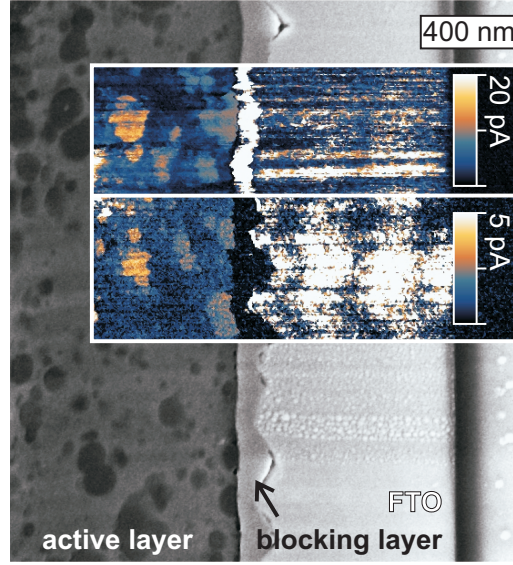
is followed by the massive TiO_2 blocking layer, the FTO electrode and the glass substrate.

The C-SFM current maps for negative (upper inset, sample bias $-2\,\text{V}$) and positive sample bias (lower inset, sample bias $+1\,\text{V}$) are displayed in figure 4.10. For an easier comparison between the two current maps, the current values for the negative sample bias have been inverted. On top of the metallic FTO electrode, a similar conductance was observed for both polarities ($10\,\text{pA}$ at $-2\,\text{V}$ and $6\,\text{pA}$ at $+1\,\text{V}$). The horizontal lines of higher currents can be attributed to the FIB polishing process. They can be observed in all other layers, as well.

On top of the blocking layer structure, a high current of $330\,\text{pA}$ was recorded at negative sample bias. At positive bias, the blocking layer was almost insulating: a current of $200\,\text{fA}$ was recorded, more than a factor of 1000 less. This rectifying behavior can be understood in terms of a Schottky barrier that forms between the metallic FTO and the n-type semiconducting TiO_2 [Sna06] (see also figure 2.5 on page 14).

On the the active layer, a similar behavior would be expected. The TiO_2 should yield a higher current at negative sample bias ((2) in figure 4.9), whereas on top of the TPA polymer higher currents at positive bias would be expected ((3) in figure 4.9). However, I observed the same contrast for both polarities. The TPA polymer rich domains carried $3-10$ times higher currents compared to $1\,\text{pA}$ recorded on the TiO_2 rich domains.

This bipolar transport in the active layer could be caused by gallium ions implanted during the polishing procedure. However, this would only affect a small surface layer of the cut. Furthermore, the one pot preparation procedure might not lead

to completely pure phases. Residual TiO_2 in the TPA polymer rich phase and vice versa might enhance bipolar transport. The higher conductance and unipolar transport observed on the blocking layer compared to the TiO_2 in the active layer is thus most probably caused by the higher purity and crystallinity in the blocking layer. Moreover, the drop-casting might not lead to a perfect mechanical and thus electrical contact between the active layer and the substrate. This generates additional injection barriers that deteriorate the device performance.

Finally, with C-SFM no completely insulating spots could be found on the active layer, neither on the TPA polymer rich nor on the TiO_2 rich domains. This observation proves, that the TPA polymer formed a well percolating network through the TiO_2 network and vice versa. Thus, the here presented morphology is well suited for the application in hybrid solar cells.

4.4 Summary

With the electrical SPM studies, deep insights into the working mechanism of hybrid structures for solar cells were gained and specific problems were identified. By local conductance and Kelvin probe measurements the working principle of a novel nanocomposite material with integrated blocking layer could be visualized. Moreover, defect structures could be identified which might deteriorate the performance of the structure.

The increase of the sample conductance on areas that were scanned several times with C-SFM has demonstrated that tip-induced modifications on the sample surface have to be taken into account. Next to the mechanical interaction, current induced effects can cause irreversible effects, owing to the highly localized nature of the measurement.

With C-SFM on a focused ion beam polished cross cut of a hybrid solar cell structure, the multi-layer system inside the cell could be studied and specific functionalities, such as the hole blocking behavior of a TiO_2 layer, could be visualized. Different preparation conditions in the layers (annealed TiO_2 in the blocking layer, sol-gel derived TiO_2 in the active layer) resulted in qualitatively and quantitatively different charge transport properties. In contrast to unipolar charge transport in the blocking layer, the TiO_2 in the active layer showed bipolar transport at much lower current densities. Moreover, it could be proved that inside the active layer, the hole- and electron conducting parts formed a well percolated network.

5 Scanning Conductive Torsion Mode Microscopy
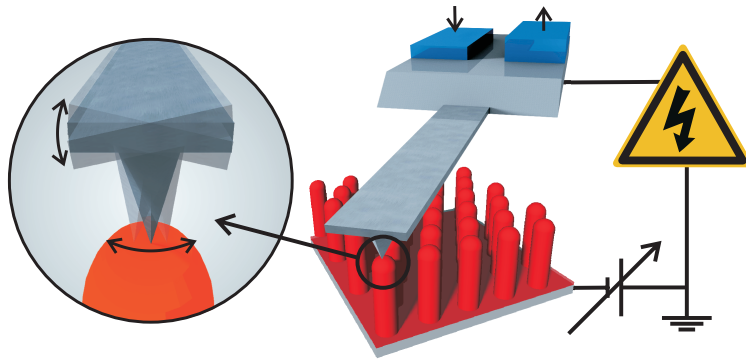
In spite of many publications, the application of C-SFM on soft, fragile and flexible electronic components is challenging. During the operation of the SFM in contact mode, high lateral forces can be exerted on the sample by the scanning tip, leading to modifications in the sample surface [Leu92, Ber07]. Such changes on soft organic electronic materials have been reported in the context of C-SFM studies [Dou07a, Dan08a] (see figure 1.2 on page 4).

In order to avoid lateral forces, advanced SFM techniques have been proposed. Jumping mode scanning force microscopy [Ots03] is a force-volume based method, where on every point of the sample a force-distance curve and, at a defined force, a current-voltage curve is recorded. In point-contact current imaging microscopy [Pab98] the topographic information of an oscillating cantilever is used to bring the tip in contact with the surface, where a current voltage curve is recorded. Both methods reduce the lateral forces on the sample; however, measurement times become very long. Freitag et al. described local conductivity measurements using a quartz needle sensor on carbon nanotubes [Fre00]. However, the individually fabricated probes limit the wide application of this method.

Thus, for soft and fragile organic electronic samples, there is still a need for a more gentle method that minimizes the tip-sample interaction at constant electrical contact with the sample. With scanning conductive torsion mode microscopy, such

a new mode was used for the first time to characterize organic electronic structures in the context of this work.

5.1 Working Principle
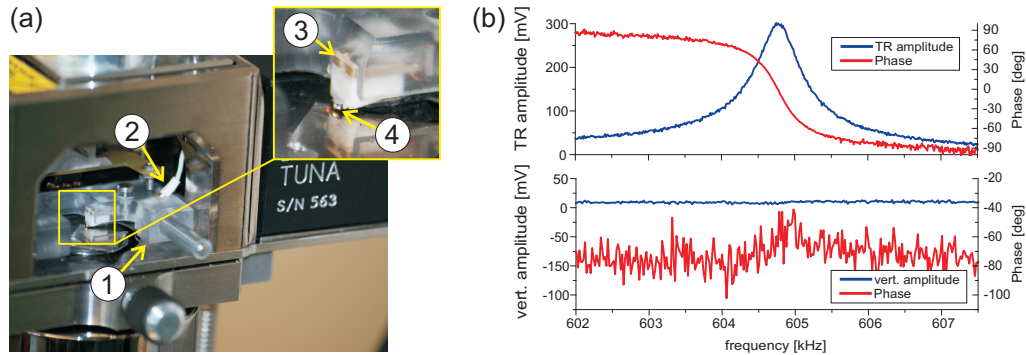
Figure 5.1: SCTMM on a Veeco MultiMode (a). The cantilever holder (1) is electrically connected to the current amplifier (2). Inset: the two piezos (3) under the chip of the cantilever (4) can excite the torsional motion in the cantilever. Torsional amplitude around the resonance frequency ((b), upper graph) and simultaneously recorded vertical signal (lower graph), demonstrating that the torsional motion is not coupled to a vertical motion.

In torsion mode, the base of a rectangular cantilever is vibrated by a pair of piezo-electric actuators that are driven antiperiodically (figure 7 (a) and previous page). Depending on the vibration frequency, a torsional resonance mode can be excited in the cantilever (figure 5.1 (b)). When the tip gets close to the sample surface, the vibration amplitude is reduced. This damping is caused by surface forces and in-plane interactions with the sample [Kaw02, Hua04]. The decrease in amplitude is used as a feedback signal for the tip-sample separation. Thus, the feedback loop is sensitive to vertical obstacles and lateral forces can be minimized.

Before the exact tip-sample interaction was explored, a series of calibrations had been performed to correlate the amplitude that is displayed in the SFM-software in volts with the physical motion amplitude of the SFM tip.

5.1.1 Estimation of the Torsional Amplitude

For the calibration, several steps were necessary. First, the lateral signal of the photo diode had to be correlated with the torsional deflection angle of the cantilever.

It turned out that the amplitude values in the software (given in volts) do not correspond to the values measured at the photo diode (Software version 5.31r1, Nanoscope IIIa controller, Quadrex extender, torsion mode adapter). Finally, the typical dimensions of a PPP-EFM (NanoSensors) tip cone were used to obtain the real amplitude of motion for the tip apex.
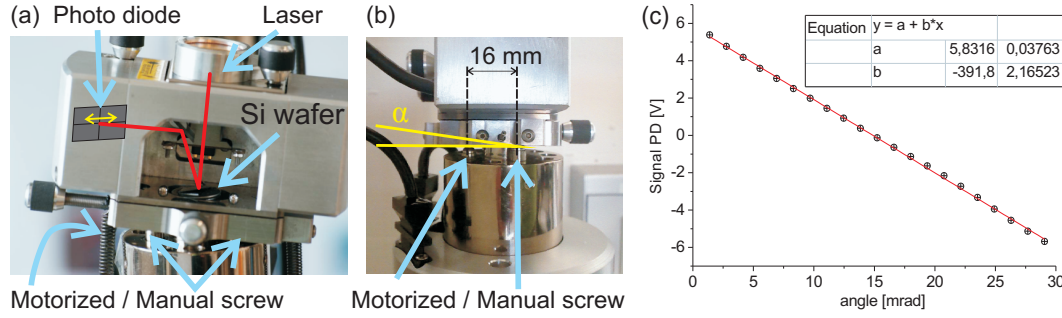
Figure 5.2: Calibration procedure for the torsional motion of the SFM tip. (a) Front view and (b) side view of the scanner with the SFM head on top. The tilt angle α can be controlled by the motorized screw; (c) lateral photodiode signal as a function of the head tilt angle.

For the correlation of the cantilever angle with the lateral photo diode signal, a MultiMode scanner with three independent height adjustment screws was used (serial number 1601 E-z, figure 5.2 (a), (b)). These screws can adjust the tilt angle α of the SFM head on top of the scanner. Two of these screws are manual screws; the third is moved by a step motor that is controlled by the software (e.g. for the sample approach). The pitch of the motorized screw was determined to be $(323 \pm 5)\,\mu m$. On the sample holder of the scanner, a flat piece of silicon was placed. The SFM head without the cantilever holder was tilted with the manual screws until the SFM laser was reflected from the silicon onto the photo diode (figure 5.2 (a)).

The motor control in the SFM software allows to control the SFM head height in steps as low as $26\,nm$ (NanoScope software version 5.31R1). This step size had to be correlated with the true position of the motorized screw. For a full revolution of the step motor, 75 steps at a step size of $1.01\,\mu m$ (software) were necessary. However, the pitch of the screw was measured to be $323\,\mu m$. Thus, the step size of the software has to be corrected by a factor of $323\,\mu m/(75 \cdot 1.01\,\mu m) = 4.26$. The displacement of the motor was then converted into the tilt angle α using the distance of the motorized screw to the manual screws ($16\,mm$, see figure 5.2 (b)).

In a series of 21 steps of $520\,nm$ (software) / $2.21\,\mu m$ (real) / $1.4\,mrad$ (tilt angle) the lateral signal of the photo diode was measured (display on the front of the MultiMode base). The result is displayed in figure 5.2 (c). The response was linear over the

the whole range of the measurement. A sensitivity factor of $(392 \pm 2)\,\mathrm{V\,rad^{-1}}$ or $(2.552 \pm 0.013)\,\mathrm{mrad\,V^{-1}}$ was determined by a least squares fit.

The electrical signals were cross checked with a signal access module (Veeco) and a digital oscilloscope (Tektronix, TDS 1012, coupling: DC $1\,\mathrm{M\Omega}$). The static lateral deflection values displayed on the base of the SFM were found to be identical to the signal going to the controller. The oscillation amplitude A_{softw} that is displayed in the software, e.g. during a cantilever tune, was also identical for the combination of NanoScope V controller and software version 7.3. However, in the configuration with NanoScope IIIa controller, Quadrex extender and software version 5.31R1, the displayed amplitude is a factor $(3{,}92 \pm 0{,}3)$ higher than the measured signal. Taking this into account and using a tip cone height of $15\,\mathrm{\mu m}$ (PPP-EFM, NanoSensors) I calculated for the real oscillation amplitude:

$$A_{real}^{NS\ IIIa} = A_{softw} \cdot \frac{1}{(3{,}92 \pm 0{,}3)} \cdot (2.552 \pm 0{,}013)\,\mathrm{mrad\,V^{-1}} \cdot 15\,\mathrm{\mu m}$$

$$= A_{softw} \cdot (9.6 \pm 0.4)\,\mathrm{nm\,V^{-1}} \tag{5.1}$$

$$A_{real}^{NS\ V} = A_{softw} \cdot (37.6 \pm 0.2)\,\mathrm{nm\,V^{-1}} \tag{5.2}$$

## 5.1.2 Distance Dependence of the Torsion Amplitude

The following experiments have been performed on a Veeco Multi Mode (NanoScope V Controller)[1] with a NanoSensors PPP-EFM cantilever. The vertical force constant of the lever was determined to be $2.2\,\mathrm{N\,m^{-1}}$ with the thermal noise method.

Figure 5.3 shows the torsion amplitude and the vertical cantilever deflection as a function of the vertical sample displacement on two different samples. The first curve was recorded on highly oriented pyrolytic graphite (HOPG, figure 5.3 (a)). The torsional amplitude in the approach (trace) direction dropped directly from its free air value of $11\,\mathrm{nm}$ to almost zero. Only a very small residual amplitude of $(380 \pm 90)\,\mathrm{pm}$ was observed. Simultaneously, the vertical cantilever force jumped to a value of $-9\,\mathrm{nN}$. From the linear increase of the deflection signal after this jump I conclude that under the influence of attractive surface forces the tip directly jumped into a stable contact with the surface (a so called *snap-in* event). The mechanical contact of the tip after the snap-in is so strong that the tip is not able to move laterally any more. In the opposite (retrace) direction, the amplitude jumps back to the free air amplitude simultaneously with the detachment of the tip from the surface (snap-out). At this point it has to be mentioned that the normal force

---

[1]In contrast to the configuration with NanoScope IIIa controller and Quadrex box, the NanoScope V controller allows the simultaneous acquisition of up to three freely selectable data channels in the spectroscopy mode.

that is measured by the SFM is always the sum of the cantilever force and the adhesion force when the tip is in contact with the surface. In this case, the force that the tip exerts on the sample is the adhesion force, determined from the snap-out (21.5 nN) plus the cantilever force. Hence, the normal force at the snap-in would be $21.5 \, nN - 9 \, nN = 12.5 \, nN$.
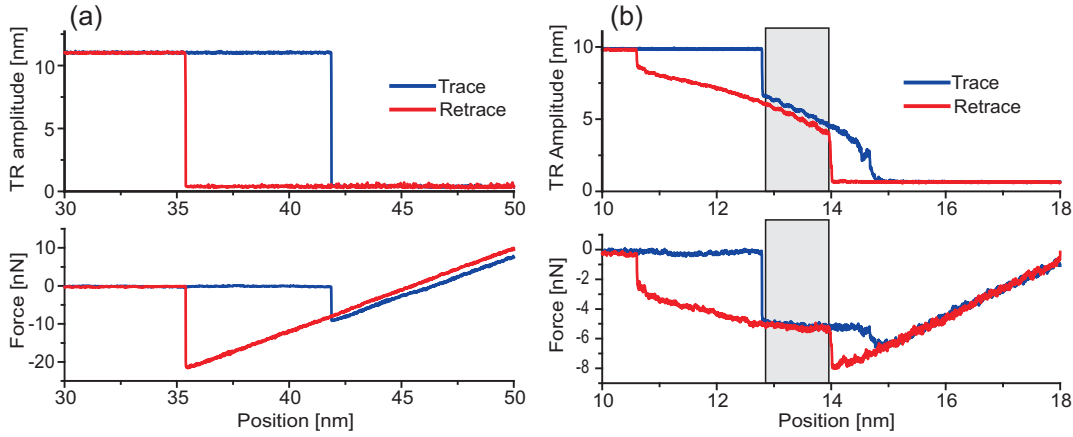

Figure 5.3: Lateral tip vibration oscillation and vertical deflection signal as a function of the sample z-displacement on a) HOPG and b) PEDOT:PSS. The residual torsion amplitude signal is caused by a sideway motion of the cantilever owing to the torsional excitation.

The second sample was a drop-casted film of the conducting polymer composite PEDOT:PSS (see also figure 2.4 on page 12) (Sigma Aldrich, high-conductivity grade, CAS: 155090-83-8). During the approach there was a discontinuous snap-in in the amplitude, as well (figure 5.3 (b)). However, in this case the amplitude only dropped by a factor of one third, from 9.8 nm to 6.7 nm. Simultaneously, the normal force jumped to a value of $-4.8 \, nN$. During the further approach, the torsion amplitude decreased monotonically whereas the vertical cantilever force remained stable around $-5.2 \, nN$. Finally, in a second snap-in the tip established a stable contact with the surface. Now, the amplitude had a constant value of $(620 \pm 20) \, pm$ and the force increased linearly. In the retrace, both jump events can be observed again with a delay of a few nanometers.

It is well known that adhesion of nanoscale objects is accompanied by a deformation of the surface [Joh71, But03]. In the case of the HOPG sample, the tip directly forms a stable contact with the surface. The depression that is formed in the contact region only allows a very small lateral movement of the tip. The direct jump of the amplitude from its free vibration amplitude to zero is in contrast to previous reports. Huang and co-workers reported a continuously decreasing torsion amplitude when they approached a torsionally vibrating silicon tip to a HOPG terrace [Hua04].
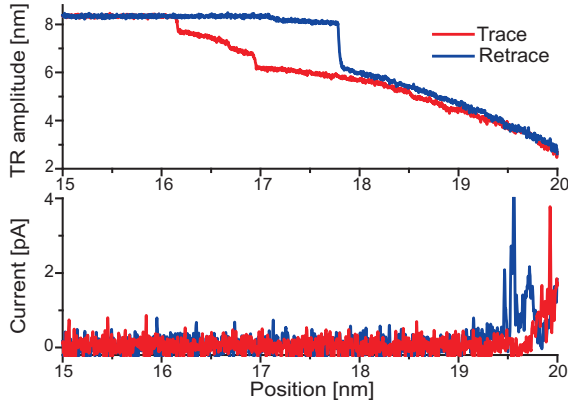
Figure 5.4: Torsional vibration amplitude vs. sample displacement with additional current measurement on PEDOT:PSS. The sample was set to a bias voltage of 3.2 V.

As one source for the torsional vibration damping they discussed adsorbed water. Although HOPG is hydrophobic, the presence of a thin water layer is very probable under ambient conditions. In my experiment, however, I was not able to obtain a torsional vibration in the contact region, not even after directly breathing on the sample. An alternative explanation could be the metal coated tip. In contrast to the sharper, uncoated silicon tips used by Huang they might have stronger adhesion to the substrate.

On the the soft polymeric PEDOT:PSS, the adhesion force is weaker. Therefore, the tip is able to move laterally over the surface without a direct snap-in to a stable contact. The lateral amplitude is damped by in-plane friction forces. These forces grow with increasing normal force until the lateral motion becomes too slow to further prevent the formation of a stable contact - the second snap-in.

A stable imaging of the surface is only possible if there is a continuous and distance dependent amplitude change that the feedback electronics can use to regulate the z-position (gray shaded area in figure 5.3 (b)). Quite remarkably, in the case of the PEDOT:PSS sample this stable operation range occurs at a negative cantilever deflection. In contact mode, no stable operation would be possible at a negative deflection setpoint. Thus, the minimum normal force acting on the sample during contact mode imaging would be the adhesion force plus a minimum positive cantilever deflection. In torsion mode, stable imaging is possible even at normal forces lower than the adhesion force.

In contrast to the intermittent contact mode introduced in section 3.1.1 (page 21), the tip stays in close proximity to the sample surface during the whole oscillation cycle of the torsional motion. Thus, at sufficiently high voltage differences, charge carriers can be exchanged between the tip and a conductive sample. This was demonstrated in an additional ramping experiment. Figure 5.4 shows the torsional amplitude and the current amplifier signal as a function of the sample displacement (sample bias: 3.2 V). The z-approach was stopped before the second snap-in to

prevent an overshoot of the current signal. On the last nanometer of the approach, a fast increase of the current to up to $4\,\text{pA}$ was observed.

5.2 Current Mapping on Reference Samples

The current signal that was observed in the previous experiment (figure 5.4) can also be recorded with a scanning tip during torsion mode imaging. We call this operation mode scanning conductive torsion mode microscopy (SCTMM). In order to test the method, a comparative C-SFM / SCTMM study was performed on a reference structure with defined insulating and conducting structures. In order to elucidate the influence of the torsional amplitude setpoint during SCTMM operation, a second reference experiment on the surface of a soft organic electronic material (PEDOT:PSS) was performed.

5.2.1 Experimental

The first reference sample was prepared by focused ion beam (FIB) assisted chemical vapor deposition (FEI Nova 600, dual beam setup). On a freshly cleaved surface of HOPG, a $30\,\mu\text{m}$ long and $1\,\mu\text{m}$ wide stripe of electrically insulating silicon dioxide was deposited at an ion current of $50\,\text{pA}$ and an ion energy of $30\,\text{keV}$. The thickness was found to be $(8.6 \pm 0.4)\,\text{nm}$ (SFM topography). On top of the insulator a second electrically conducting stripe with the same dimensions and rotated by $90°$ was written by platinum deposition at the same conditions. Its thickness was found to be $(18 \pm 1)\,\text{nm}$. Films prepared by FIB assisted chemical vapor deposition are known to have high carbon contents [Tel02]. Thus, I will refer to the structures as SiOC in the case of the insulator and PtC in the case of the platinum stripe.

The second experiment was performed on a $100\,\text{nm}$ thick blade coated film of PEDOT:PSS (Sigma Aldrich, high-conductivity grade, CAS: 155090-83-8) on an ITO/glass substrate. Before the experiment, the film was annealed in a vacuum oven at $140\,°\text{C}$ for $90\,\text{min}$.

The experiments were done in ambient conditions (humidity $40 - 60\%$) on a Veeco MultiMode (NanoScope IIIa controller, Quadrex extender, TUNA current amplifier). The special cantilever holder used in this study can be used for contact mode, torsion mode and intermittent contact mode imaging. Thus, I used a cantilever whose properties allow for an operation in all three modes (Nanosensors PPP-EFM, nominal vertical resonance frequency of $70\,\text{kHz}$).
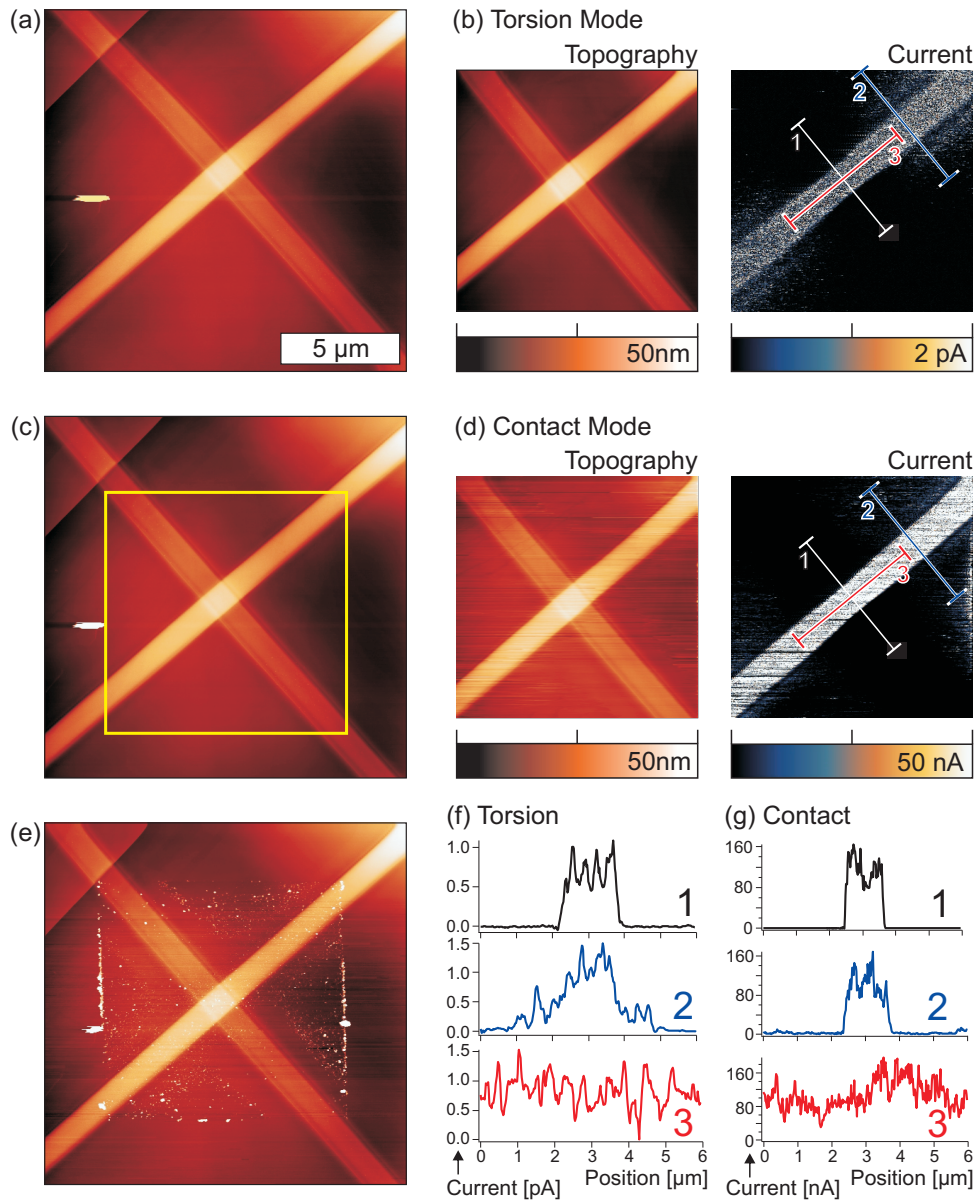
Figure 5.5: SCTMM on a reference crossbar structure (scale bar in (a) valid for all images). The topography before the experiment was measured in intermittent contact mode (a). The results of SCTMM are shown in (b). In the subsequently recorded intermittent contact image (c) no modifications to the surface structure were observed in the previously scanned region (yellow square). After that, the sample was measured in contact mode C-SFM (d). Finally, an intermittent contact mode image shows the damage caused by the last C-SFM measurement (e). (f) and (g): Line plots from the locations marked in the current images of (b) and (d).

5.2.2 Results and Discussion

In a first step, an intermittent contact mode image was recorded in order to have a reference for the topographic structure (figure 5.5 (a)). After that, the PtC/SiOC cross on HOPG was imaged by SCTMM at a sample bias of 50 mV (figure 5.5 (b)). In contrast to the HOPG surface that was investigated in figure 5.3 (page 53), the FIB treated surface yielded enough friction for a stable torsion mode imaging. The comparison of the topography in a and b (left) confirmed that the imaging in a different operation mode did not influence the resulting topographic image.

In the current map of (b) and the three averaged cross sections (f) the basic structure of the predefined insulator/conductor pattern was reproduced. An average current of 0.9 pA was found on top of the PtC stripe. The underlying SiOC stripe had no influence on the structure of the current. Only a slight decrease in the average current to 0.8 pA directly on top of the insulator could be observed. This observation confirms that the platinum stripe formed a homogeneously conductive bridge over the SiOC bar. Next to the PtC, no significant current could be observed on the whole SiOC structure. At the crossing point with the PtC structure, there is a sharp increase in the signal (cross section 1 in (f)). In between the stripes on top of the HOPG an average current of 0.12 pA was measured, which was higher closer to the PtC stripe (see also cross section 2 in (f)). This current increase towards the FIB structures can be explained by overspray during the structuring process with the focused ion beam [Utk08]. Deflected and secondary ions can induce material deposition next to the predefined structure, generating a halo of $1 - 3\,\mu$m radius around the structure, which can be seen in the current map around the PtC stripe (b). It demonstrates that the platinum overspray enhanced the charge injection from the tip to HOPG. However, on top of the SiOC stripe, the halo in the current map disappeared, proving that the thickness of the overspray film is not sufficient to form a homogeneously conductive film. A final intermittent contact mode scan of the investigated area proved that no structural modifications or damage occurred during the SCTMM measurements (figure 5.4 (c)).

In a second experiment, the same structure was investigated by conventional C-SFM in contact mode with the same cantilever at a sample bias of 38 mV (figure 5.5 (d)). The current map shows a qualitatively similar structure compared to the SCTMM result. However, the observed currents were much higher. On top of the PtC, the average current was 100 nA, which is 10^5 times higher compared to SCTMM. In between the stripes, the current dropped to 2 nA and no current could be found directly on the SiOC. In the topographic image, many blurred out horizontal lines can be found indicating a strong cross talk from the currents to the topographic signal. Intermittent contact mode imaging after the experiment revealed severe damage on the sample surface, especially on the blank HOPG surface (figure 5.5 (e)).
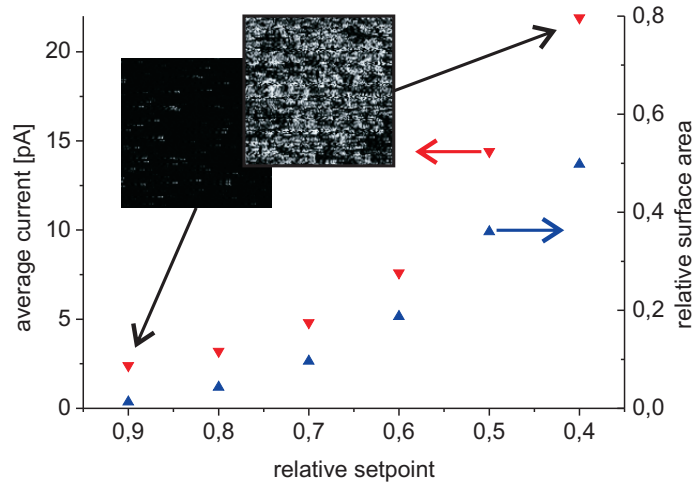
Figure 5.6: Average current (red triangles) and the surface area fraction that carries a current higher than 10 pA (blue triangles) measured on a PEDOT:PSS sample as a function of the normalized amplitude setpoint (free air amplitude = 1). The insets show the recorded SCTMM current maps on an area of 1 μm x 1 μm at two relative setpoints. The gray scale covers a data range of 100 pA.

The influence of adsorbed water on the in-plane damping of the torsional vibration has already been discussed in the previous section 5.1.2 (on page 53). Such a layer would also influence the properties of the injection barrier between tip and substrate. It has furthermore been discussed that the tip-sample forces in contact mode are higher compared to torsion mode. These higher forces will also lead to an increased contact area by the formation of a small indent at the contact point. Depending on the thickness of the water layer, the local topography and capillary forces, the injection barrier height can be subject to huge variations. In the case of torsion mode, the penetration of the adsorption layer on the surface is also possible. However, this will lead to an increased damping of the oscillation of the tip which, in turn, will force the feedback controller to withdraw the tip. In fact, in order to observe a significant current, the amplitude setpoint had to be set to a high damping (60% of the free amplitude).

On the FIB reference structure, stable torsion mode imaging was only possible in a narrow range of amplitude setpoints. Thus, the influence of the torsion amplitude on the current mapping had to be studied on a different sample. Annealed PEDOT:PSS was found to be an appropriate system, as it allows stable imaging over a wide range of amplitude setpoints. At the same time, currents could be recorded at a moderate sample voltage of 20 mV over the whole range of stable amplitude values. Prior to

the experiment, the free torsional amplitude was set to a value of 20 nm at a distance of 1 μm above the sample. This value corresponds to a relative setpoint of 1.

For the plot in figure 5.6, the PEDOT:PSS film was imaged on an area of 1 μm x 1 μm and the average current of the entire scanned area was calculated (red triangles). In order to avoid irreversible modifications to the PEDOT:PSS sample (comparable for example to those in figure 4.6 on page 44 or in [Dan08a] and [Pin08]), the sample had been moved prior to every scan. Thus, each measurement was performed on a pristine sample region.

The structure of the current map showed conductive spots in a mostly insulating matrix (insets in figure 5.6). This fits well with the PEDOT:PSS structure of conducting PEDOT domains in an insulating PSS matrix that was reported in the literature [IZ04]. With decreasing amplitude setpoint, the average current was found to increase. This effect was composed of two factors: (i) The average current per conducting spot and (ii) the overall number of conducting spots was increasing with decreasing setpoint. In order to separate those effects, the fraction of the surface area carrying a current larger than 10 pA was calculated (blue triangles in figure 5.6). This number roughly correlates with the number of conducting spots on the surface. For higher setpoints, the surface fraction grows faster than the average current, whereas at lower setpoints, the current shows a faster increase.

Qualitatively, this effect can be understood by considering the tip-sample force. In figure 5.3 (b) on page 53 it was found that the deflection of the cantilever is constant in the vertical sample displacement range that is relevant for torsion mode imaging. Thus, the effective tip-sample force (the sum of adhesion force and cantilever force) is increasing with decreasing deflection setpoint. In context of the Hertz model, the geometry of the tip-sample contact can be estimated [Her82]. In the case of a planar surface and a tip with radius R, the contact area A_C (radius a) as a function of the normal force F is given by

$$A_C = \pi a^2 = \pi (\frac{3\,R}{4\,E^*}F)^{2/3} \tag{5.3}$$

(E^* is the effective Young's modulus of tip and sample; see [But03] for details). Assuming a homogeneous charge injection on the conductive PEDOT:PSS domains, the tip-sample current is proportional to the contact area. This model works well as long as the conducting domains are larger than the tip-sample contact. However, it does not explain the increase in conducting spots.

It has been reported that on PEDOT:PSS surfaces a thin PSS rich surface layer of some nanometers thickness can be found [Cri03, Hig03]. The charges collected by the tip have to pass this insulating surface layer. In the context of the Hertz model, an elastic deformation of tip and sample is predicted in the contact area. For the given configuration of a hard metallic tip and a soft polymeric sample, most of the

deformation will take place in the polymer. The depth δ of the indentation is given by

$$\delta = \frac{a^2}{R} = R^{-1/3}(\frac{3\,R}{4\,E^*}F)^{2/3}. \tag{5.4}$$

For the mechanical tip-sample interactions such effects have been shown already. In block copolymer blends, the topographic structure was strongly influenced by the amplitude setpoint [Hua04, Yur08]. This effect was ascribed to a penetration of the tip through the first surface layers of the polymeric sample at lower amplitude setpoints. Thus, deeper regions of the sample can interact with the tip at higher normal forces or, in the case of torsion mode operation, at lower amplitude setpoints. In the PEDOT:PSS system, more conductive domains can interact with the tip and the density of conductive spots increases.

5.3 Current Mapping on Nano Pillar Arrays

Free standing nano-pillars with a defined aspect ratio and pitch can be easily prepared by template assisted preparation techniques, e.g. block copolymer templates or anodized aluminum oxide (AAO) [Hab09]. Such structures have been proposed as an ideal morphology for the donor/acceptor bulk heterojunction in an organic solar cell (see [Yan07, Gun07] and section 2.2.3 on page 17). Here, the knowledge of the interplay between morphology and conductivity of individual nano-pillars is crucial for the functionality of the device.

The analysis of free standing organic nano-pillars by C-SFM is often complicated by the deformation and destruction of the sample caused by the forces induced by the scanning tip (see also section 3.2.2 on page 30). One way to stabilize the nano-pillar structure is to remove only the top parts of the aluminum oxide template [Ert06, Wan09b]. First C-SFM studies on freestanding rod architectures made of polypyrrole [Lee08] and core-shell P3HT:PCBM [Wan09a] using soft cantilevers ($k = 0.2\,\mathrm{Nm}^{-1}$) have been presented. However, no simultaneous measurement of topography and current was possible on the setup used in this study. Thus, a direct correlation between nano-pillar morphology and conductivity was impossible.

I will show that the reduced tip-sample forces in SCTMM make a non destructive investigation of such a fragile three dimensional structure possible. This project is a collaboration within the IRTG together with Niko Haberkorn (AK Patrick Theato, University Mainz), who synthesized a novel semiconducting triphenylamine derivate and prepared the nano-pillar arrays used in this study.
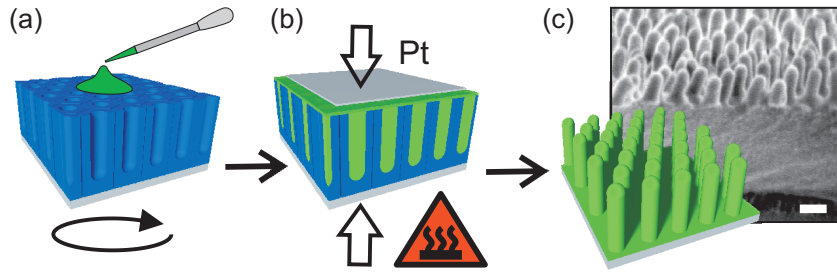
Figure 5.7: Preparation procedure for freestanding nano-pillar arrays. The AAO template is filled with the polymer solution by spin coating (a). After thermal cross linking and the attachment of the substrate (b) the template is removed. A SEM image on a fracture of the resulting TPD nano pillar array is shown in (c) (FE-SEM, Zeiss LEO 1530, scale bar: 100 nm).

5.3.1 Experimental

For the preparation of the nano-pillar arrays an AAO template in analogy to the procedure described in figure 5.7 and [Hab09] was used. This approach allows the fabrication of free-standing nano-pillars on large areas. The length and diameter can easily be varied by the pore dimensions of the template. For this study, arrays of a novel thermally cross-linkable N,N'-bis(4-methoxyphenyl)- N,N'-bisphenyl-(1,1'-biphenyl)-4,4'-diamine (TPD) derivative were investigated. The cross-linking of the semi-conducting TPD polymer provides an enhanced mechanical stability and solvent resistance [Hab10]. It prevents adjacent pillars from collapsing to aggregates. The solvent resistance is important for subsequent deposition steps, where the array is in contact with the solvent of the n-type material. As a comparison, the standard organic donor material poly(3-hexylthiophene) (regioregular P3HT, molecular weight: 25 k, BASF) was used to prepare a nano-pillar array with comparable morphology. The samples were attached to a silicon wafer with a 30 nm thick sputtered platinum layer. This electrode geometry has the advantage of a very low surface roughness.

The experiments were done in ambient conditions (humidity $40 - 60\%$) on a Veeco MultiMode (NanoScope IIIa controller, Quadrex extender, TUNA current amplifier) with Pt/Ir coated cantilevers (Nanosensors PPP-EFM, nominal vertical resonance frequency of 70 kHz).

5.3.2 TPD Nano-Pillar Array

With scanning electron microscopy, a fracture of the TPD nano-pillar array was investigated (figure 5.7 (c)). The length and diameter of the TPD nano-pillars

was measured to be (165 ± 5) nm and (64 ± 2) nm, respectively. Between the nano-pillar array and the Pt-electrode a layer of TPD-polymer of 300 nm in thickness was observed.

Initial attempts to image the sample were done in the conventional contact mode using a soft cantilever (μmash CSC17/Ti-Pt, force constant $0.05 - 0.3$ Nm^{-1}). However, no structure could be resolved, neither in topography, nor in the current map (figure 5.8). Although a very low deflection setpoint was used, the scanning tip bent and destroyed the structures. On some parts of the sample the tip even scratched deeper lying structures of higher conductance (bright parts in 5.8 (b)).
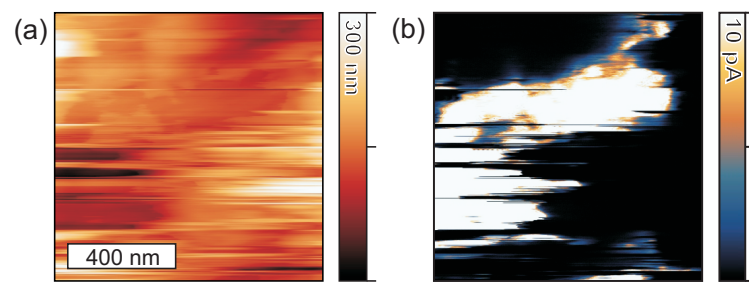

Figure 5.8: Topography (a) and tip-sample current (b) measured on the TPD nano-pillar array in contact mode (sample bias 5.2 V)

Thus, the operation mode was switched to scanning conductive torsion mode microscopy (cantilever: Nanosensors PPP-EFM, measured vertical and torsional frequency of 70.8 kHz and 873 kHz, respectively). The setpoint for the torsional amplitude was set to 2.6 nm. In contrast to the contact mode results, the topography obtained in torsion mode clearly resolved the single nano-pillars (figure 5.9 (a)).

For a comparison of the imaging modes, a interleaved intermittent contact/torsion mode experiment was performed (comparable to dual pass KPFM experiments). The resulting topographic maps were then subtracted in order to visualize the differences (figure 5.9). No larger deviations could be found: on most parts of the sample, the differences were less than 2 nm. This observation proves that the topographic signal obtained in torsion mode is not subject to imaging artifacts, e.g. generated by the lateral movement of the tip. On the topographic map in (a), smaller artifacts are visible on the upper and lower edges of the topography that might be caused by the use of a lower amplitude setpoint, which can induce a minimal bending of the pillars (arrows in figure 5.9 (c)).

The statistical analysis of the relative height differences between the 180 nano-pillars in figure 5.9 (a) gave a standard deviation of 4 nm, demonstrating the uniform pillar height. The topographic image shows that the tip penetrates the gaps between the
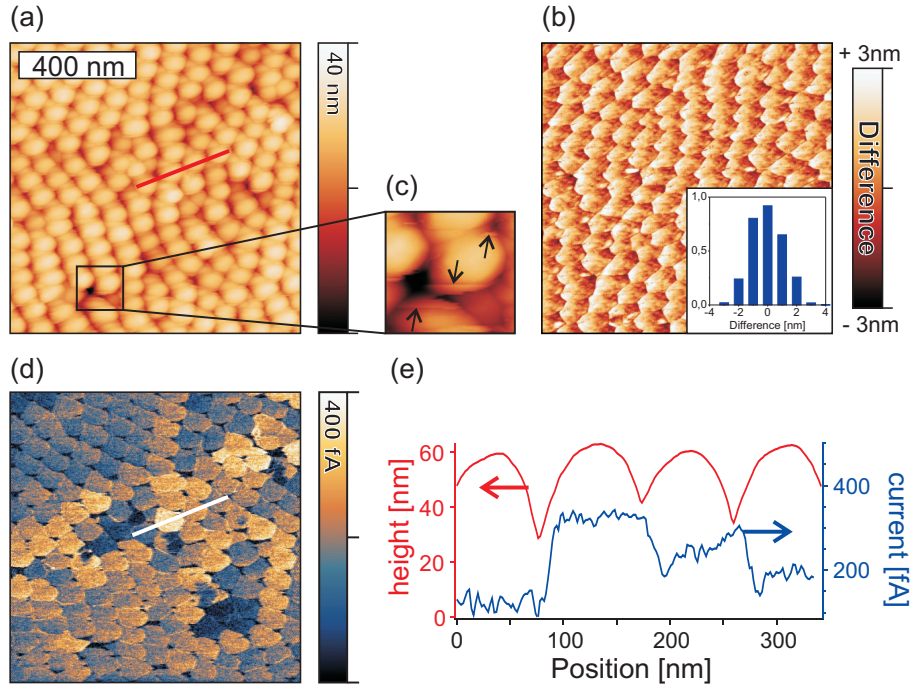
Figure 5.9: SCTMM results on the freestanding TPD nano-pillar array: topography measured in torsion mode (a); difference of the intermittent contact mode height and the torsion mode height data measured in interleaved scan lines on a different sample position (b) (inset: histogram of the data); enlarged detail of the topography showing smaller imaging artifacts (c); tip-sample current map recorded simultaneously with (a) at a sample bias of 12 V (d) and line profile on the same position in topography (red) and current (blue), demonstrating the good correlation between topography and current (e).

rods to a depth of $30 - 40$ nm. This behavior can be expected from the tip geometry (radius of curvature 20 nm), the diameter and pitch of the nano-pillar structures.

The current map revealed distinct current domains of up to 340 fA (figure 5.9 (d)). Since the topography and the current map were recorded simultaneously, each of the current domains can be associated with a single nano-pillar. The current is uniform on top of one specific nano-pillar (root-mean square value 60 fA). Clear transitions between adjacent nano-pillars were resolved, which correspond to the minima in the topographic image. Exemplarily, the topography and the current signal of three adjacent nano-pillars along the line indicated in figure 5.9 (a) and (d) were plotted. In between two neighboring nano-pillars I measured a sharp transition in the current, typically within $10 - 30$ nm (figure 5.9 (e)). Thus, the currents can be clearly associated to the conduction through one specific nano-pillar. Qualitatively,
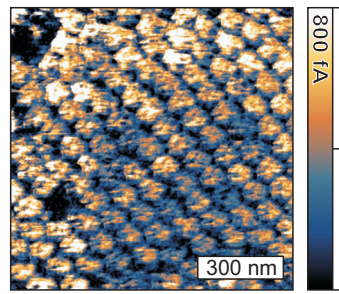
Figure 5.10: Current map recorded on the same sample at a negative sample bias of $-12\,\mathrm{V}$.

the same results with slightly higher and less homogeneous currents were obtained at a negative sample bias of $-12\,\mathrm{V}$ (figure 5.10).

For a statistical evaluation of the images, all areas of the individual nano-pillars were defined as a mask in the topographic image ("watershed" algorithm in the free SPM data analysis software gwyddion). This mask was then used to determine the mean current of each rod (red bars in figure 5.11 (a). For this analysis we used a conductivity map which was obtained on a larger scan area of (5x5) $\mu\mathrm{m}^2$ covering 2660 rods (figure 5.11 (b) and (c)). The histogram of the current distribution shows a maximum for pillars corresponding to a current value of $160\,\mathrm{fA}$. An average current for all measured pillars of $(240 \pm 140)\,\mathrm{fA}$ was determined. Only a minority of nano-pillars (below 2%) exhibit a current lower than $60\,\mathrm{fA}$ (the noise level of the current measurement).

A possible explanation for the conductance variations would be differences in the height of the nano-pillars. However, a correlation between the heights of the nano-pillars with their current could not be found. Another source for variations in the current could be differences in the contact of the triarylamine polymer layer with the Pt-electrode. However, the thickness of the underlying uniform polymer layer was found to be almost twice compared to the length of the nano-pillars (Figure 5.7 (c)). This layer smears out the current that flows between the platinum electrode and the tip. Thus, contact variations with the bottom electrode can only explain conductance variations on larger scales. The huge differences in the conductivity that is visible even on adjacent nano-pillars (e.g. in the section view in figure 5.9 (e)) can thus not be attributed to the substrate contact. As the tip only touches one nano-pillar at a given time, the measured differences in the electrical current must be attributed to the individual structure and/or material properties of that particular nano-pillar. Effects that may be considered are different densities of defects, variations in the alignment of the TPD moieties and surface impurities.

Finally, in order to rule out that the recorded current maps were influenced by parasitic electrical currents between the SFM-tip and the substrate, a further reference experiment was performed with a deliberately aged sample. Organic electronic materials are known to be sensitive to degradation induced by light, oxygen or humidity [Jør08], which results in a dramatic decrease in conductivity. On a sample

64
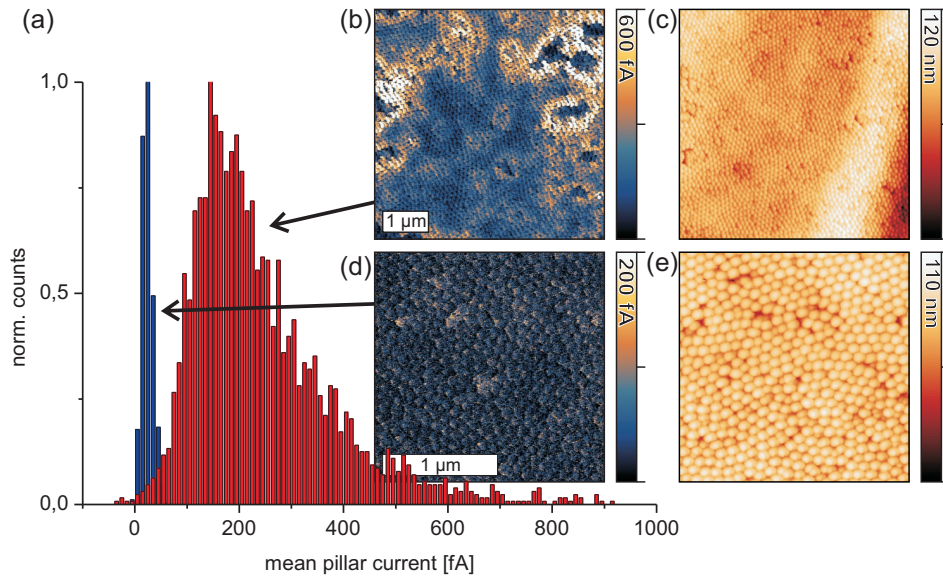
Figure 5.11: Statistical evaluation of the pillar currents (a) obtained from a larger scan (current (b) and topography (c)) and from a degraded sample (current (d) and topography (e)).

stored in ambient lab air for two weeks, a significantly lower current (factor of 10) was observed at an identical bias voltage of 12 V (figure 5.11 (d)). However, the topography of the nano pillar array remained unchanged (figure 5.11 (e)). Here, the statistical analysis of 514 rods gave a mean current of $(24 \pm 11)\,\mathrm{fA}$ (blue bars in figure 5.11 (a)). Thus, the current that was measured in the fresh sample was caused by the intrinsic conductivity of the polymer material.

## 5.3.3 P3HT Nano Pillar Array

In order to compare the results on the novel nanostructured TPA polymer system with a standard polymer in a similar geometry, a second set of samples was prepared from the semiconducting polymer of poly(3-hexylthiophene) (P3HT).

The topography of the P3HT nano-pillar sample shows a homogeneous coverage with mostly free standing nano-rods (figure 5.12). Here, no artifacts comparable to those observed in figure 5.9 (c) occurred, which can be attributed to a reduced aspect ratio and thus higher mechanical stability of the P3HT pillars (pillar length: $(110 \pm 5)\,\mathrm{nm}$). The rods were uniform in height, the standard deviation of the maximum rod height among the 1079 nano-rods in figure 5.12 (a)) is 5 nm (the image was flattened only with a first order fit routine). With 120 nano-pillars per
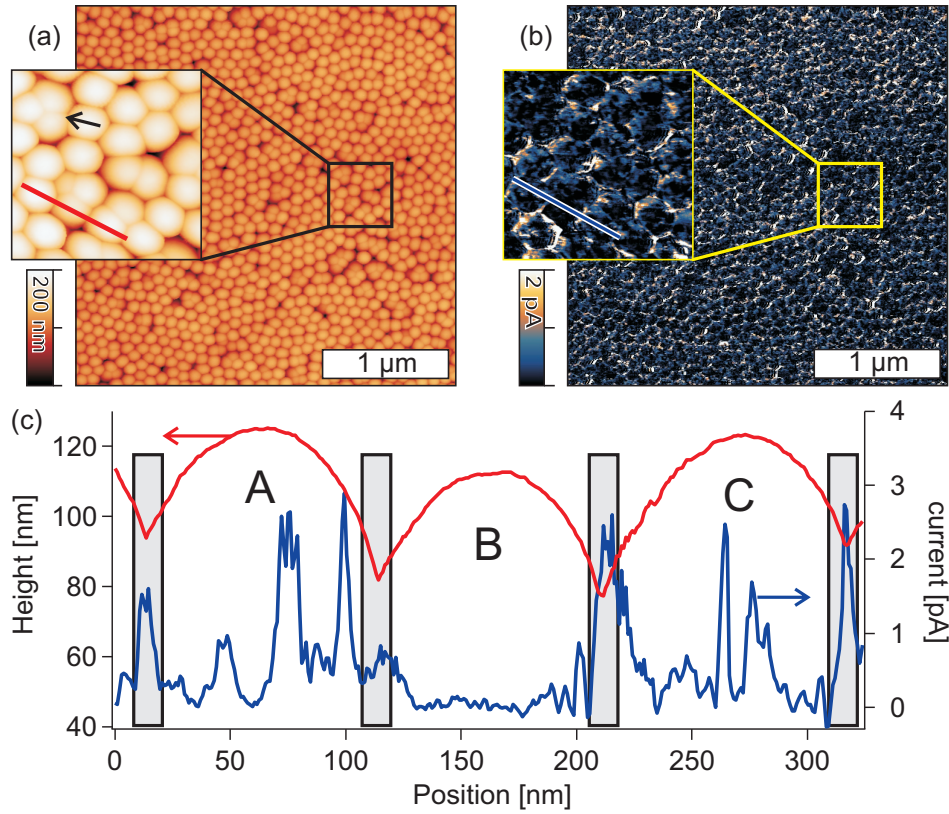
Figure 5.12: (a) Topography and (b) current map on a P3HT nano-pillar array. The black arrow in the magnification of a points towards a cluster of three aggregated nano-pillars. (c) section view of the topography (red) and the current (blue) from the lines indicated in the insets in (a) and (b).

Figure 5.13: If the tip can penetrate the gaps between the nano-pillars, the effective contact area is smaller on the top (1) compared to the contact area on the side (2) of the nano-pillar.
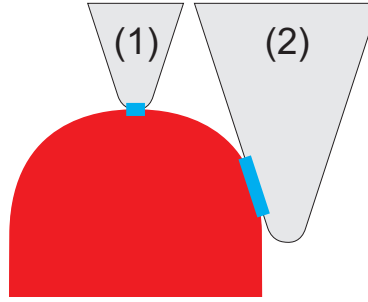
μm^2 the density comparable to the TPD nano-pillar sample. At some places, two to three adjacent rods seem to have fused (arrow in the inset of figure 5.12 (a)). This effect can be attributed to agglomeration of the nano-rods. Furthermore, the topography shows that the tip penetrated some of the gaps between adjacent nano-rods to a depth of up to 100 nm. The reason could be a wider distance between adjacent nano-pillars, in particular next to agglomerated pillar clusters.

In the current image, no large insulating areas were found on the nano-rod array at a sample bias of 2 V (see 5.12 (b)). The correlation with the height data in a profile view reveals that in large parts of the gaps between adjacent nano-rods an increased current was recorded (gray shaded areas in figure 5.9 (c)). Especially in larger gaps, higher currents are recorded (for example in the gap between B and C in figure 5.9 (c)). There are two plausible explanations for this behavior: (i) The tip penetrates the gap deep enough to interact with the substrate and (ii) the effective contact area increases as the shaft of the tip also interacts with the pillars (see figure 5.13).

In contrast to the TPD nano-pillar array, the current on top of the P3HT nano-rods was not homogeneous. Conductive patches of $10-20$ nm in size were found on almost every nano-rod (e.g. the peaks in particle A and C in figure 5.12). They carry a current of typically 300 fA up to some pA, which is significantly higher than the average current of (200 ± 100) fA. Such patches have been observed on planar films of P3HT by scanning tunneling microscopy [Gre03]. The authors ascribed these structures to crystalline domains embedded in a less conductive, amorphous polythiophene matrix.

So far, the operation of SCTMM was found to be more gentle compared to the standard C-SFM operation. However, when the SCTMM parameters are not chosen carefully, irreversible sample damage can occur in SCTMM, as well. In particular, if the sample voltage is set too high, the tip-sample current can cause irreversible modifications [Lin02] or even the destruction of the surface [Pin08, Dan08a]. In figure 5.14, the results of a second P3HT nano-pillar sample is shown. The topography (a) shows a less homogeneous distribution of nano-pillars compared to figure 5.12. A higher fraction of pillars were aggregated and larger gaps between particle clusters could be observed. In these gaps, the highest currents of up to 80 pA were recorded
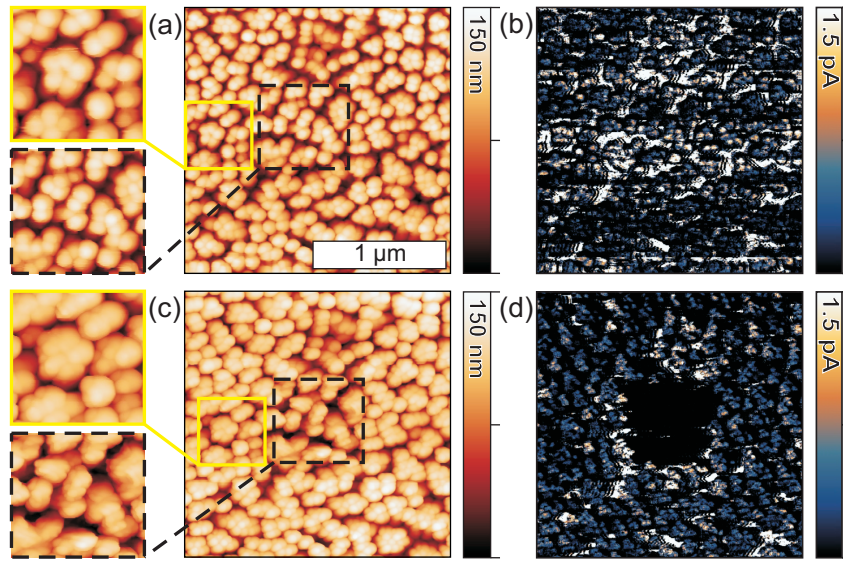
Figure 5.14: P3HT nano-pillar array before ((a) and (b)) and after ((c) and (d)) the central region was imaged at a sample voltage of 10 V. In addition to a tip modification (upper cut-out in (a) and (c)) the sample in the central region was modified as well (lower cut-out). The latter region became completely insulating (d).

(sample voltage 2 V, figure 5.14 (b)). On top of the pillar structures, an average current of 300 fA was measured, which is consistent with the previous P3HT sample.

After this first imaging at a moderate voltage, the scan size was decreased to 500 nm and the sample voltage was set to 10 V (dashed square indicated in figure 5.14 (a)). The subsequent full size SCTMM image revealed a slightly altered topography. In the first SCTMM topographic image, single nano-pillars were clearly resolved, even on the aggregate structures (see magnification in figure 5.14 (a)). After the high voltage scan, the nano-pillar clusters appeared less defined and more cloud-like, even outside of the high voltage scan. This can be ascribed to a modification of the tip during the high voltage scan, either by a destruction of the tip apex or by sample material that attached to the tip. Owing to this altered tip geometry, the aggregates appeared broader and thus, the gaps in between the clusters narrowed. In the central region, however, the gaps have become broader, indicating an additional modification in the sample structure.

Most remarkably, however, is the complete loss of sample conductance in the high voltage scan region (figure 5.14 (d)). The rest of the sample exhibits an only slightly decreased conductance. At a sample voltage of 2.5 V, an average current of 250 fA was measured on top of the nano-pillars and clusters. The decreased penetration into the gaps was also reflected in a reduced number of high current spots in those

regions. The center of the sample, however, remained completely insulating. A possible explanation for this behavior could be a heating effect caused by the presence of high current densities. This heating could lead to rearrangements in the polymer structure that leave the sample in an amorphous and thus less conductive state. It could furthermore lead to an oxidation of the P3HT, which also deteriorates the conductivity.

5.4 Charge Injection Mechanism

Further insights into the charge injection mechanism of individual nano-pillars can be obtained by recording local current-voltage characteristics (see also section 3.2.1 on page 27). In SCTMM, this kind of measurement can be performed by positioning the tip on the sample with active feedback. Figure 5.15 shows a current-voltage plot recorded on the TPD nano-pillar array with several plot types.

In figure 5.15 (a) the current voltage data recorded on a single TPD nano-pillar is plotted in a linear plot. For a better visibility, the data was split into positive current (blue squares) and negative current (red circles). In the Fowler-Nordheim plot (b) no linear behavior can be observed. Thus, quantum mechanic tunneling can be ruled out as the limiting charge injection mechanism. In the Richardson-Schottky plot (c) the approximation by a line fit works much better. Here, the fit for the positive current data generates a slightly better result compared to the negative current (sum of error squares 81 (neg) compared to 131 (pos)). Finally, to test the space charge limited conduction model, the data was displayed in a double logarithmic plot (d). The fitting of a power law (ax^b) yields a power of $b = 1{,}94 \pm 0{,}01$ for the negative current. This is very close the the value of $b = 2$ that would be expected from a space charge limited injection current in a solid. For the positive current, the best fit yields an exponent of $b = 1{,}27 \pm 0{,}01$. This value is even below the exponent of space charge limited injection into vacuum ($b = 3/2$).

In literature, several modifications to the space charge limited injection model have been proposed in order to explain exponents in the current voltage characteristics that differ from the solid or vacuum case. Owing to the strong hopping transport in disordered organic electronic materials, Poole-Frenkel type conduction with a field dependent mobility could be considered. At higher electric fields, it is easier for charge carriers to escape from trap states, which makes them more mobile. This model was often successfully used to fit current-voltage data [Boz99, Cam99, Lin02]. In the case of the positive bias current in my experiments, however, the current increase is lower at higher electric fields - the opposite effect.

Chandra and co-workers assumed a combination of vacuum- and solid space charge limited conduction. They simulated the effective exponent of the current voltage
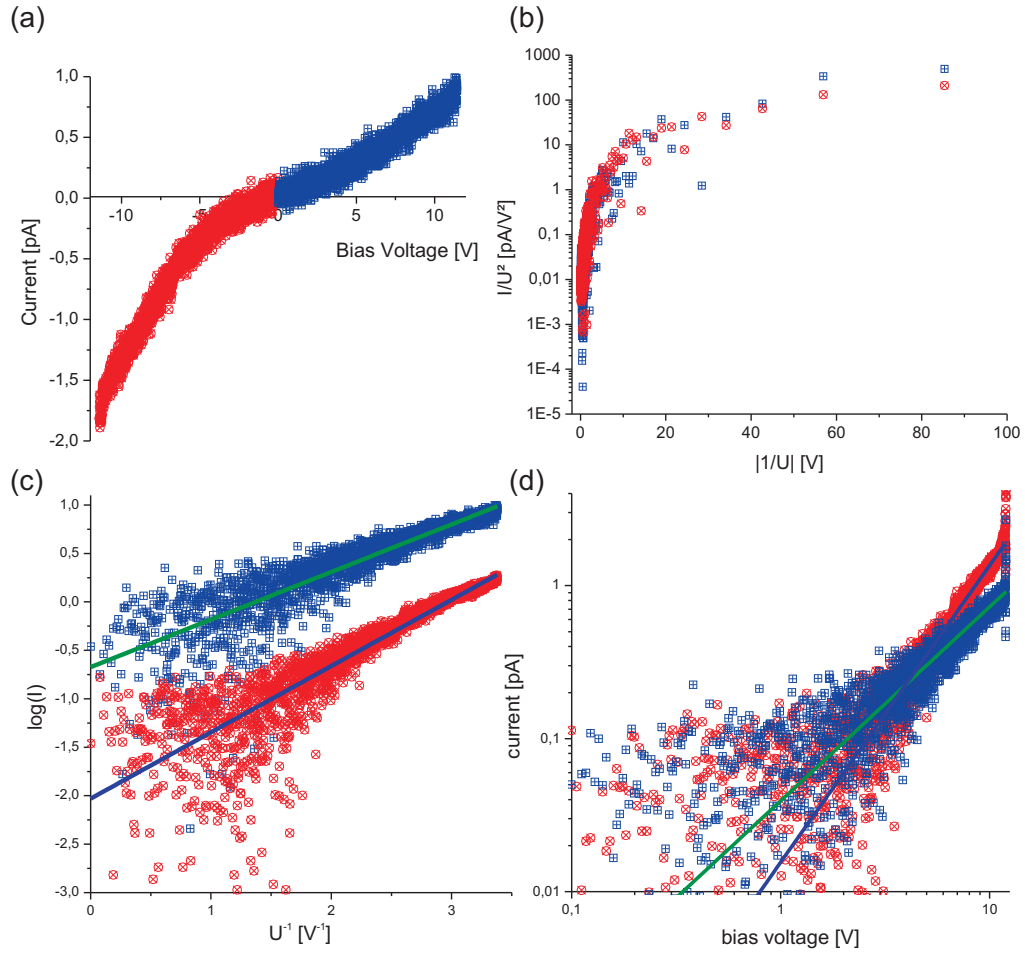
Figure 5.15: Current voltage data recorded with SCTMM. The current values at positive sample bias are plotted in blue squares and the negative bias values in red circles. Plot (a) is the data in a linear plot, (b) Fowler-Nordheim plot, (c) Richardson-Schottky plot (the data points corresponding to negative bias have been shifted for better visibility) and (d) a double logarithmic plot.

Figure 5.16: (a) In homogeneous films, the current paths from the tip to the substrate do not follow straight lines; directly under the tip there is a volume of high current density. (b) In the case of the nano-pillars, the current direction is given by the geometry of the tip.
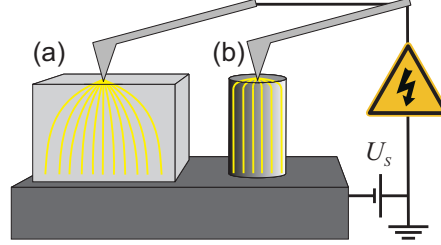
characteristics as a function of the fraction of free space (vacuum) to solid in the gap between the electrodes and found that the exponent tends continuously from the pure solid case ($b = 2$) to the vacuum case ($b = 3/2$). However, during torsion mode operation it is very unlikely that there is a significant fraction of free space between the tip and the sample (see data in figure 5.3 on page 53 and [Yur08]).

In the given geometry of an organic semiconductor in between two metal contacts, the formation of a Schottky barrier at one of the contacts is the most feasible explanation for the asymmetric current voltage behavior.

For a quantitative analysis of current-voltage experiments, Reid and co-workers have studied space charge limited currents measured with C-SFM on planar films of conjugated polymers [Rei08]. They found that C-SFM experiments overestimate the charge carrier mobility by up to 3 orders of magnitude. In most experiments, a planar electrode geometry is assumed, where every current path runs on a straight line perpendicular to the electrodes. They used finite element simulations to account for the proper tip-sample geometry and found a modified Mott-Gurney law that yielded mobilities close to those measured in a planar device geometry. The simulation demonstrated that the current spreads out under the tip forming a volume of high current density in a radius five to ten times larger than the tip apex (figure 5.16 (a)).

This model, however, does not apply for the system studied here, as the current path is determined by the nano-pillar geometry. Thus, a planar electrode geometry can be assumed for the further calculations (figure 5.16 (b)). I calculated the mobility under the assumption of pure Mott-Gurney type conduction at negative sample bias (i.e. hole injection from the tip to the sample). Furthermore I assumed that the compact polymer layer under the nano-pillars and the contact to the substrate does not further influence the charge conduction. Thus, the conduction is limited by the nano-pillar geometry, namely by the height $h_{pillar} = (165 \pm 5)\,\text{nm}$ and the cross sectional area $A_{pillar} = \pi((64 \pm 2)\,\text{nm}/2)^2$. Fitting the data in figure 5.15 with a quadratic function $y = ax^2$ yields a prefactor of $a = 0.014\,\text{pA/V}^2$. Using equation

(3.14) (page 30) and setting $\epsilon = 3$ (typical value for polymers [Lin02]) we get:

$$j_x(U) = \frac{I_{tip}(U)}{A_{pillar}} = \frac{9}{8}\mu\epsilon_0\epsilon\,\frac{U^2}{h_{pillar}^3},$$

$$I_{tip} = \frac{9\,\mu\epsilon_0\epsilon\,A_{pillar}}{8\,h_{pillar}^3}U^2 = a\,U^2$$

$$\Rightarrow \mu = \frac{8 \cdot a \cdot h_{pillar}^3}{9 \cdot \epsilon_0\epsilon \cdot A_{pillar}}$$

$$= 6.5 \cdot 10^{-6}\,\mathrm{cm^2\,V^{-1}\,s^{-1}} \tag{5.5}$$

This value is in the range of typical charge hole mobilities for polymeric organic semiconductors [Bar10]. However, the current mapping demonstrated huge variations in the pillar currents. As the charge carrier mobility is strongly influenced by the local packing of the polymer chains, this value has to be seen as the individual value for one specific nano-pillar.

For a final decision on which injection type is dominant, additional experiments at different temperatures should be performed. If the injection current is temperature dependent, thermionic emission might play an additional role. Furthermore, the electrode structure could be optimized to ensure unipolar injection at the bottom electrode and the tip coating could be varied to optimize energy level alignment and thus to minimize the injection barrier. Finally, the experiments could be performed at higher voltages to increase the data range.

5.5 Summary

It was demonstrated that the combination of current measurements with scanning torsion mode microscopy is a useful extension to standard conductive scanning force microscopy. The normal force that the tip exerts on the sample during scanning can be kept below the adhesion force of the tip-sample system. The reduced normal force has two consequences: First, the contact area between tip and sample becomes smaller and thus, the recorded currents are some orders of magnitude lower compared to the conventional imaging contact mode. Second, the imaging becomes much more gentle. The reduced normal force also reduces the friction with the sample during scanning. Thus, scanning conductive torsion mode microscopy allows studies on soft and fragile samples that could not be investigated by the standard technique.

In particular, the described mode can be applied to vertical nano-rods, wires or pillar array structures without bending or destroying the surface structure. The same analysis performed by conventional conductive SFM operated in contact mode lead to the removal of the nano-pillars from the surface. Thus, the here presented

mode allows a more detailed study of topography and current at one position since the topography and current data are recorded simultaneously.

However, a careless choice of operation parameters can cause sample damage in SCTMM, as well. In particular, parts of a P3HT nano-pillar sample were transformed into an electrically insulating state. Although modifications in the sample structure were observed, the principle surface structure of the pillars survived. This implies that information can be actively written into the sample. The possibility to address *individual* nano-pillars allows to set one particular nano-pillar into a defined state of conducting or insulating. With the given type of arrays, data densities of 80 Gigabit per square inch would already be possible. By optimizing the material and the structure, repeated writing and higher data densities would be possible.

Finally, a current-voltage experiment performed on a single TPD nano-pillar was analyzed. It yielded further insights to the charge injection mechanism in the SCTMM experiments. Quantum mechanic tunneling could be ruled out as the limiting process. By assuming space charge limited conduction, the charge carrier mobility of a single nano-pillar could be calculated. With this type of analysis, charge conduction phenomena in nanostructured matter can be measured directly. The comparison with planar geometries for example in thin films could give insights into the influence of the templating process on the molecular packing.

6 Photoelectric Scanning Force Microscopy
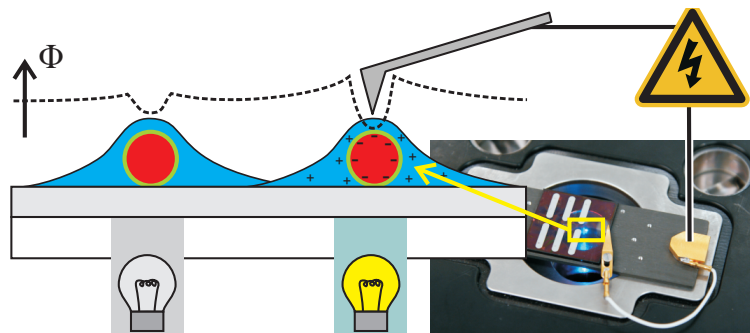
So far, the electric SFM studies have been performed on passive structures. Conductive SFM could visualize nanoscale variations in the conductance of functional nano structures under the influence of an externally applied electric field. With Kelvin probe force microscopy, changes in the work function were studied on equilibrium structures. The investigated materials, however, all have possible applications in photovoltaic devices and thus the potential to become *active* nanostructures when interacting with light. The previous studies have demonstrated that electric SFM modes would be the ideal tool to investigate the photoinduced electrical response of such structures.

A SFM setup that allows to study light induced effects on organic electronic nanostructures should fulfill the following requirements:

- The sample holder should have an optical access from the substrate side. Sample illumination from the top would generate a shadow under the cantilever that makes it difficult to estimate the illumination intensity.

- The light source for the sample illumination should be stable in terms of output power and spectral stability. For studying dynamic effects, an external modulation of the light source, for example for generating light pulses, would also be beneficial. Finally, the illumination spot should have a homogeneous intensity profile. All these requirements are best met by a laser source. The

wavelength should be in the main absorption bands of the photoactive layer and long enough not to cause photo bleaching or other UV-induced degradation processes. Ideally, the wavelength is in the range of $450 - 550\,$nm.

- The laser that monitors the cantilever deflection should have a long wavelength. The energy of the photons should not be sufficient to generate excitations across the band gap of typical organic semiconductors. Ideally, the SFM laser is controlled by the software and can be switched off during local current-voltage experiments.

- The software control of the SFM should be flexible enough to enable the user to generate custom measurement procedures, such as the afore mentioned current measurement with deactivated SFM laser.

- Organic electronic materials are very sensitive towards oxygen or water, in particular in combination with light irradiation [Jør08, See09]. The SFM experiments should thus be performed in an inert atmosphere with low oxygen and water content. This can be achieved by performing the experiments in a sealed sample cell under a constant gas flow [Cof07]. Such cells are used for example for experiments performed in liquid environments. However, changing the samples is difficult as the whole sample cell has to be transferred into a glove box. An easier approach is to put the whole SFM into a glove box under inert atmosphere.

None of the existing SFM setups at the Max Planck Institute for Polymer Research met all these requirements. Therefore, one of my goals was to built an additional setup for photoelectric SFM experiments in inert atmosphere.

6.1 MFP3D Setup

With the Standalone version of the Molecular Force Probe 3D (MFP3D) from Asylum Research we found a scanning force microscope that met most of the requirements stated above. Nevertheless, some additional modifications were necessary. First, the instrument was placed in an acrylic glass glove box (type P10R180T2, GS Glovebox Systemtechnik GmbH) that can be constantly flushed with dry nitrogen. Under these conditions, the sensors in the box display an atmosphere with less than 0,1 % humidity and less than 0,01 % oxygen. An acrylic box of this size is very susceptible to accoustic noise. Thus, the whole setup was placed in an accoustic chamber. To protect the experiments from vibrations in the building, the setup was placed on a massive marble plate supported by foam concrete blocks (figure 6.1 (a)). Additionally, the microscope was placed on an active vibration table (Halcyonics Nano 30, figure 6.1 (b)).
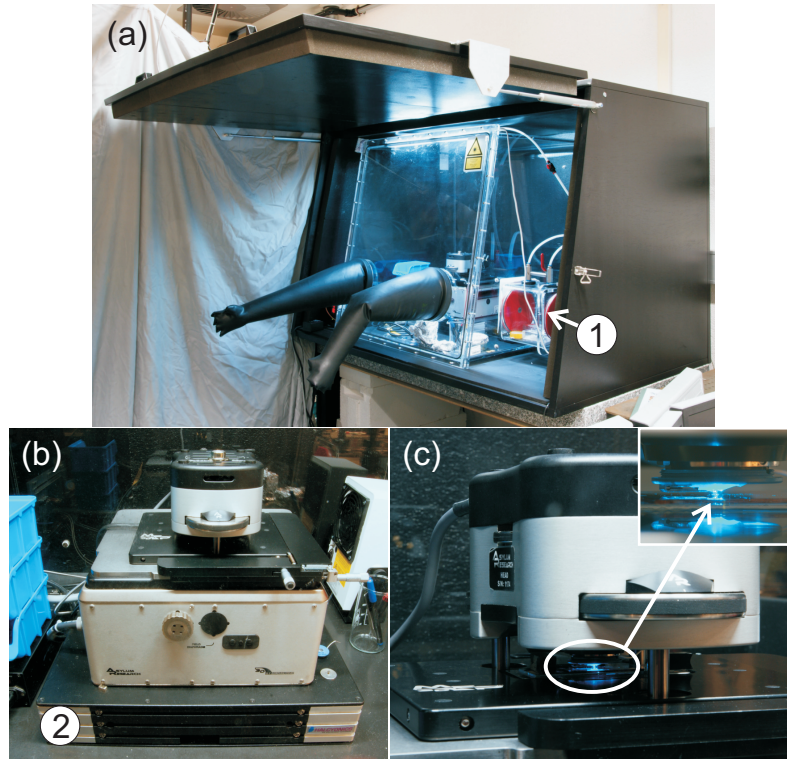
Figure 6.1: Setup of the Photoelectric SFM. The SFM is placed in an acrylic glove box inside an acoustic chamber (black box) to shield the experiment from noise, humidity and oxygen (a). Samples and additional equipment can be passed into the glove box via an air lock (1). Additionally, the SFM (b) is placed on an active vibration isolation (2). The SFM head with activated sample illumination (c). The inset shows a magnification of the cantilever holder with the cantilever (arrow).

The base of the microscope was modified with additional optics for the sample illumination. A fiber coupled diode laser (Point Source, iFLEX2000) with a nominal output power of 15 mV and a wavelength of 488 nm was installed for the sample illumination (figure 6.1 (c) and (d)). Owing to the fiber, the actual laser unit could be placed outside the glovebox. The output power of the laser beam can be modulated via an analog coaxial connector at a frequency of up to 5 MHz (manufacturer data sheet). For the positioning of the laser spot on the sample, a motorized mirror with an in-house made motor control electronics was developed.

6.1.1 Characterization of the Illumination Laser

For reproducible experiments, exact knowledge of the laser beam characteristics, such as power density or the modulation behavior is of extreme importance. The
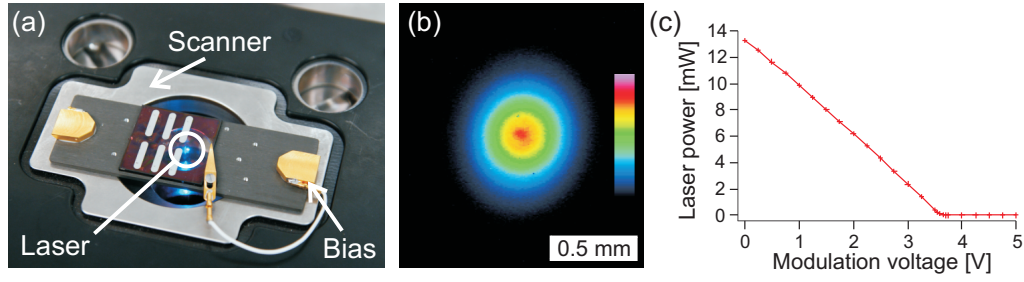
Figure 6.2: (a) MFP 3D scanner with sample holder. The electrical connection to the sample is made via a magnetic pad at the side of the sample holder. On the sample, the laser spot can be seen. (b) Beam profile measured with a beam profiler. (c) Laser output power as a function of the voltage at the analog modulation input.

power of the laser at the sample position was measured to be 13.3 mW (Newport Optical Power Meter, model no. 835 with a detector model no. 818-SL). The beam profile was recorded with a Coherent BeamView-USB Analyzer (figure 6.2 (b)). The beam was found to have a symmetric Gaussian profile with an average $1/e^2$ diameter of 640 µm at a peak-to-average power ratio of 2.39. Thus, the average and peak intensity of the beam are 4.1 Wcm^{-2} and 9.9 Wcm^{-2}, respectively. For photoelectric SFM experiments, the tip is positioned in the center of the laser spot. Here, the laser beam has its highest power and the intensity profile is homogeneous on the typical length scales of SFM scans.

The dependence of the laser output power to the applied voltage at the modulation input is plotted in figure 6.2 (c). The power decreases linearly with the modulation voltage (at 3.72 mW per volt) from zero (full laser power) to 3.63 V (power below 100 µW). From 3.63 V to 5 V the laser still emits light at an intensity in the micro to nano watt range. At 5 V modulation voltage the laser is completely dark. This dependence has to be taken into account when experiments at lower or time dependent intensities are carried out.

## 6.2 Charge Separation in Functionalized Nanostructures

In hybrid solar cells, the proper design of the interface between the inorganic and the organic material is of supreme importance. Here, the excitons are split into individual charges, facilitated by the energetic offset between the electron donor and acceptor material. However, numerous processes close to the interface can deteriorate the device performance:

- Excitons generated far away from the donor-acceptor interface will recombine before they can be split into separated charges.

- If the separated charge carriers are not collected efficiently, they may recombine, as well.

- Insufficient contact between the donor and the acceptor material over the whole interface area can additionally decrease the light harvesting efficiency.

In order to tackle all these problems, a model system for a solar cell with optimized interface structure was developed in the Zentel group at the University of Mainz. It is based on ZnO nano-rods as the electron conducting part. In addition to a high specific surface area, the elongated structure of the nano-rods can provide conduction pathways for efficient charge collection. For the hole-conducting part, a modified conjugated triphenylamine (tetraphenylbiphenyldiamin, TPD) was combined with a perylene dye and an anchor group in a single block copolymer. The anchoring dopamine group can covalently bind to the ZnO [Zor08]. By combining the anchoring group and the dye in one block, the light absorption close to the interface should be enhanced.

A first indication towards a charge transfer from the polymer to the ZnO was found by photoluminescence spectroscopy. Here, the sample is illuminated with a strong light source in the near-UV region and the emission at longer wavelengths is recorded. One source for this emission is the recombination of excitons generated by the near-UV light. If some of the excitons are dissociated by a donor acceptor interface, the emission is reduced or - in other words - the photoluminescence is quenched. This effect was observed for the previously described block copolymers following the attachment to the ZnO nano-rods (figure 6.3 (a)).

If the light absorption causes a charge transfer from the dye/TPD system to the ZnO nano-rod, the internal potentials in the particle-polymer system should change (figure 6.3 (b)). I will demonstrate that these potentials can be visualized on a single particle level by means of Kelvin probe force microscopy in combination with light irradiation. This work was done in an IRTG collaboration together with Matthias Zorn (AK Zentel, University Mainz), who carried out the synthesis of the block-copolymer and the sample preparation.
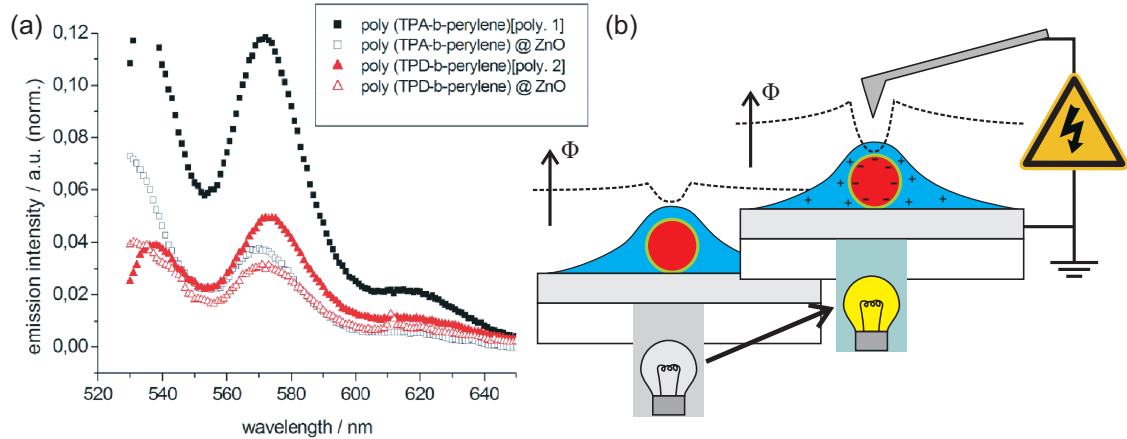
Figure 6.3: (a) Photoluminescence spectra of the pure polymer (filled symbols) and the polymer attached to the ZnO nano-rods (open symbols) for two different triphenylamine derivates (data provided by Matthias Zorn [Zor10]). (b) The photo-induced charge separation should lead to a change in the internal potential of the particle-polymer system that can be detected by KPFM

6.2.1 Kelvin Probe Force Microscopy

The functionalized nano-rods were spin-cast from a toluene solution on a transparent and conductive substrate (indium tin oxide, ITO). Surface potential maps of the functionalized particles were recorded in the dark (figure 6.4 (a)) and under laser illumination (figure 6.4 (b)) at a scan height of $10 - 20\,\mathrm{nm}$ above the surface. The potential maps showed several elongated structures of $200 - 400\,\mathrm{nm}$ length and $60 - 80\,\mathrm{nm}$ width, which can be associated to particles on the surface (see also topography in figure 6.5 (a)). The contrast that is visible in the unilluminated sample is caused by the work function difference between the ZnO, the polymer and the ITO substrate. In order to separate this static contrast from the dynamic, light induced potential, both images were subtracted (figure 6.4 (c)). This map of potential difference shows both bright areas corresponding to a potential increase (positive charging) and dark areas corresponding to a potential decrease (negative charging). Those areas are localized around the nano-rods. Areas more than $200\,\mathrm{nm}$ away from the particles do not show a significant potential change. On larger particle agglomerates, the charging of many nano-rods sums up and the resulting signals are more pronounced than on smaller piles and single particles (e.g. yellow circles in figure 6.4 (c)).

On top of the isolated particles, the charge separation can be studied exemplarily (upper yellow circle in figure 6.4 (c)). The $200\,\mathrm{nm}$ long and $60\,\mathrm{nm}$ wide particle has a $20 - 40\,\mathrm{nm}$ wide bright corona corresponding to a positive charging of up to $50\,\mathrm{mV}$. In the center of the particle, the potential difference is negative; down to $-20\,\mathrm{mV}$.
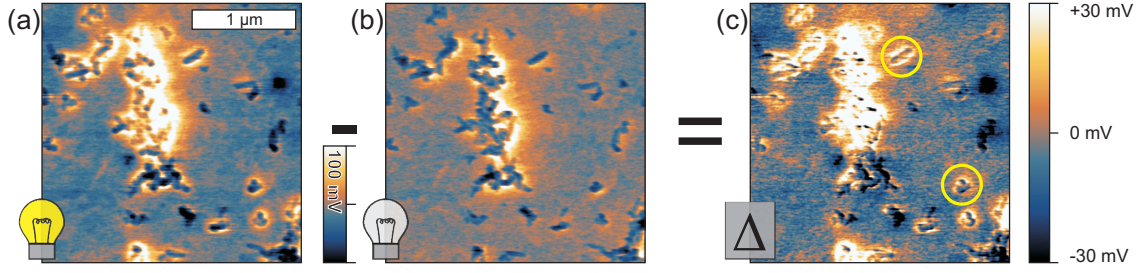
Figure 6.4: Background subtracted potential map in the dark (a) and (b) under laser illumination. (c) Difference calculated from (a) and (b). On isolated particles, the charge separation between the corona (bright) and the particles (dark) can be seen (yellow circles).

The KPFM tip cannot measure the full potential change inside the particle, because the polymer layer on top will shield parts of the signal (see figure 6.3 (b)). Thus, the $-20\,\mathrm{mV}$ are only an upper estimate for the true ZnO potential.

Assuming a symmetric charge distribution, the particle/polymer system can be approximated by a cylindrical capacitor with capacity

$$C = 2\pi\epsilon_0\epsilon \frac{l}{ln((R+d)/R)}\;. \tag{6.1}$$

where l is the length, R the radius of the nano-rod and d the thickness of the polymer layer or the mean distance of the positive charges. As an example, I chose an isolated particle in figure 6.4 (c) (upper yellow circle, $l = 200\,\mathrm{nm}$, $R = 30\,\mathrm{nm}$) and estimated the average distance of the charges to be $d = 20\,\mathrm{nm}$. The dielectric constant is approximated by a typical value for polymers ($\epsilon = 3$ [Lin08]). Using these values, the capacity of a single functionalized ZnO particle is estimated to be $65\,\mathrm{aF}$. In such a capacitor, a potential difference of $70\,\mathrm{mV}$ corresponds to a charging of $4{,}6 \cdot 10^{-18}\mathrm{C}$ or 29 electrons.

Figure 6.5: Topography of the TPD (a) and PS (b) functionalized ZnO nano-rods.
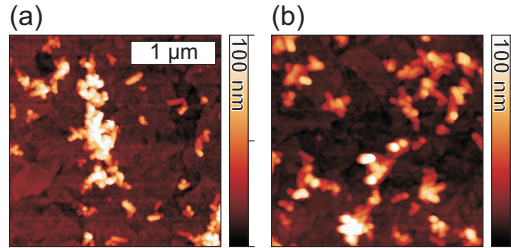
Finally, we tried to prove that the visualized potential change is caused by a charge separation between TPD and ZnO nano-rod. Light absorption and exciton generation in the dye could also lead to an electron transfer to the particle, only. In
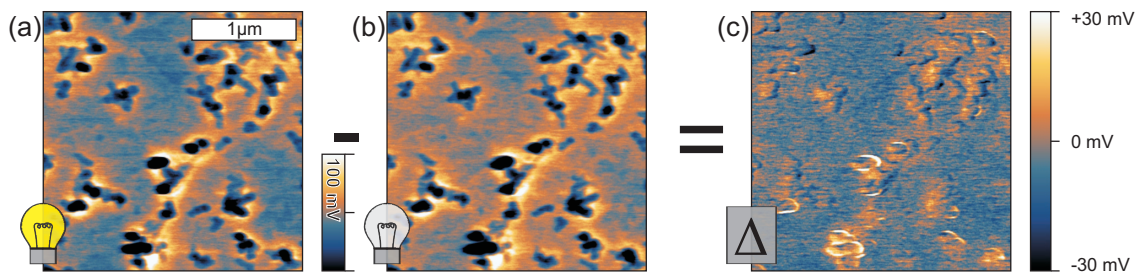
Figure 6.6: Reference measurement on PS/dye/anchor functionalized ZnO nano-rods. Surface potential on the (a) dark and (b) illuminated sample and (c) potential difference of (a) and (b).

this scenario, the positive charge would accumulate in the dye. Thus, Matthias Zorn synthesized a reference polymer containing the same dye/anchor moiety with a polystyrene block attached to it. Polystyrene has very poor charge transport properties and can be regarded as an insulator.

Figure 6.6 shows the potential maps recorded on the reference system. The map of the light induced potential difference (c) shows no larger areas of higher or lower potential. Only in the lower half of the image, circular areas of increased potential, $20-40\,$nm in diameter, show up around some of the particles. This is consistent with the previously stated scenario of localized positive charging in the dye.

Although qualitative differences between figure 6.4 (c) and figure 6.6 (c) are visible, a final statement on which system generates a more efficient charge separation is difficult. Thus, I compared the histograms of both images (figure 6.7). It revealed that on the reference sample, a much higher fraction of pixels was recorded with a potential difference of less than $10\,$mV (gray shaded area in figure 6.7). On the PS sample 90% of the pixels were in that region, whereas on the TPD sample it was 68%. This effect cannot be explained by the different particle densities on the two samples. The analysis of the topographic images (figure 6.5) showed the opposite: on the PS reference sample, 25% of the surface is covered with particles, compared to 16% surface coverage on the TPD sample. That is, although more particles are present on the reference sample, the electrical response of the TPD sample is stonger and more delocalized around the particles.

Furthermore, the analysis of the histogram for the TPD functionalized nano-rod sample revealed an asymmetry in the potential distribution. Whereas on 23% of the pixels a potential difference higher than $10\,$mV was recorded, only 8.5% have a difference lower than $-10\,$mV. This asymmetry can be explained by the lower surface fraction that is occupied by the particles compared to the polymer and the previously proposed shielding of the particle potential by the polymer corona.
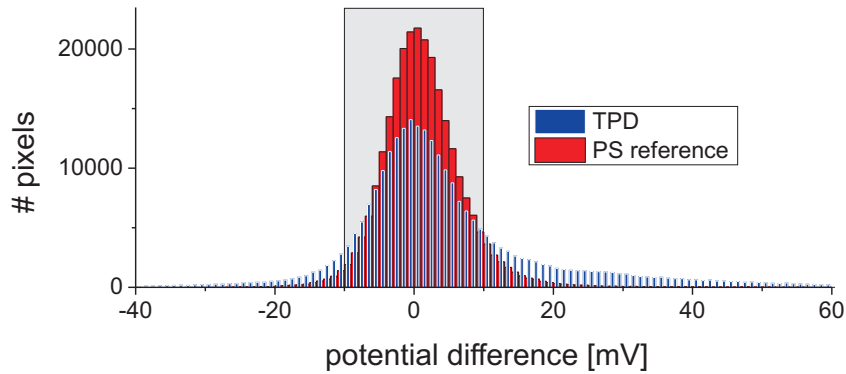
Figure 6.7: Histogram comparing the potential difference values from figure 6.4 (TPD system, blue) and 6.6 (PS system, red).

6.3 Summary

The KPFM experiments demonstrated that the new photoelectric SFM setup can study photo-induced charging on the level of single nanostructures. It was possible to differentiate between two possible charging scenarios: Simple charge transfer from the light absorbing dye to the ZnO nano-rod and additional charge transfer to the polymer corona. It could be demonstrated that the presence of a hole-conducting polymer corona facilitates the charge transfer to the corona and thus a more efficient charge separation. On the reference system, such a positive charging of the polymer corona could not be observed.

7 Concluding Remarks and Outlook

In my work, I demonstrated that the additional information about local surface properties provided by the electrical modes in scanning probe microscopy are a valuable extension to pure topographic imaging. In particular, the working mechanism of newly developed structures for organic solar cells were tested. Specific functionalities and problems (defects) that originate from the nanoscale sample structure could be identified. This kind of information gives important feedback to the synthetic chemists for the optimization of their materials.

7.1 Cross Sectional Analysis

On a focused ion beam polished cross cut, the function of a blocking layer and the electrical properties of the active layer could be studied by conductive scanning force microscopy. In particular, issues concerning the electrical contact between the layers and the conducting properties of different domains can be studied with a lateral resolution in the order of $10\,\mathrm{nm}$. By additional investigations with Kelvin Probe force microscopy the internal potential distribution in a solar cell device can be studied. Possible effects on the device performance caused by interface dipoles or space charges have been discussed [Blo07]. In particular the existence of space charges would change the internal potentials in a bulk heterojunction. In combination with illumination experiments, the rearrangement of the internal potentials could be visualized on the working working device.

In this context, the impact of the high energy ion exposure during the polishing procedure on the electronic structure of the device should be investigated further. It is well known that implantation of impurity atoms can have a huge impact on the electronic structure of a solid. Moreover, the high energy of the ions and the heat generated during the polishing can damage the molecular structure of the organic electronic compounds in a device. This damage can be minimized by using lower energy ions towards the end of the process, however, it cannot be ruled out completely.

Thus, alternative preparation procedures have to be considered. Microtome cutting, for example, is a well established technique for the preparation of thin cuts for transmission electron microscopy (TEM). Here, a sharp diamond blade cuts the sample in $10 - 100\,\mathrm{nm}$ thick slices. That way, both the sample and the slices become very smooth after a certain number of cutting steps. The remaining sample can now be used for SPM investigations. The main drawback of this method is the high force that acts on the sample during the cutting. Most organic electronic devices do not have a strong adhesion between their functional layers and thus, delamination is a major problem. Here, new sample preparation procedures have to be found that either increase the internal adhesion in the device or externally stabilize the structure.

In spite of the sample preparation issues, the cross sectional analysis on combination with electrical SPM is in my opinion one of the most promising fields for future projects.

7.2 SCTMM on Organic Structures

I have demonstrated, that scanning conductive torsion mode microscopy provides a valuable extension to the well established conductive scanning force microscopy. It allows non-destructive imaging on fragile three dimensional nano structures. Thus, the influence of the nanoscale structure of a material on the molecular packing and thus, on the transport properties of the material can be studied and compared to values obtained from bulk measurements.

Local spectroscopy in torsion mode, e.g. by current-voltage measurements, has advantages compared to experiments performed in contact mode. Applying a voltage to the tip gives rise to an electrical field between tip and sample. Thus, the attractive tip-sample force increases (see calculation in section 3.1.2 on page 24). In contact mode, this increase is not reflected in a stronger deflection in the cantilever. Thus, the feedback cannot compensate it and the contact area and interaction depth increases (see equation (5.3) on page 59). In torsion mode, an increased normal force leads to a stronger friction and thus, to a stronger damping of the torsion amplitude. The feedback will retract the tip to keep the amplitude constant. Thus, the contact area stays more defined during the voltage ramp.

For the nano-pillar arrays it would be interesting to perform spatially resolved current-voltage ramp experiments in order to look for variations in the charge carrier mobility. Furthermore, conductance measurements on the sidewall on a pillar could be performed. Therefore, a fracture or cross cut of a sample can be investigated. From the position dependent conductance, the nanoscale conductivity of the material can be derived.

7.3 Photoelectric SFM

With the new Photoelectric SFM setup, photo-induced processes can be studied on a nanometer scale. In particular, the charging of functionalized nanoparticles upon laser irradiation could be studied on the level of single nano-rods. The calculation of the nano-rod capacity revealed that under the experimental conditions ($10\,\mathrm{Wcm^{-2}}$), each nano-rod carries a charge of at least 20- 50 electrons. Thus, we can also estimate the limits of the method. Assuming a single, spherical nanoparticle with a radius of $20\,\mathrm{nm}$ and an additional $20\,\mathrm{nm}$ of polymer corona, we obtain a capacity of $13\,\mathrm{aF}$ (spherical capacitor). The detection limit of KPFM is in the order of $10\,\mathrm{mV}$. A charging of $20\,\mathrm{mV}$ in such a structure would correspond to roughly one to two elementary charges - or the dissociation of a single exciton. So in principle, the setup is capable of detecting single exciton dissociation events. By placing the tip on top of such a nanostructure, the dynamics of particle charging depending on different experimental conditions could be studied. In previous studies a temporal resolutions in the $100\,\mathrm{\mu s}$ range have been reported [Cof06]. By optimizing the mechanical and electrical properties of the cantilever and incorporating external lock-in amplifiers, an even faster response of the feedback will be possible.

Dynamic experiments are not only interesting for isolated nano-structures. Techniques like transient photovoltage [Foe09] or Photo-CELIV (current extraction by linearly increasing voltage) [Jus00, Dei08] can measure charge carrier concentrations and recombination rates by investigating the decay characteristics of the photovoltage after a light pulse. With a similar approach, Coffey and co-workers were able to measure variations in local charge carrier generation dynamics (time-resolved EFM, [Cof06]). However, their technique uses a very elaborate and lengthy measurement procedure, where on every spot of the sample, a decay characteristics is recorded.

A much easier approach would be to induce a response in the sample by a periodically modulated illumination intensity. If the timescales fit together, a mechanical vibration in the cantilever can be induced. This way, variations in the charge carrier generation and recombination dynamics can be studied with the lateral resolution of a scanning force microscope.

Finally, the charge carriers generated in a solar cell can be detected by the C-SFM current amplifier [Cof07]. Thus, the local performance of the structure can be correlated with the morphology. Thus, the underlying processes of charge separation can be better understood and the most efficient structures can be identified.

Bibliography

[Ale06]   A. Alexeev, J. Loos and M. Koetse, *Nanoscale electrical characterization of semiconducting polymer blends by conductive atomic force microscopy (c-afm)*, Ultramicroscopy **106**(3), p. 191 (2006), `dx.doi.org/10.1016/j.ultramic.2005.07.003`. 30

[Ale08]   A. Alexeev and J. Loos, *Conductive atomic force microscopy (c-afm) analysis of photoactive layers in inert atmosphere*, Org. Electron. **9**(1), p. 149 (2008), `dx.doi.org/10.1016/j.orgel.2007.10.003`. 30

[Ash76]   N. Ashcroft and N. Mermin, *Solid State Physics*, Harcourt, Orlando (1976). 8

[Bar99]   S. Barth, U. Wolf, H. Bässler, P. Müller, H. Riel, H. Vestweber, P. F. Seidler and W. Rieß, *Current injection from a metal to a disordered hopping system. iii. comparison between experiment and monte carlo simulation*, Phys. Rev. B **60**(12), p. 8791 (1999), `dx.doi.org/10.1103/PhysRevB.60.8791`. 28

[Bar10]   E. M. Barea, G. Garcia-Belmonte, M. Sommer, S. Hüttner, H. J. Bolink and M. Thelakkat, *Determination of charge carrier mobility of hole transporting polytriarylamine-based diodes*, Thin Solid Films **518**(12), p. 3351 (2010), `dx.doi.org/10.1016/j.tsf.2009.10.003`. 72

[Ben09]   G. Benstetter, R. Biberger and D. Liu, *A review of advanced scanning probe microscope analysis of functional films and semiconductor devices*, Thin Solid Films **517**(17), p. 5100 (2009), `dx.doi.org/10.1016/j.tsf.2009.03.176`. 26

[Ber07]   R. Berger, Y. Cheng, R. Forch, B. Gotsmann, J. S. Gutmann, T. Pakula, U. Rietzler, W. Schartl, M. Schmidt, A. Strack, J. Windeln and H.-J. Butt, *Nanowear on polymer films of different architecture*, Langmuir **23**(6), p. 3150 (2007), `dx.doi.org/10.1021/la0620399`. 49

[Ber09]   R. Berger, H.-J. Butt, M. B. Retschke and S. A. L. Weber, *Electrical modes in scanning probe microscopy*, Macromol. Rapid Commun. **30**(14), p. 1167 (2009), `dx.doi.org/10.1002/marc.200900220`. 26, 33

[Bin82]   G. Binnig, H. Rohrer, C. Gerber and E. Weibel, *Surface studies by scanning tunneling microscopy*, Phys. Rev. Lett. **49**(1), p. 57 (1982), `dx.doi.org/10.1103/PhysRevLett.49.57`. 1

[Bin83]   G. Binnig, H. Rohrer, C. Gerber and E. Weibel, *7 x 7 reconstruction on si(111) resolved in real space*, Phys. Rev. Lett. **50**(2), p. 120 (1983), `dx.doi.org/10.1103/PhysRevLett.50.120`. 1

[Bin86]   G. Binnig, C. F. Quate and C. Gerber, *Atomic force microscope*, Phys. Rev. Lett. **56**(9), p. 930 (1986), `dx.doi.org/10.1103/PhysRevLett.56.930`. 1, 21

[Blo97]   P. W. M. Blom, M. J. M. de Jong and M. G. van Munster, *Electric-field and temperature dependence of the hole mobility in poly(p-phenylene vinylene)*, Phys. Rev. B **55**(2), p. R656 (1997), `dx.doi.org/10.1103/PhysRevB.55.R656`. 13

[Blo07]   P. Blom, V. Mihailetchi, L. Koster and D. Markov, *Device physics of polymer:fullerene bulk heterojunction solar cells*, Adv. Mater. **19**(12), p. 1551 (2007), `dx.doi.org/10.1002/adma.200601093`. 17, 85

[Boe08]   B. de Boer and A. Facchetti, *Semiconducting polymeric materials*, Polym. Rev. **48**(3), p. 423 (2008), `dx.doi.org/10.1080/15583720802231718`. 11

[Boh97]   M. Bohmisch, F. Burmeister, A. Rettenberger, J. Zimmermann, J. Boneberg and P. Leiderer, *Atomic force microscope based kelvin probe measurements: Application to an electrochemical reaction*, J. Phys. Chem. B **101**(49), p. 10162 (1997), `dx.doi.org/10.1021/jp9728767`. 32

[Boz99]   L. Bozano, S. A. Carter, J. C. Scott, G. G. Malliaras and P. J. Brock, *Temperature- and field-dependent electron and hole mobilities in polymer light-emitting diodes*, Appl. Phys. Lett. **74**(8), p. 1132 (1999), `dx.doi.org/10.1063/1.123959`. 69

[Bra01]   C. J. Brabec, G. Zerza, G. Cerullo, S. D. Silvestri, S. Luzzati, J. C. Hummelen and S. Sariciftci, *Tracing photoinduced electron transfer process in conjugated polymer/fullerene bulk heterojunctions in real time*, Chem. Phys. Lett. **340**(3-4), p. 232 (2001), `dx.doi.org/10.1016/S0009-2614(01)00431-6`. 17

[Bre96]   J.-L. Bredas, J. Cornil and A. J. Heeger, *The exciton binding energy in luminescent conjugated polymers*, Adv. Mater. **8**(5), p. 447 (1996), `dx.doi.org/10.1002/adma.19960080517`. 15

[Bul09]   T. A. Bull, L. S. C. Pingree, S. A. Jenekhe, D. S. Ginger and C. K. Luscombe, *The role of mesoscopic pcbm crystallites in solvent vapor annealed copolymer solar cells*, ACS Nano **3**(3), p. 627 (2009), `dx.doi.org/10.1021/nn800878c`. 31

[Bur02]   L. Burgi, H. Sirringhaus and R. H. Friend, *Noncontact potentiometry of polymer field-effect transistors*, Appl. Phys. Lett. **80**(16), p. 2913 (2002), `dx.doi.org/10.1063/1.1470702`. 35

[Bur08]   V. Burtman, *Organic tunneling devices and field effect transistors using polycrystalline naphthalene diimine frameworks*, Thin Solid Films **516**(10), p. 3436 (2008), `dx.doi.org/10.1016/j.tsf.2007.06.010`. 28

[But03]   H. Butt, K. Graf and M. Kappl, *Physics and Chemistry of Interfaces*, Wiley-VCH Weinheim (2003). 24, 25, 53, 59

[Cam96]   I. H. Campbell, T. W. Hagler, D. L. Smith and J. P. Ferraris, *Direct measurement of conjugated polymer electronic excitation energies using metal/polymer/metal structures*, Phys. Rev. Lett. **76**(11), p. 1900 (1996), `dx.doi.org/10.1103/PhysRevLett.76.1900`. 15

[Cam99]   I. H. Campbell, D. L. Smith, C. J. Neef and J. P. Ferraris, *Consistent time-of-flight mobility measurements and polymer light-emitting diode current–voltage characteristics*, Appl. Phys. Lett. **74**(19), p. 2809 (1999), `dx.doi.org/10.1063/1.124021`. 13, 69

[Cha54]   D. M. Chapin, C. S. Fuller and G. L. Pearson, *A new silicon p-n junction photocell for converting solar radiation into electrical power*, J. Appl. Phys. **25**(5), p. 676 (1954), `dx.doi.org/10.1063/1.1721711`. 2

[Che06]   Y.-J. Cheng and J. Gutmann, *Morphology phase diagram of ultrathin anatase tio$_2$ films templated by a single ps-b-peo block copolymer*, J. Am. Chem. Soc. **128**(14), p. 4658 (2006), `dx.doi.org/10.1021/ja0562853`. 38

[Chi05]   M. Chiesa, L. Burgi, J.-S. Kim, R. Shikler, R. H. Friend and H. Sirringhaus, *Correlation between surface photovoltage and blend morphology in polyfluorene-based photodiodes*, Nano Lett. **5**(4), p. 559 (2005), `dx.doi.org/10.1021/nl047929s`. 35

[Cof06]   D. C. Coffey and D. S. Ginger, *Time-resolved electrostatic force microscopy of polymer solar cells*, Nat. Mater. **5**(9), p. 735 (2006), `dx.doi.org/10.1038/nmat1712`. 87

[Cof07]   D. Coffey, O. Reid, D. Rodovsky, G. Bartholomew and D. Ginger, *Mapping local photocurrents in polymer/fullerene solar cells with photoconductive atomic force microscopy*, Nano Lett. **7**(3), p. 738 (2007), `dx.doi.org/10.1021/nl062989e`. 31, 76, 87

[Cri03]   X. Crispin, S. Marciniak, W. Osikowicz, G. Zotti, A. W. D. van der Gon, F. Louwet, M. Fahlman, L. Groenendaal, F. D. Schryver and W. R. Salaneck, *Conductivity, morphology, interfacial chemistry, and stability*

of poly(3,4-ethylene dioxythiophene)-poly(styrene sulfonate): A photoelectron spectroscopy study, J. Polym. Sci., Part B: Polym. Phys. **41**(21), p. 2561 (2003), `dx.doi.org/10.1002/polb.10659`. 59

[Dai96]   H. Dai, E. W. Wong and C. M. Lieber, *Probing electrical transport in nanomaterials: Conductivity of individual carbon nanotubes*, Science **272**(5261), p. 523 (1996), `dx.doi.org/10.1126/science.272.5261.523`. 30

[Dan08a]   X.-D. Dang, M. Dante and T.-Q. Nguyen, *Morphology and conductivity modification of poly(3,4-ethylenedioxythiophene):poly(styrene sulfonate) films induced by conductive atomic force microscopy measurements*, Appl. Phys. Lett. **93**(24), 241911 (2008), `dx.doi.org/10.1063/1.3049599`. 49, 59, 67

[Dan08b]   M. Dante, J. Peet and T.-Q. Nguyen, *Nanoscale charge transport and internal structure of bulk heterojunction conjugated polymer/fullerene solar cells by scanning probe microscopy*, J. Phys. Chem. C **112**(18), p. 7241 (2008), `dx.doi.org/10.1021/jp712086q`. 30

[Dan09]   M. Dante, A. Garcia and T.-Q. Nguyen, *Three-dimensional nanoscale organization of highly efficient low band-gap conjugated polymer bulk heterojunction solar cells*, J. Phys. Chem. C **113**(4), p. 1596 (2009), `dx.doi.org/10.1021/jp809650p`. 30

[Dei08]   C. Deibel, A. Baumann and V. Dyakonov, *Polaron recombination in pristine and annealed bulk heterojunction solar cells*, Appl. Phys. Lett. **93**(16), 163303 (2008), `dx.doi.org/10.1063/1.3005593`. 87

[Dou06]   O. Douheret, L. Lutsen, A. Swinnen, M. Breselge, K. Vandewal, L. Goris and J. Manca, *Nanoscale electrical characterization of organic photovoltaic blends by conductive atomic force microscopy*, Appl. Phys. Lett. **89**(3), 032107 (2006), `dx.doi.org/10.1063/1.2227846`. 30

[Dou07a]   O. Douheret, A. Swinnen, S. Bertho, I. Haeldermans, J. D'Haen, M. D'Olieslaeger, D. Vanderzande and J. V. Manca, *High-resolution morphological and electrical characterisation of organic bulk heterojunction solar cells by scanning probe microscopy*, Prog. Photovoltaics Res. Appl. **15**(8), p. 713 (2007), `dx.doi.org/10.1002/pip.795`. 49

[Dou07b]   O. Douheret, A. Swinnen, M. Breselge, I. Van Severen, L. Lutsen, D. Vanderzande and J. Manca, *High resolution electrical characterisation of organic photovoltaic blends*, Microelectron. Eng. **84**(3), p. 431 (2007), `dx.doi.org/10.1016/j.mee.2006.10.056`. 4

[Dru00]   P. Drude, *Zur elektronentheorie der metalle*, Ann. Phys-Leipzig. **306**(3), p. 566 (1900), `dx.doi.org/10.1002/andp.19003060312`. 7

[Ert06]   D. Erts, B. Polyakov, B. Daly, M. A. Morris, S. Ellingboe, J. Boland and J. D. Holmes, *High density germanium nanowire assemblies: Contact challenges and electrical characterization*, J. Phys. Chem. B **110**(2), p. 820 (2006), `dx.doi.org/10.1021/jp055309p`. 60

[Foe09]   A. Foertig, A. Baumann, D. Rauh, V. Dyakonov and C. Deibel, *Charge carrier concentration and temperature dependent recombination in polymer-fullerene solar cells*, Appl. Phys. Lett. **95**(5), 052104 (2009), `dx.doi.org/10.1063/1.3202389`. 87

[Fre00]   M. Freitag, M. Radosavljević, W. Clauss and A. T. Johnson, *Local electronic properties of single-wall nanotube circuits measured by conducting-tip afm*, Phys. Rev. B **62**(4), p. R2307 (2000), `dx.doi.org/10.1103/PhysRevB.62.R2307`. 34, 49

[Fum08]   L. Fumagalli, I. Casuso, G. Ferrari and G. Gomila, *Applied Scanning Probe Methods VIII - Scanning Probe Microscopy Techniques*, Kapitel Probing Electrical Transport Properties at the Nanoscale by Current-Sensing Atomic Force Microscopy, p. 421–450, NanoScience and Technology, Springer Berlin Heidelberg (2008), `dx.doi.org/10.1007/978-3-540-74080-3`. 26

[Gar02]   R. Garcìa and R. Pérez, *Dynamic atomic force microscopy methods*, Surf. Sci. Rep. **47**(6-8), p. 197 (2002), `dx.doi.org/10.1016/S0167-5729(02)00077-8`. 22, 23

[Gie95]   F. J. Giessibl, *Atomic resolution of the silicon (111)-(7x7) surface by atomic force microscopy*, Science **267**(5194), p. 68 (1995), `dx.doi.org/10.1126/science.267.5194.68`. 24

[Gir10]   R. Giridharagopal and D. S. Ginger, *Characterizing morphology in bulk heterojunction organic photovoltaic systems*, J. Phys. Chem. Lett. **1**(7), p. 1160 (2010), `dx.doi.org/10.1021/jz100100p`. 13

[Gre03]   B. Grevin, P. Rannou, R. Payerne, A. Pron and J.-P. Travers, *Scanning tunneling microscopy investigations of self-organized poly(3-hexylthiophene) two-dimensional polycrystals*, Adv. Mater. **15**(11), p. 881 (2003), `dx.doi.org/10.1002/adma.200304580`. 67

[Gro09]   L. Gross, F. Mohn, N. Moll, P. Liljeroth and G. Meyer, *The chemical structure of a molecule resolved by atomic force microscopy*, Science **325**(5944), p. 1110 (2009), `dx.doi.org/10.1126/science.1176210`. 24

[Gug00]   M. Guggisberg, M. Bammerlin, C. Loppacher, O. Pfeiffer, A. Abdurixit, V. Barwich, R. Bennewitz, A. Baratoff, E. Meyer and H.-J. Güntherodt, *Separation of interactions by noncontact force microscopy*, Phys. Rev. B **61**(16), p. 11151 (2000), `dx.doi.org/10.1103/PhysRevB.61.11151`. 25

[Gun07]   S. Gunes, H. Neugebauer and N. S. Sariciftci, *Conjugated polymer-based organic solar cells*, Chem. Rev. **107**(4), p. 1324 (2007), `dx.doi.org/10.1021/cr050149z`. 60

[Hab09]   N. Haberkorn, J. S. Gutmann and P. Theato, *Template-assisted fabrication of free-standing nanorod arrays of a hole-conducting cross-linked triphenylamine derivative: Toward ordered bulk-heterojunction solar cells*, ACS Nano **3**(6), p. 1415 (2009), `dx.doi.org/10.1021/nn900207a`. 60, 61

[Hab10]   N. Haberkorn, S. A. L. Weber, R. Berger and P. Theato, *Template-based preparation of free-standing semiconducting polymeric nanorod arrays on conductive substrates*, ACS Appl. Mater. Interfaces **2**(6), p. 1573 (2010), `dx.doi.org/10.1021/am100085t`. 61

[Ham88]   C. Hamann, H. Burghardt and T. Frauenheim, *Electrical Conduction Mechanisms in Solids*, VEB Deutscher Verlag der Wissenschaften, Berlin (1988). 13, 28, 30

[Ham10]   B. H. Hamadani, S. Jung, P. M. Haney, L. J. Richter and N. B. Zhitenev, *Origin of nanoscale variations in photoresponse of an organic solar cell*, Nano Lett. **10**(5), p. 1611 (2010), `dx.doi.org/10.1021/nl9040516`. 30

[Han01]   W. Hansen, *Standard reference surfaces for work function measurements in air*, Surf. Sci. **481**(1-3), p. 172 (2001), `dx.doi.org/10.1016/S0039-6028(01)01036-6`. 32

[Her82]   H. Hertz, *Über die berührung fester elastischer körper*, Journal für die reine und angewandte Mathematik **92**, p. 156 (1882). 59

[Hig03]   A. M. Higgins, S. J. Martin, P. C. Jukes, M. Geoghegan, R. A. L. Jones, S. Langridge, R. Cubitt, S. Kirchmeyer, A. Wehrum and I. Grizzi, *Interfacial structure in semiconducting polymer devices.*, J. Mater. Chem. **13**(11), p. 2814 (2003), `dx.doi.org/10.1039/b304990f`. 59

[Hop05]   H. Hoppe, T. Glatzel, M. Niggemann, A. Hinsch, M. Lux-Steiner and N. Sariciftci, *Kelvin probe force microscopy study on conjugated polymer/fullerene bulk heterojunction organic solar cells*, Nano Lett. **5**(2), p. 269 (2005), `dx.doi.org/10.1021/nl048176c`. 35, 46

[Hsu10]   J. W. Hsu and M. T. Lloyd, *Organic/inorganic hybrids for solar energy generation*, Mrs. Bull. **35**, p. 422 (2010). 19

[Hua04]   L. Huang and C. Su, *A torsional resonance mode afm for in-plane tip surface interactions*, Ultramicroscopy **100**(3-4), p. 277 (2004), `dx.doi.org/10.1016/j.ultramic.2003.11.010`. 22, 50, 53, 60

[IZ04]   C. Ionescu-Zanetti, A. Mechler, S. Carter and R. Lal, *Semiconductive polymer blends: Correlating structure with transport properties at the nanoscale*, Adv. Mater. **16**(5), p. 385 (2004), `dx.doi.org/10.1002/adma.200305747`. 30, 59

[Jac99]   H. O. Jacobs, H. F. Knapp and A. Stemmer, *Practical aspects of kelvin probe force microscopy*, Rev. Sci. Instrum. **70**(3), p. 1756 (1999), `dx.doi.org/10.1063/1.1149664`. 33, 41

[Jar08]   S. P. Jarvis, J. E. Sader and T. Fukuma, *Applied Scanning Probe Methods VIII*, Kapitel Frequency Modulation Atomic Force Microscopy in Liquids, p. 315 – 350, Springer Berlin Heidelberg (2008), `dx.doi.org/10.1007/978-3-540-74080-3_9`. 24

[Joh71]   K. L. Johnson, K. Kendall and A. D. Roberts, *Surface energy and the contact of elastic solids*, Proc. R. Soc. London, Ser. A **324**(1558), p. 301 (1971), `dx.doi.org/10.1098/rspa.1971.0141`. 53

[Jør08]   M. Jørgensen, K. Norrman and F. C. Krebs, *Stability/degradation of polymer solar cells*, Sol. Energ. Mat. Sol. C. **92**(7), p. 686 (2008), `dx.doi.org/10.1016/j.solmat.2008.01.005`, degradation and Stability of Polymer and Organic Solar Cells. 64, 76

[Jus00]   G. Juska, K. Arlauskas, M. Viliunas and J. Kocka, *Extraction current transients: New method of study of charge transport in microcrystalline silicon*, Phys. Rev. Lett. **84**(21), p. 4946 (2000), `dx.doi.org/10.1103/PhysRevLett.84.4946`. 87

[Kaw02]   T. Kawagishi, A. Kato, Y. Hoshi and H. Kawakatsu, *Mapping of lateral vibration of the tip in atomic force microscopy at the torsional resonance of the cantilever*, Ultramicroscopy **91**(1-4), p. 37 (2002), `dx.doi.org/10.1016/S0304-3991(02)00080-3`. 22, 50

[Kel98]   V. Kelvin, *Contact electricity of metals*, Philos. Mag. Series 5 **46**(278), p. 82 (1898), `dx.doi.org/10.1080/14786449808621172`. 32

[Kel99]   T. W. Kelley, E. Granstrom and C. D. Frisbie, *Conducting probe atomic force microscopy: A characterization tool for molecular electronics*, Adv. Mater. **11**(3), p. 261 (1999), `dx.doi.org/10.1002/(SICI)1521-4095(199903)11:3<261::AID-ADMA261>3.0.CO;2-B`. 30

[Kem04]   M. Kemerink, S. Timpanaro, M. M. de Kok, E. A. Meulenkamp and F. J. Touwslager, *Three-dimensional inhomogeneities in pedot:pss films*, J. Phys. Chem. B **108**(49), p. 18820 (2004), `dx.doi.org/10.1021/jp0464674`. 30

[Kip09]   B. Kippelen and J.-L. Bredas, *Organic photovoltaics*, Energy Environ. Sci. **2**(3), p. 251 (2009), `dx.doi.org/10.1039/b812502n`. 16

[Kir05]   S. Kirchmeyer and K. Reuter, *Scientific importance, properties and growing applications of poly(3,4-ethylenedioxythiophene)*, J. Mater. Chem. **15**(21), p. 2077 (2005), `dx.doi.org/10.1039/b417803n`. 12

[Kur98]   S. Kurokawa and A. Sakai, *Gap dependence of the tip-sample capacitance*, J. Appl. Phys. **83**(12), p. 7416 (1998), `dx.doi.org/10.1063/1.367985`. 24

[Lec09]   M. C. Lechmann, D. Kessler and J. S. Gutmann, *Functional templates for hybrid materials with orthogonal functionality*, Langmuir **25**(17), p. 10202 (2009), `dx.doi.org/10.1021/la900980y`, pMID: 19624139. 44, 45

[Lee08]   J. I. Lee, S. H. Cho, S.-M. Park, J. K. Kim, J. K. Kim, J.-W. Yu, Y. C. Kim and T. P. Russell, *Highly aligned ultrahigh density arrays of conducting polymer nanorods using block copolymer templates*, Nano Lett. **8**(8), p. 2315 (2008), `dx.doi.org/10.1021/nl801105s`. 60

[Leu92]   O. M. Leung and M. C. Goh, *Orientational ordering of polymers by atomic force microscope tip-surface interaction*, Science. **255**(5040), p. 64 (1992), `dx.doi.org/10.1126/science.255.5040.64`. 49

[Li06]   J. C. Li, S. C. Blackstock and G. J. Szulczewski, *Interfaces between metal and arylamine molecular films as probed with the anode interfacial engineering approach in single-layer organic diodes*, J. Phys. Chem. B **110**(35), p. 17493 (2006), `dx.doi.org/10.1021/jp060407b`. 28

[Lin02]   H.-N. Lin, H.-L. Lin, S.-S. Wang, L.-S. Yu, G.-Y. Perng, S.-A. Chen and S.-H. Chen, *Nanoscale charge transport in an electroluminescent polymer investigated by conducting atomic force microscopy*, Appl. Phys. Lett. **81**(14), p. 2572 (2002), `dx.doi.org/10.1063/1.1509464`. 30, 67, 69, 72

[Lin08]   Y. H. Lin, Y. C. Sun, W. B. Jian, H. M. Chang, Y. S. Huang and J. J. Lin, *Electrical transport studies of individual iro 2 nanorods and their nanorod contacts*, Nanotechnology **19**(4), p. 045711 (2008), `dx.doi.org/10.1088/0957-4484/19/04/045711`. 81

[Lis08]   A. Liscio, V. Palermo, K. Mullen and P. Samori, *Tip-sample interactions in kelvin probe force microscopy: Quantitative measurement of the local surface potential*, J. Phys. Chem. C **112**(44), p. 17368 (2008), `dx.doi.org/10.1021/jp806657k`. 35

[Lis10]   A. Liscio, V. Palermo and P. Samori, *Nanoscale quantitative measurement of the potential of charged nanostructures by electrostatic and kelvin probe force microscopy: Unraveling electronic processes in complex materials,*

Acc. Chem. Res. **43**(4), p. 541 (2010), `dx.doi.org/10.1021/ar900247p`. 35

[Liu09]   R. Liu, *Imaging of photoinduced interfacial charge separation in conjugated polymer/semiconductor nanocomposites*, J. Phys. Chem. C **113**(21), p. 9368 (2009), `dx.doi.org/10.1021/jp810732n`. 35

[Liu10]   L. Liu and G. Li, *Electrical characterization of single-walled carbon nanotubes in organic solar cells by kelvin probe force microscopy*, Appl. Phys. Lett. **96**(8), 083302 (2010), `dx.doi.org/10.1063/1.3332489`. 35

[Loi98]   M. J. Loiacono, E. L. Granstrom and C. D. Frisbie, *Investigation of charge transport in thin, doped sexithiophene crystals by conducting probe atomic force microscopy*, J. Phys. Chem. B **102**(10), p. 1679 (1998), `dx.doi.org/10.1021/jp973269m`. 30

[Mag03]   S. Magonov and N. Yerina, *High-temperature atomic force microscopy of normal alkane c60h122 films on graphite*, Langmuir **19**(3), p. 500 (2003), `dx.doi.org/10.1021/la0206615`. 23

[Mar87]   Y. Martin, C. C. Williams and H. K. Wickramasinghe, *Atomic force microscope–force mapping and profiling on a sub 100-[a-ring] scale*, J. Appl. Phys. **61**(10), p. 4723 (1987), `dx.doi.org/10.1063/1.338807`. 22

[Mar88]   Y. Martin, D. W. Abraham and H. K. Wickramasinghe, *High-resolution capacitance measurement and potentiometry by force microscopy*, Appl. Phys. Lett. **52**(13), p. 1103 (1988), `dx.doi.org/10.1063/1.99224`. 31

[Mem09]   M. Memesa, S. Weber, S. Lenz, J. Perlich, R. Berger, P. Muller-Buschbaum and J. S. Gutmann, *Integrated blocking layers for hybrid organic solar cells.*, Energy Environ. Sci. **2**(7), p. 783 (2009), `dx.doi.org/10.1039/b902754h`. 38, 39

[Men09]   Y. Men, X. Zhang and W. Wang, *Capillary liquid bridges in atomic force microscopy: Formation, rupture, and hysteresis*, J. Chem. Phys. **131**(18), 184702 (2009), `dx.doi.org/10.1063/1.3257624`. 24

[Mot50]   N. Mott and R. Gurney, *Electronic Processes in Ionic Crystals (second edition)*, Oxford University Press, London (1950). 29

[Mur93]   M. P. Murrell, M. E. Welland, S. J. O'Shea, T. M. H. Wong, J. R. Barnes, A. W. McKinnon, M. Heyns and S. Verhaverbeke, *Spatially resolved electrical measurements of sio[sub 2] gate oxides using atomic force microscopy*, Appl. Phys. Lett. **62**(7), p. 786 (1993), `dx.doi.org/10.1063/1.108579`. 3, 26, 28

[Non91]   M. Nonnenmacher, M. P. O'Boyle and H. K. Wickramasinghe, *Kelvin probe force microscopy*, Appl. Phys. Lett. **58**(25), p. 2921 (1991), `dx.doi.org/10.1063/1.105227`. 3, 33

[Olb98]   A. Olbrich, B. Ebersberger and C. Boit, *Conducting atomic force microscopy for nanoscale electrical characterization of thin sio[sub 2]*, Appl. Phys. Lett. **73**(21), p. 3114 (1998), `dx.doi.org/10.1063/1.122690`. 28

[O'R91]   B. O'Regan and M. Grätzel, *A low-cost, high-efficiency solar cell based on dye-sensitized colloidal tio2 films*, Nature **353**(6346), p. 737 (1991), `dx.doi.org/10.1038/353737a0`. 19

[Ots03]   Y. Otsuka, Y. Naitoh, T. Matsumoto and T. Kawai, *Point-contact current-imaging atomic force microscopy: Measurement of contact resistance between single-walled carbon nanotubes in a bundle*, Appl. Phys. Lett. **82**(12), p. 1944 (2003), `dx.doi.org/10.1063/1.1563308`. 49

[Pab98]   P. J. de Pablo, J. Colchero, J. Gómez-Herrero and A. M. Baró, *Jumping mode scanning force microscopy*, Appl. Phys. Lett. **73**(22), p. 3300 (1998), `dx.doi.org/10.1063/1.122751`. 49

[Pai70]   D. M. Pai, *Transient photoconductivity in poly(n-vinylcarbazole)*, J. Chem. Phys. **52**(5), p. 2285 (1970), `dx.doi.org/10.1063/1.1673300`. 12

[Pal06]   V. Palermo, M. Palma and P. Samori, *Electronic characterization of organic thin films by kelvin probe force microscopy*, Adv. Mater. **18**(2), p. 145 (2006), `dx.doi.org/10.1002/adma.200501394`. 35

[Pal07a]   V. Palermo, A. Liscio, D. Gentilini, F. Nolde, K. Muellen and P. Samori, *Scanning probe microscopy investigation of self-organized perylenetetracarboxdiimide nanostructures at surfaces: Structural and electronic properties*, Small **3**(1), p. 161 (2007), `dx.doi.org/10.1002/smll.200600381`. 35

[Pal07b]   V. Palermo, G. Ridolfi, A. Talarico, L. Favaretto, G. Barbarella, N. Camaioni and P. Samori, *A kelvin probe force microscopy study of the photogeneration of surface charges in all-thiophene photovoltaic blends*, Adv. Funct. Mater. **17**(3), p. 472 (2007), `dx.doi.org/10.1002/adfm.200600122`. 35

[Par06]   V. A. Parsegian, *Van der Waals Forces*, Cambridge University Press, New York (2006). 25

[Pen04]   B. Peng, G. Jungmann, C. Jäger, D. Haarer, H.-W. Schmidt and M. Thelakkat, *Systematic investigation of the role of compact tio2 layer in solid state dye-sensitized tio2 solar cells*, Coord. Chem. Rev. **248**(13-14), p. 1479 (2004), `dx.doi.org/10.1016/j.ccr.2004.02.008`. 38

[Pin08] L. S. C. Pingree, B. A. MacLeod and D. S. Ginger, *The changing face of pedot:pss films: Substrate, bias, and processing effects on vertical charge transport*, J. Phys. Chem. C **112**(21), p. 7922 (2008), `dx.doi.org/10.1021/jp711838h`. 59, 67

[Pin09a] L. S. C. Pingree, O. G. Reid and D. S. Ginger, *Electrical scanning probe microscopy on active organic electronic devices*, Adv. Mater. **21**(1), p. 19 (2009), `dx.doi.org/10.1002/adma.200801466`. 30, 35

[Pin09b] L. S. C. Pingree, O. G. Reid and D. S. Ginger, *Imaging the evolution of nanoscale photocurrent collection and transport networks during annealing of polythiophene/fullerene solar cells*, Nano Lett. **9**(8), p. 2946 (2009), `dx.doi.org/10.1021/nl901358v`. 31

[Poc06] A. Pochettino, *Sul comportamento foto-elettrico dell'antracene.*, Acad. Lincei Rendiconti **15**, p. 355 (1906). 1

[Pun03] K. P. Puntambekar, P. V. Pesavento and C. D. Frisbie, *Surface potential profiling and contact resistance measurements on operating pentacene thin-film transistors by kelvin probe force microscopy*, Appl. Phys. Lett. **83**(26), p. 5539 (2003), `dx.doi.org/10.1063/1.1637443`. 35

[Rei08] O. G. Reid, K. Munechika and D. S. Ginger, *Space charge limited current measurements on conjugated polymer films using conductive atomic force microscopy*, Nano Lett. **8**(6), p. 1602 (2008), `dx.doi.org/10.1021/nl080155l`. 30, 71

[Sch29] G. Schmaltz, *Über glätte und ebenheit als physikalisches und physiologisches problem*, Zeitschrift des Vereins deutscher Ingenieure **12**, p. 1461 (1929). 1, 2

[Sco03] J. C. Scott, *Metal–organic interface and charge injection in organic electronic devices*, J. Vac. Sci. Technol., A **21**(3), p. 521 (2003), `dx.doi.org/10.1116/1.1559919`. 13, 28

[See09] A. Seemann, H.-J. Egelhaaf, C. J. Brabec and J. A. Hauch, *Influence of oxygen on semi-transparent organic solar cells with gas permeable electrodes*, Org. Electron. **10**(8), p. 1424 (2009), `dx.doi.org/10.1016/j.orgel.2009.08.001`. 76

[Sha08] P. E. Shaw, A. Ruseckas and I. D. W. Samuel, *Exciton diffusion measurements in poly(3-hexylthiophene)*, Adv. Mater. **20**(18), p. 3516 (2008), `dx.doi.org/10.1002/adma.200800982`. 17

[Smi07] E. C. P. Smits, S. G. J. Mathijssen, M. Cölle, A. J. G. Mank, P. A. Bobbert, P. W. M. Blom, B. de Boer and D. M. de Leeuw, *Unified description of potential profiles and electrical transport in unipolar and ambipolar*

organic field-effect transistors, Phys. Rev. B: Condens. Matter **76**(12), 125202 (2007), `dx.doi.org/10.1103/PhysRevB.76.125202`. 35

[Sna06]   H. Snaith and M. Grätzel, *The role of a "schottky barrier" at an electron-collection electrode in solid-state dye-sensitized solar cells*, Adv. Mater. **18**(14), p. 1910 (2006), `dx.doi.org/10.1002/adma.200502256`. 47

[Sti00]   T. Stifter, O. Marti and B. Bhushan, *Theoretical investigation of the distance dependence of capillary and van der waals forces in scanning force microscopy*, Phys. Rev. B **62**(20), p. 13667 (2000), `dx.doi.org/10.1103/PhysRevB.62.13667`. 24

[Sug02]   H. Sugimura, Y. Ishida, K. Hayashi, O. Takai and N. Nakagiri, *Potential shielding by the surface water layer in kelvin probe force microscopy*, Appl. Phys. Lett. **80**(8), p. 1459 (2002), `dx.doi.org/10.1063/1.1455145`. 34

[Tan86]   C. W. Tang, *Two-layer organic photovoltaic cell*, Appl. Phys. Lett. **48**(2), p. 183 (1986), `dx.doi.org/10.1063/1.96937`. 2

[Tel02]   K. A. Telari, B. R. Rogers, H. Fang, L. Shen, R. A. Weller and D. N. Braski, *Characterization of platinum films deposited by focused ion beam-assisted chemical vapor deposition*, J. Vac. Sci. Technol., B **20**(2), p. 590 (2002), `dx.doi.org/10.1116/1.1458958`. 55

[Tes09]   N. Tessler, Y. Preezant, N. Rappaport and Y. Roichman, *Charge transport in disordered organic materials and its relevance to thin-film devices: A tutorial review*, Adv. Mater. **21**(27), p. 2741 (2009), `dx.doi.org/10.1002/adma.200803541`. 12

[Uhr10]   C. L. Uhrich, G. Schwartz, B. Maennig, W. M. Gnehr, S. Sonntag, O. Erfurth, E. Wollrab, K. Walzer, J. Foerster, A. Weiss, O. Tsaryova, K. Leo, M. K. Riede and M. Pfeiffer, *Efficient and long-term stable organic vacuum deposited tandem solar cells*, in P. L. Heremans, R. Coehoorn and C. Adachi (Herausgeber), *Organic Photonics IV*, Band 7722, p. 77220G, SPIE (2010), `dx.doi.org/10.1117/12.855088`. 3

[Utk08]   I. Utke, P. Hoffmann and J. Melngailis, *Gas-assisted focused electron beam and ion beam processing and fabrication*, J. Vac. Sci. Technol., B **26**(4), p. 1197 (2008), `dx.doi.org/10.1116/1.2955728`. 57

[Wan09a] H.-S. Wang, L.-H. Lin, S.-Y. Chen, Y.-L. Wang and K.-H. Wei, *Ordered polythiophene/fullerene composite core–shell nanorod arrays for solar cell applications*, Nanotechnology **20**(7), p. 075201 (5pp) (2009), `dx.doi.org/10.1088/0957-4484/20/7/075201`. 60

[Wan09b] K. Wang, P. Birjukovs, D. Erts, R. Phelan, M. A. Morris, H. Zhou and J. D. Holmes, *Synthesis and characterisation of ordered arrays of*

mesoporous carbon nanofibres, J. Mater. Chem. **19**(9), p. 1331 (2009), `dx.doi.org/10.1039/b817156d`. 60

[Wat05]   P. K. Watkins, A. B. Walker and G. L. B. Verschoor, *Dynamical monte carlo modelling of organic solar cells: The dependence of internal quantum efficiency on morphology*, Nano Lett. **5**(9), p. 1814 (2005), `dx.doi.org/10.1021/nl051098o`. 17, 18

[Wea91]   J. M. R. Weaver and H. K. Wickramasinghe, *Semiconductor characterization by scanning force microscope surface photovoltage microscopy*, Journal of Vacuum Science & Technology B: Microelectronics and Nanometer Structures **9**(3), p. 1562 (1991), `dx.doi.org/10.1116/1.585424`. 3

[Yan07]   X. Yang and J. Loos, *Toward high-performance polymer solar cells: The importance of morphology control*, Macromolecules **40**(5), p. 1353 (2007), `dx.doi.org/10.1021/ma0618732`. 60

[Yan10]   C.-W. Yang and I.-S. Hwang, *Soft-contact imaging in liquid with frequency-modulation torsion resonance mode atomic force microscopy*, Nanotechnology. **21**(6), p. 065710 (2010), `dx.doi.org/10.1088/0957-4484/21/6/065710`. 24

[Yur08]   A. Yurtsever, A. M. Gigler, C. Dietz and R. W. Stark, *Frequency modulated torsional resonance mode atomic force microscopy on polymers*, Appl. Phys. Lett. **92**(14), 143103 (2008), `dx.doi.org/10.1063/1.2907498`. 60, 71

[Zen09]   T.-W. Zeng, F.-C. Hsu, Y.-C. Tu, T.-H. Lin and W.-F. Su, *Kelvin probe force microscopy study on hybrid p3ht:titanium dioxide nanorod materials*, Chem. Phys. Lett. **479**(1-3), p. 105 (2009), `dx.doi.org/10.1016/j.cplett.2009.07.104`. 35

[Zer05]   U. Zerweck, C. Loppacher, T. Otto, S. Grafstrom and L. M. Eng, *Accuracy and resolution limits of kelvin probe force microscopy*, Phys. Rev. B: Condens. Matter **71**(12), 125424 (2005), `dx.doi.org/10.1103/PhysRevB.71.125424`. 34

[Zie07]   D. Ziegler, J. Rychen, N. Naujoks and A. Stemmer, *Compensating electrostatic forces by single-scan kelvin probe force microscopy*, Nanotechnology. **18**(22), p. 225505 (5pp) (2007), `dx.doi.org/10.1088/0957-4484/18/22/225505`. 34

[Zor08]   M. Zorn, S. Meuer, M. N. Tahir, Y. Khalavka, C. Sonnichsen, W. Tremel and R. Zentel, *Liquid crystalline phases from polymer functionalised semiconducting nanorods*, J. Mater. Chem. **18**(25), p. 3050 (2008), `dx.doi.org/10.1039/b802666a`. 79

[Zor10]   M. Zorn, S. A. L. Weber, M. N. Tahir, W. Tremel, H.-J. Butt, R. Berger and R. Zentel, *Light induced charging of polymer functionalized nanorods*, Nano Lett. **11**(8), p. 2812 (2010), `dx.doi.org/10.1021/nl100741n`. 80

Acknowledgments

"And now, the end is near, I have to face the final curtain..."

With my favorite Norebang[1]-song (my deepest apologies for this melodramatic quote) I want to express my gratitude towards all the people that made it possible for me to do it *My Way*:

Under the supervision of my Doktorvater **Prof. Hans-Jürgen Butt** I have all the freedom and the chances, a young scientist can wish to have. At the same time, Hans-Jürgen is always open for questions and discussions and gave me invaluable input for my work. Thank you!

The most important person for my scientific work was, is and hopefully will be for some time after my PhD **Rüdiger Berger**. A typical situation: I have a question or something to discuss. I walk to Rüdiger's office. Three hours later we have (a) answered my question/discussed the data (b) found an interesting question that goes far beyond the topic (c) discussed issues concerning his new garage (d) commented on recent AK-Butt seminar talks (e) discussed and outlined the work of that could be interesting for the next five years and so on. Working on papers, posters and conference abstracts with Rüdiger is very exhausting ("hey, there are three words that are not marked in red!!!") but he manages to bring everything we do to the highest level. And most important: in every discussion there is room for a laugh. Thank you for being my mentor during the last three years!

Furthermore, I would like to thank Prof. **Thomas Palberg** from the University of Mainz, who kindly agreed to be the second referee for my dissertation.

I want to express my gratitude towards **Prof. Kookheon Char** who hosted me in his group during my first four months at Seoul National University in South Korea. In his group I learned many things about layer-by-layer assembly and quantum dot based optoelectronics. I also would like to thank **Prof. Changhee Lee**, my host during my second stay at Seoul National University. In his group I gathered invaluable knowledge about state of the art organic optoelectronic devices and device characterization.

---

[1]Korean: Karaoke-Bar.

The cornerstone of my work was the team spirit and the good collaboration within the International Research Training Group "Self organized materials for Optoelectronics" (or simply "**IRTG**"). Next to providing me money and the chance to visit Korea, the project offered me the most valuable thing I have received during my PhD: the chance for real *interdisciplinary* work. I learned to see the world from a chemist's or an engineer's point of view and was given the chance to investigate exciting new classes of materials with the eyes of a physicist. All this under the guidance of one man, who "dreams sometimes" and whose dreams of a fruitful interdisciplinary and international collaboration sometimes come true: **Prof. Rudolf Zentel**. Thank you very much! Another important part is the never ending support for our common work by the "PIs", in particular **Prof. Jochen Gutmann** and **Patrick Theato**.

The numerous collaborations with fellow IRTG students would not have been possible without the good cooperative spirit in our group. Beyond collaborations I found some true friends. I want to thank **Maria Lechmann** for asking me physics questions and, much more, for answering my chemistry questions (also: thanks for the chemical drawings). I am very happy and relieved that the fears you had after the first IRTG "sojulizing" did not come true! I also want to thank **Niko Haberkorn** and **Matthias Zorn**. I am sure that all our collaborations would not have been that successful without all the fun we had together during our numerous IRTG activities. In spite of big plans for joint publications (in particular review papers), the scientific collaboration with my Nogdu-neighbor **Kim Hun** has so far not been that successful (but thank you for borrowing me the beam profiler!). However, he taught me lots of things about Korea and - most important - we had lots of fun during the time there ("What happens in Korea...").

Next to Hun, many other people from Seoul National University supported me in my struggle with the Korean culture, language and door frames that were too low for my size. In particular I would like to thank **Suh Hyoseon** who took care of me and Regina when we arrived in Korea for the first time. I want to thank **Bae Wanki**, **Noh Seunguk** and **Lee Donggu** for lots of help and scientific and non-scientific discussions.

But also in Mainz at the MPIP I was supported by many people. I want to thank **Mine Memesa** for the good collaboration and really intersting samples (the origin of the nano-turtle). I really have to thank **all** my colleagues for not strangling me during the last three years when I made my paronomasias! In particular my office mates, namely **Helma Burg**, **Tassilo Kaule**, **Maren Müller**, **Huong Nguyen**, **Sascha Pihan**, **Maria Retschke**, **Uwe Rietzler** and **Esha Sengupta** were very indulgent with me. I also want to thank them for the good (working) atmosphere in our office! I want to thank the **AK Butt** for the non-scientific discussions in the coffee corner that have always been very stimulating. The level (auf deutsch: Niveau) of

the discussion was often ameliorated (and equally often exacerbated) by the spirited contributions of **Tim Still**. In addition to that, I want to thank him for granting me asylum in his office during the last months of my thesis-writing. Speaking of asylum: I want to thank the Asylum Research team in Mannheim, in particular **Stefan Vinzelberg** for the help with the MFP3D. And speaking of scanning force microscopes I have to mention **Uwe Rietzler**, the master of the numerous scanning force microscopes in our main lab. He helped me on numerous occasions throughout my PhD time when struggling with user hostile hard- and software. **Andreas Best** was a big help for all kinds of problems regarding lasers and optics. **Helma Burg** supported me not only with SFM related issues, she occasionally helped me to fix my furniture (der Sitzsack: vielen Dank nochmal!). **Maren Müller** and **Michael Kappl** taught me how to use the focused ion beam and, in particular, how to fix it when it didn't work. Finally, I want to acknowledge the help by electronics- and the mechanics workshop (**Dirk Richter** and **Achim Gerstenberg**) and in particular **"Professor" Roman Pilz** and **Benjamin Ettmüller** from the Haustechnik for the construction of the passive noise shielding of the MFP3D setup.

During the tutorial lecture I was giving at the university I met two talented and enthusiastic physicists, **Dominik Pilat** and **Victor Bergmann**, who worked with me on a number of projects on the side tracks of my PhD. Although not everything they did lead to a Science paper, their support and the constant stream of questions were an important and inspiring part of my PhD time. The same stands for the two former diploma and now PhD students, **Maria Retschke** and **Anna Domanski**, who significantly increased the number of people working with "electric SPM on organic stuff".

If you, dear reader, found any spelling or grammar mistakes while reading this dissertation you can blame me. If not, it is thanks to my proof readers that fought their way through the manuscript. So my thanks go to **Regina Bauer**, **Andreas Kolloch**, **Sascha Pihan** and **Laura Hennemann**.

I thank my grandfathers, **Alban Reiter** (A.) and **Ludwig Weber** (L.), for making me unique.

I want to thank my parents **Irmgard** and **Karl-Heinz Weber** for their never ending support, love and patience, in particular when I started to disassemble radios and the video recorder during my early adolescence.

At last I want to thank **Regina Bauer** for everything she does and is.

Curriculum Vitae

Stefan Weber

Date of birth: August 2nd, 1981

Place of birth: Trier, Germany

Nationality: German

Dissertation

09/2007 - 08/2010

PhD thesis in the IRTG "Self-organized Materials for Optoelectronics" at the Max Planck Institute for Polymer Research in the group of Prof. Dr. Hans-Jürgen Butt (Project leader: Dr. Rüdiger Berger)

02/2010 - 04/2010

Research stay at the School of Electrical Engineering and Computer Science in the group of Prof. Dr. Changhee Lee at Seoul National University, South Korea

12/2008 - 04/2010

Research stay at the School of Chemical and Biological Engineering in the group of Prof. Dr. Kookheon Char at Seoul National University, South Korea

Study

10/2001 - 07/2007

Study at the University Konstanz, Department of Physics. Degree obtained: "Physik Diplom"

07/2006 - 07/2007

Diploma thesis in the group of Prof. Dr. Johannes Boneberg, University of Konstanz, Department of Physics. Topic: "Laserinduced Nanobubbles - Interaction of gold nanoparticles with pulsed laserlight".

School Education

09/1992 - 06/2001

Gymnasium am Hoptbühl in Villingen-Schwenningen, Germany. Degree obtained: "Abitur" (university entrance exam).

List of Publications and Presentations

Accepted Publications:

M. Memesa, S. Weber, S. Lenz, J. Perlich, R. Berger, P. Müller-Buschbaum and J.S. Gutmann, *Integrated blocking layers for hybrid organic solarcells.*, Energy Environ. Sci. **2**(7), p. 783 (2009).

R. Berger, H.-J. Butt, M.B. Retschke and S.A.L. Weber, *Electrical modes in scanning probe microscopy*, Macromol. Rapid Commun. **30**(14), p. 1167 (2009).

J. Kwak, W.K. Bae, M. Zorn, H. Woo, H. Yoon, J. Lim, S.W. Kang, S. Weber, H.-J. Butt, R. Zentel, S. Lee, K. Char and C. Lee, *Characterization of quantum dot/conducting polymer hybrid films and their application to light-emitting diodes*, Adv. Mater. **21**(48), p. 5022 (2009).

N. Haberkorn, S.A.L. Weber, R. Berger and P. Theato, Template-based preparation of free-standing semiconducting polymeric nanorod arrays on conductive substrates, ACS Appl. Mater. & Interfaces **2**, p. 1573 (2010).

S.A.L. Weber, M. Memesa, R. Berger, H.-J. Butt and J.S. Gutmann, *Electrical scanning probe microscopy of an integrated blocking layer*, J. Nanosci. Nanotechnol. **10**, p. 6840 (2010).

S.A.L. Weber, N. Haberkorn, P. Theato and R. Berger, *Mapping of local conductivity variations on fragile nanopillar arrays by scanning conductive torsionmode microscopy*, Nano Lett. **10**(4), p. 1194 (2010).

M. Zorn, S.A.L. Weber, M.N. Tahir, W. Tremel, H.-J. Butt, R. Berger and R. Zentel, *Light induced charging of polymer functionalized nanorods*, Nano Lett. **11**, 2812 (2010).

Manuscripts under preparation/submitted:

S Frank, L. Steidl, S.A.L. Weber, M. Panthöfer, A. Birkel, D. Koll, R. Berger, R. Zentel and W. Tremel, *Electrodeposition of ZnO nanorods on an opaline replica as hierarchically structured systems*, J. Mater. Chem., submitted (21.08.2010).

M. Lechmann, S.A.L. Weber, J. Geserick, N. Huesing, R. Berger, J.S. Gutmann, *Investigating Morphology and Electronic Properties of Self-Assembled Hybrid systems for Solar Cells*, Energy Environ. Sci., close to submission.

Oral Presentations at International Conferences and Meetings:

08.2010 Session III: "Nanomaterials - Properties: electric, magnetic, chemical, thermal, optical", Seeing the Nanoscale VIII, Basel Switzerland: "Mapping of Local Conductivity Variations in Torsion Mode by Scanning Probe Microscopy".

12.2009 Symposium OO: "Dynamic Scanning Probes - Imaging, Characterization, and Manipulation", MRS fall meeting, Boston, MA: "Walking on Jellyrods - Mapping of Local Conductivity Variations in Torsion Mode by Scanning Probe Microscopy".

02.2009 IRTG spring meeting Seoul: "Nanoscale Characterization of Organic Optoelectronic Materials - Scanning Probe Microscopy beyond topography".

11.2007 IRTG Workshop on Optoelectronic Devices, Nierstein, Germany: "Electrical Properties of Organic Optoelectronic Materials".

09.2007 IRTG fall meeting Seoul: "Kelvin Probe Microscopy for Electrical Characterization: The Fourth Dimension in AFM Imaging".

Poster Presentations at International Conferences and Meetings:

12.2009 Symposium D: "Organic Materials for Printable Thin-Film Electronic Devices" MRS fall meeting, Boston, MA: "Nanoscale Visualization of Conducting Percolation Paths in a TiO_2/Insulator Matrix by Scanning Force Microscopy".

12.2009 Symposium OO: "Dynamic Scanning Probes - Imaging, Characterization, and Manipulation" MRS fall meeting, Boston, MA: "Reference Structures for Electrical Scanning Probe Microscopy".

08.2009 International Workshop on: "Self-Organized Materials for Optoelectronics", Mainz, Germany: "Mapping Local Conductivity Changes in Torsion Mode".

09.2008 International Conference on Advanced Functional Polymers and Self-Organized Materials, Busan, Korea: "Scanning Probe Microscopy of Blocking Layers for Hybrid Organic Solar Cells".

02.2008 IRTG Spring meeting, Rottach-Egern, Germany: "Nanoscale Characterization of Optoelectronic Materials".